学位論文（要約）

High-Tc superconductivity studied by diagrammatic extensions of the dynamical mean field theory

(動的平均場理論のダイアグラマティックな拡張による高温超伝導の研究)

平成 28 年１２月博士（理学）申請

東京大学大学院理学系研究科

物理学専攻

北谷　基治

Ph.D Thesis

High-Tc superconductivity studied by diagrammatic extensions of the dynamical mean field theory

Motoharu Kitatani

Department of Physics
Graduate School of Science
University of Tokyo

December 2016

Abstract

While it is over 30 years since the high-T_c superconductor was discovered, the cuprates have attracted great interests in many scientific fields. Understanding high-T_c is one of the most challenging issues in the condensed matter theory. The mechanism of the superconductivity in these materials is still not fully understood, and continues to be discussed intensely. Specifically, the two-dimensional repulsive Hubbard model, which is a representative model for the cuprates, still has many questions, and many analytical and numerical methods have been proposed for studying the superconductivity, magnetism and other instabilities.

In the present thesis, we propose to combine the non-perturbative dynamical mean field theory (DMFT) with the perturbative diagrammatic expansion techniques to treat the local correlation effects ("Mott physics") and momentum dependent pairing interaction (that produces the d-wave pairing superconductivity) to explore the superconductivity and various instabilities in the Hubbard model.

First, we formulate the combination of the fluctuation exchange (FLEX) approximation and DMFT in a self-consistent manner in terms of the Luttinger-Ward functional for superconducting phases. The resultant phase diagram exhibits a clear T_c dome structure against the band filling as observed experimentally, while in the ordinary FLEX, T_c almost monotonically increases toward the half-filling. We trace the origin of the T_c-dome back to a combined effect of the filling dependence of the local vertex correction and the filling dependence of the pairing interaction.

As another effect inherent in the strongly correlated systems, we study a phase transition for the Pomeranchuk instability, where the four-fold rotational symmetry in the electronic structure on the tetragonal lattice is spontaneously broken into two-fold due to an interaction effect. We find that the Pomeranchuk instability is remarkably more sensitive to the Fermi surface warping than the superconducting T_c dome. An interesting question is the effect of the distorted Fermi surface due to the Pomeranchuk instability on the superconductivity, and we have revealed that the gap function is slightly changed from ordinary d-wave pairing to (d+s)-wave. Furthermore, we find that the Fermi surface distortion can enhance the superconducting T_c in frustrated systems.

Finally, we consider the extension of the DMFT vertex to study the vertex correction effect on nonlocal self-energy and the pairing interaction. For this purpose, we employ the DΓA (dynamical vertex approximation) formalism, which is extended here to accommodate superconducting phases. For the Hubbard model we obtain the T_c-dome due to a combined effect as in the FLEX+DMFT case, but the transition temperature is reduced by the vertex correction. We also find that the pairing interaction is strongly screened by the vertex correction effect.

Contents

Chapter 1

Introduction

In condensed matter physics, we intend to clarify and create many interesting materials and phenomena. Various properties of materials are studied in this field, and in many cases electron correlation plays an important role. Then one of the most important questions in this field is "how to treat the correlated many-electron systems?". Electron correlation is a very difficult problem, and various approximations have been introduced so far.

One of the simplest ways is treating the system as a free particle system. The band theory is based on this picture, and this simple scheme succeeds to describe the difference between metals, semiconductors and insulators. Despite its simplicity, this is often powerful even for correlated electron systems when we introduce the idea of quasi-particles. Based on the Fermi liquid theory [1], correlated electron systems can be thought of as a set of particles (quasi-particles) with a renormalized mass, which represents some nature of correlated electron systems. However, there are important cases, where the Fermi liquid theory does not work.

One example is the case where the correlation is very strong. In the band theory, insulators must have an even number of electrons per unit cell. On the other hand, some materials are in insulating states even when they have odd numbers of electrons per unit cell [2]. Mott pointed out that this insulating state is due to the effect of the Coulomb repulsion [3]. If two electrons are on the same site, the electrons feel a strong Coulomb repulsion. Therefore, for a strong enough Coulomb repulsion, the system can be insulating even for an odd number of electrons per unit cell. Such an insulator is known as the Mott insulator.

Another example is the case of attractive interactions. While electrons interact repulsively via the Coulomb interaction, Cooper pointed out that if there is an effective attractive interaction between electrons, the Fermi sea becomes unstable and a two-electron bound state (the Cooper pair) appears. The Fermi surface instability is known as the superconductivity. The superconductivity is experimentally discovered by Kamerlingh-Onnes in 1911 [4]. Since then, the su-

perconductivity is one of the hottest topics in condensed matter physics. The superconductivity accompanies the Meissner-Ochsenfeld effect (perfect diamagnetism) [5] and zero resistivity as effects of spontaneously broken U(1) gauge. Bardeen, Cooper, and Schrieffer explained the superconductivity theoretically, known as the BCS theory [6]. In the BCS theory, the effective attraction comes from the exchange of phonons, and the gap function, which characterizes the superconducting state, is usually isotropic in momentum space (s-wave pairing). The BCS theory succeeds to explain many properties of the conventional superconductors. In the BCS theory, T_c is estimated to be $T_c \approx \hbar\omega_{\rm D} e^{-\frac{1}{VD}}$, where V and D are the effective attraction and the density of states at the Fermi energy, respectively, while $\omega_{\rm D}$ is the Debye frequency of phonons. Before the high-T_c superconductivity was discovered in the cuprates, it was considered that the superconducting transition temperature T_c could not exceed few tens of K in the BCS theory.

The cuprate superconductors, the main target of the present thesis, are considered to have both of two difficulties explained above (i.e., the existence of (i) strong correlation and (ii) the effective attraction in a repulsively interacting system), and there still remain many puzzles even though it is more than 30 years since the cuprates were discovered in 1986. These materials attract not only theoretical interests, but also experimentally great attentions because they have the highest superconducting transition temperature at ambient pressure.

In this chapter, we introduce cuprate superconductors and explain a representative model for cuprates. We then explain the outline of this thesis.

1.1 Cuprate superconductors

Crystal structures

In 1986, Bednorz and Müller discovered a copper oxide superconductor, which is $La_{2-x}Ba_xCuO_4$(LBCO), where x is the carrier doping level [7]. After that, many high-T_c superconductors were discovered [8, 9, 10]. These superconductors have attracted extensive attention of researchers due to the high superconducting transition temperature T_c as well as many kinds of unusual behaviors in the electronic properties. The typical lattice structure is shown in Fig. 1.1.

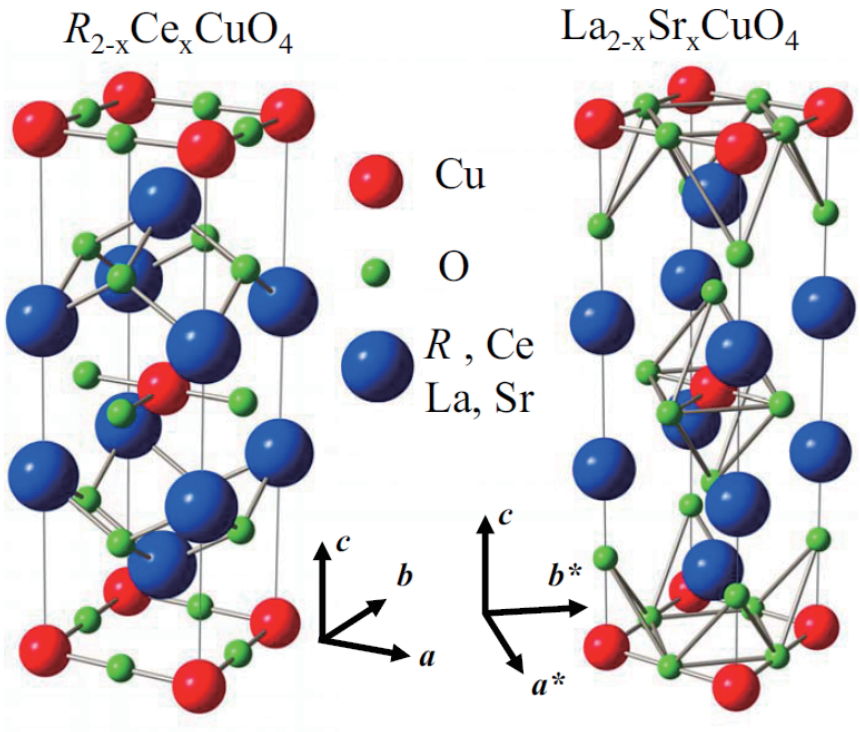

Figure 1.1: The lattice structure of the high-T_c cuprate (left: typical electron-doped cuprate RCCO, where R is a rare-earth ion, right: typical hole-doped cuprate LSCO)(from Ref. [11]).

The high-T_c cuprates are all based on layered perovskite structures, and they have copper-oxide square planes separated by charge reservoir blocks. The structure is basically tetragonal crystal systems, which has four-fold rotational symmetry. The parent materials of the cuprates are antiferromagnetic insulators and the superconductivity occurs by carrier doping. There are hole-doped and electron-doped cuprates. For example, in the LSCO (the right panel in Fig. 1.1), holes

are introduced into the CuO_2 planes by substitution of Sr with La. In the RCCO (the left panel in Fig. 1.1), electrons are introduced into the CuO_2 planes by substitution of Ce with R, where R is one of rare-earth ions such as Nd, Pr, Sm, and Eu.

Phase diagram

The doping-dependence of the transition temperature is one of the most important features of the cuprates. A typical phase diagram is shown in Fig. 1.2. The

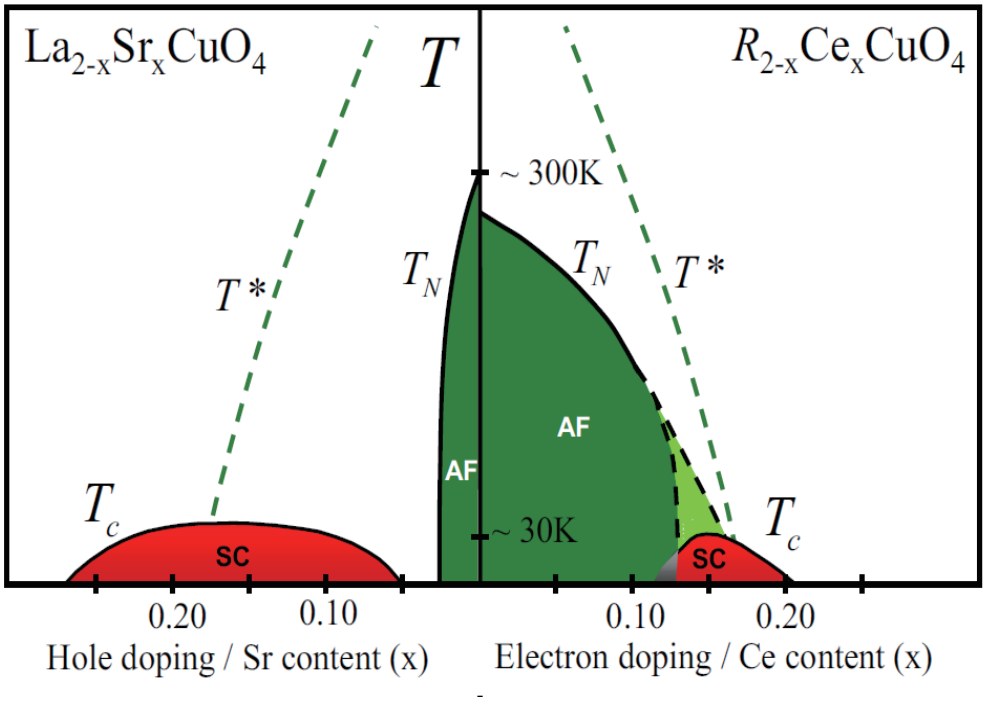

Figure 1.2: A typical phase diagram of the cuprates (LSCO and RCCO) (from Ref. [11]). The vertical axis is the temperature while the horizontal axis is the doping level.

parent (undoped) cuprate is an antiferromagnetic insulator, and the antiferromagnetic insulator phase disappears and a superconducting phase appears as we introduce the carrier. The transition temperature is peaked at a finite doping level (called the optimal doping), and T_c decreases for further carrier doping (overdoped region). This structure is called the T_c-dome. Recently, an experiment reported that there are electron doped copper-oxide materials that show superconductivity near zero-doping if apical oxygens are carefully removed [12].

The symmetry of the pairing and the gap function are important factors characterizing cuprate superconductors. The momentum dependence of the gap function is determined to be an anisotropic d-wave from phase sensitive measurements [13]. The high transition temperature and the anisotropic gap function are not explained by the BCS theory, and the mechanism of superconductivity in high-T_c cuprates is one of the most challenging issues in condensed matter physics.

Charge orders

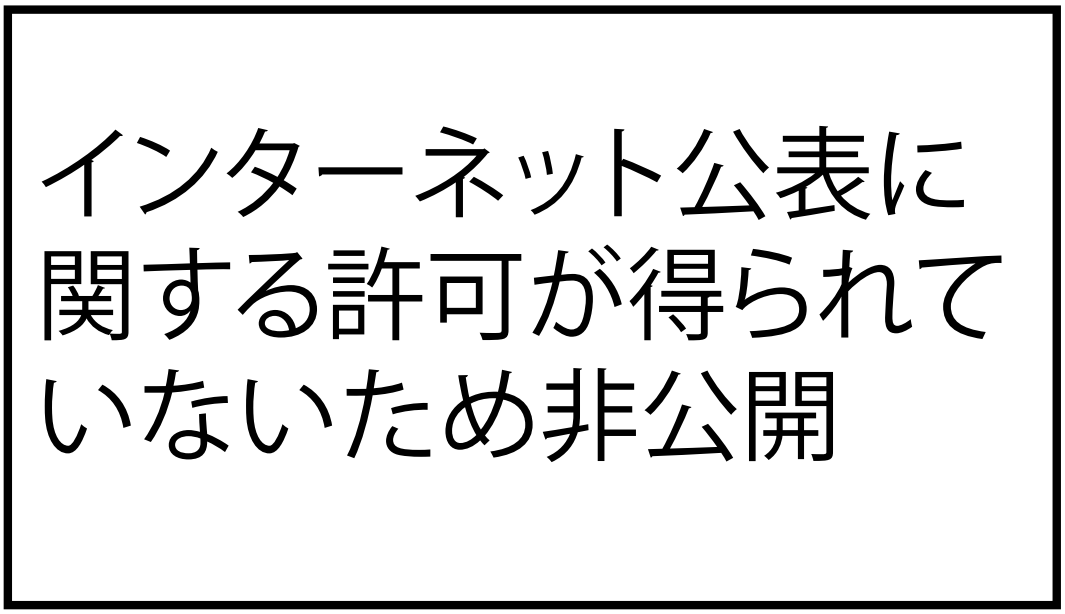

Figure 1.3: (a) A neutron scattering result for the spin-excitations spectrum at 7 meV in a-b plane around $\boldsymbol{Q}_{\rm AF} = (0.5, 0.5)$ in reciprocal lattice units (from Ref. [20]). (b) A tunneling result for $Z(\boldsymbol{r}, \omega = \Delta(\boldsymbol{r})) \equiv g(\boldsymbol{r}, \omega)/g(\boldsymbol{r}, -\omega)$, where g is the differential tunneling conductance (dI/dV) and Δ measures a the pseudogap magnitude (from Ref. [21]).

There are many experimental results indicating a charge ordered state in cuprate superconductors [14, 15, 16, 17, 18]. Recently many phase boundaries regarding the charge order are considered to exist in the cuprate phase diagram [19]. There are experiments suggesting the existence of electronic nematic states, where the four-fold symmetry of the electronic state is spontaneously broken [20, 21, 22]. In Fig. 1.3(a), we show a result of a neutron scattering measurement for $YBa_2Cu_3O_{6.45}$ [20], which indicates an in-plane anisotropy in magnetic excitations. We can also see a breakdown of the four-fold symmetry in the electronic state in Fig. 1.3(b), which is the result of a tunneling measurement.

Pairing interaction

Mechanism of the superconductivity in high-T_c cuprates is different from those in the conventional superconductors and it cannot be explained by the BCS theory. The electron correlation induced by the Coulomb repulsion is thought to play an important role in the cuprates.

The BCS gap equation is

$$\Delta(\boldsymbol{k}) = -\sum_{\boldsymbol{k}'} V(\boldsymbol{k}, \boldsymbol{k}') \frac{\Delta(\boldsymbol{k}')}{2E(\boldsymbol{k}')} \tanh\left(\frac{1}{2}\beta E(\boldsymbol{k}')\right), \tag{1.1}$$

where Δ is the gap function, $\boldsymbol{k}$ is the momentum, V is the pairing interaction, and E is defined as

$$E(\boldsymbol{k}) = \sqrt{\epsilon(\boldsymbol{k})^2 + \Delta(\boldsymbol{k})^2}, \tag{1.2}$$

where $\epsilon(\boldsymbol{k})$ is the band dispersion. In the BCS theory, we assume that the interaction V does not depend on the momentum, and hence the gap function is isotropic and the interaction V must be negative (attractive) to obtain a non-zero Δ. On the other hand, if the effective interaction is momentum-dependent, a repulsive interaction V can give rise to a non-zero Δ by sign change of the gap function as described in Fig. 1.4. Thus the origin of this momentum-dependent effective interaction is one of the most fundamental questions for cuprates.

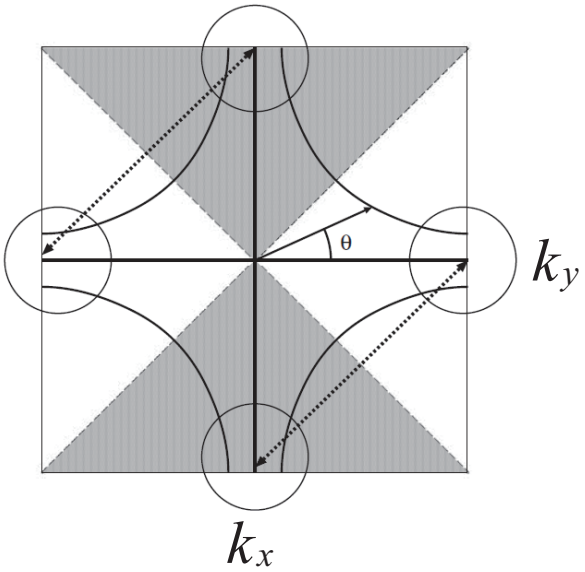

Figure 1.4: A typical Fermi surface in cuprates (solid curves) (from Ref. [23]). The superconducting gap function has opposite signs between the shaded and white regions. The strongest pair-scattering process is shown by the dashed lines. The encircled regions are around the antinodal region.

1.2 Hubbard model on the square lattice

For studying the origin of the momentum dependent effective pairing interaction, there are many studies for the tight-binding models which consider the electron hopping and an on-site repulsive Coulomb interaction. All the cuprates have copper-oxide planes and the superconductivity is thought to occur on these planes. Therefore, the tight-binding model of this plane, the d-p model and a simpler model, the Hubbard model, are used [24]. While the d-p model is a more accurate model for the CuO_2 plane, we often consider a maximally localized Wannier basis (Zhang-Rice singlet [25] in the hole-doped case) and use the single-orbital Hubbard model on a square lattice as the simplest low-energy effective model of the cuprate.

In this thesis, we focus on the two-dimensional repulsive Hubbard model, whose Hamiltonian is

$$\mathcal{H} = \sum_{\boldsymbol{k},\sigma} \epsilon(\boldsymbol{k}) c^{\dagger}_{\boldsymbol{k},\sigma} c_{\boldsymbol{k},\sigma} + U \sum_{i} n_{i,\uparrow} n_{i,\downarrow}, \tag{1.3}$$

where $c^{\dagger}_{\boldsymbol{k},\sigma}$ and $c_{\boldsymbol{k},\sigma}$ are respectively creation and annihilation operators of an electron with the wave-vector $\boldsymbol{k} = (k_x, k_y)$ and the spin σ, U is the repulsive interaction strength, and n is the number operator defined as

$$n_{i,\sigma} = c^{\dagger}_{i,\sigma} c_{i,\sigma}. \tag{1.4}$$

The two-dimensional dispersion $\epsilon(\boldsymbol{k})$ is given as

$$\epsilon(\boldsymbol{k}) = -2t(\mathrm{cos}k_x + \mathrm{cos}k_y) - 4t'\mathrm{cos}k_x\mathrm{cos}k_y - 2t''(\mathrm{cos}2k_x + \mathrm{cos}2k_y) - \mu, \tag{1.5}$$

where t, t', and t'' represent the nearest-neighbor, second-neighbor, and third-neighbor hopping parameters, respectively. A schematic diagram is shown in Fig 1.5. Here μ is the chemical potential. In practice, this value is determined so as to fit the density of electrons ρ as

$$\rho = \frac{1}{\beta N_{\boldsymbol{k}}} \sum_{k} \frac{e^{i\omega_n 0^+}}{i\omega_n - \epsilon(\boldsymbol{k}) - \Sigma(k)}, \tag{1.6}$$

where β is the inverse temperature, $N_{\boldsymbol{k}}$ is the total number of k-points, ω_n is the ferimonic Matsubara frequency, $k = (\omega_n, \boldsymbol{k})$ and $\Sigma(k)$ is the self-energy which is explained in chapter 2 in detail.

This model is the most popular model for investigating correlated electron systems. The first term in the Hamiltonian represents the kinetic energy, while the second term the correlation of electrons. This model is the simplest model which includes itinerancy of the band electrons and the short-range (on-site) interaction.

If we consider the weak-coupling limit $U/t \to 0$, where the kinetic term of the Hamiltonian dominates, then the Hamiltonian $\mathcal{H}_{\mathrm{kin}} = \sum_{\boldsymbol{k},\sigma} \epsilon(\boldsymbol{k}) c^{\dagger}_{\boldsymbol{k},\sigma} c_{\boldsymbol{k},\sigma}$ is

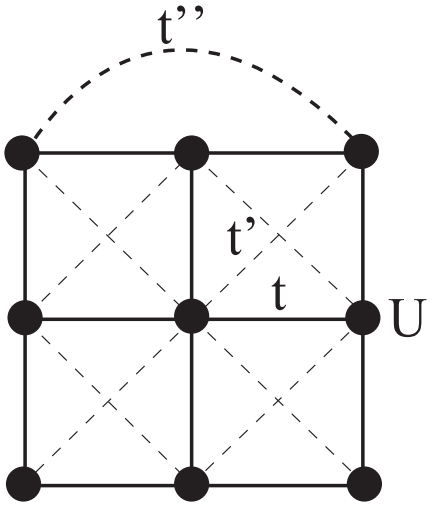

Figure 1.5: Two-dimensional square lattice model. The lines with t, t', and t'' represent the nearest-neighbor, second-neighbor, and third-neighbor hopping parameters, while U is the on-site Hubbard repulsion.

diagonalized in momentum space. On the other hand, if we consider the strong-coupling limit $t/U \to 0$, where the interaction term dominates, then the Hamiltonian $\mathcal{H}_{\rm int} = U \sum_i n_{i,\uparrow} n_{i,\downarrow}$ is diagonalized in real space, and the density of states is separated into two with a separation $\sim U$. The density of states in the two limits are schematically displayed in Fig. 1.6. From these limiting behaviors, we can see that this simple model contains the Mott physics. Once both terms coexist, it is too difficult to solve this model exactly. The difficulty of this model comes from combination of these two natures, in other words, it is difficult to describe a Mott insulator in momentum space.

There are many studies for single and multi-band Hubbard models to describe the superconductivity in the cuprates. Scalapino et al. have proposed a spin-fluctuation mediated d-wave pairing mechanism and studied superconductivity diagrammatically by using the random phase approximation (RPA) [26] and the fluctuation exchange (FLEX) approximation [27]. Quantum Monte Carlo (QMC) simulations also show that the d-wave pairing correlation function is dominant in the two-dimensional square lattice Hubbard model [28, 29, 30, 31].

1.3 Motivation and organization of the thesis

Despite a lot of theoretical studies, the mechanism of the high-T_c cuprate is not fully clarified yet. While QMC is exact within numerical errors, we can treat limited system sizes. RPA and FLEX cannot describe the Mott physics and the

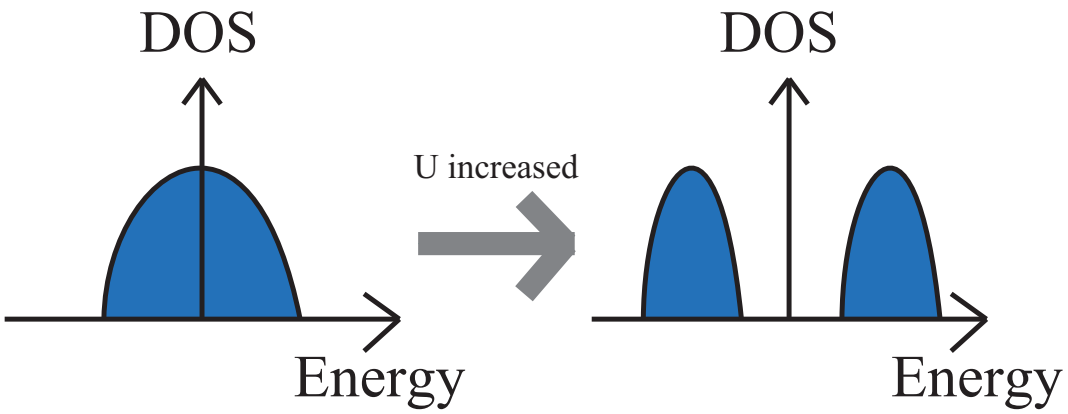

Figure 1.6: A schematic picture of the Mott-Hubbard transition. U is the interaction strength. Left panel shows the weak-coupling regime, where the band theory works well, while right panel shows the strong-coupling regime, where the density of states (DOS) splits into the upper and lower Hubbard bands.

T_c-dome, and these approaches are considered to be more appropriate for the overdoped region. On the other hand, the dynamical mean field theory [32, 33, 34], which is the typical non-perturbative method and can describe the Mott transition, ignores the momentum dependence of the self-energy and cannot describe anisotropic pairing. To include the momentum dependence of the self-energy effect, cluster extensions of the dynamical mean field theory have been proposed [35, 36, 37]. These schemes map the bulk into a small-size cluster impurity problem, instead of considering a single site impurity problem in DMFT, and recently succeeded to describe the T_c-dome [38] and the pseudogap is suggested to come from the momentum-dependent Mott gap in this formalism [39, 40]. However, these schemes ignore long-range fluctuations (such as antiferromagnetic ones), and long-range fluctuation effects in these calculations are open questions. More recently, diagrammatic extensions of the dynamical mean field theory have been proposed [41, 42, 43, 44, 45] to take into account the long-range fluctuation effects, which are ignored in small-size cluster methods. Within these schemes, the importance of long-range fluctuation effect is recently realized [46, 47].

Given these situations, we study the phase diagram, charge instability, and pairing interaction of the Hubbard model by employing diagrammatic extensions of the dynamical mean field theory. First, we consider the combination of DMFT and FLEX, which is a typical diagrammatic method to treat the superconductivity. We formulate this in terms of the Luttinger-Ward functional, and apply this method to study the superconducting phase [48] and the Pomeranchuk instability [49], which is a kind of charge instability. Finally, to study the vertex

correction effect on nonlocal self-energy and the pairing interaction, we employ the DΓA [41, 50] (dynamical vertex approximation) formalism, and extend it to accommodate superconducting phases.

This thesis is organized as follows. In chapter 2, we introduce the basis of the diagrammatic methods and explain some typical diagrammatic methods for studying superconductivity in tight-binding models. In chapter 3, we explain the dynamical mean field theory, which is a typical non-perturbative method to treat strongly correlated systems. In chapter 4, we introduce the FLEX+DMFT formalism, and apply it to study the superconducting phase diagram for the two-dimensional Hubbard model. In chapter 5, we study the Pomeranchuk instability by employing FLEX+DMFT. In chapter 6, we introduce the DΓA, and study vertex correction effects on the pairing interaction of the two-dimensional Hubbard model.

Chapter 2

Diagrammatic approaches

The Hubbard model described in the previous chapter is difficult to solve exactly and some approximations are needed. Before considering the approximations, we should make clear what quantity we want to obtain, because the full information (e.g. wave functions or density matrix) is too much and we do not need it in many cases.

One of the most basic and important quantities in a correlated electron system is the spectral function $A(\boldsymbol{k}, \omega)$ defined as

$$A(\boldsymbol{k}, \omega) = \frac{1}{Z} \sum_{n,m} \langle n \mid c_{\boldsymbol{k}}^{\dagger} \mid m \rangle \langle m \mid c_{\boldsymbol{k}} \mid n \rangle (e^{-\beta E_m} + e^{-\beta E_n}) \delta(\omega - E_n - E_m), \quad (2.1)$$

where $c_{\boldsymbol{k}}^{\dagger}$ creates an electron with wave vector $\boldsymbol{k}$, ω is the energy, β is the inverse temperature, $\mid m \rangle$ is an eigenstate of the Hamiltonian $\mathcal{H}$ with eigenvalue E_m, and $Z \equiv \sum_m e^{-\beta E_m}$ is the partition function. The spectral function represents occupied and unoccupied single-particle states in the energy and momentum spaces. The density of states ρ is obtained as $\rho(\omega) = \sum_{\boldsymbol{k}} A(\boldsymbol{k}, \omega)$. This quantity has much information beyond the band theory, including the lifetime of the quasi-particle and the incoherent part of the spectral weight. Once we obtain a spectral weight, we can distinguish metals and insulators properly in systems that include Mott insulators. Also, this quantity is directly observed by the angle-resolved photoemission spectroscopy (ARPES) measurement. Therefore obtaining the spectral weight of the target model is one of the main targets in condensed matter physics.

Further important quantities are the susceptibilities, which represent the response against external fields. This cannot be obtained from the one-particle quantity (spectral function), and we need the information in the two-particle level.

In this chapter, we introduce the formalism based on the Green's function, which has the same information as the spectral function $A(\boldsymbol{k}, \omega)$. First, we introduce the Green's function and the self-energy, and then we show the relationship

between the self-energy and the two-particle vertex function according to the equation of motion. Then we review some approximations based on the Feynman diagram for studying superconductivity.

2.1 One-particle quantities

The Green's function is defined as

$$G(\boldsymbol{k},\tau) \equiv -\left\langle T_\tau c_{\boldsymbol{k}}(\tau) c^\dagger_{\boldsymbol{k}}(0)\right\rangle, \tag{2.2}$$

where T_τ is the time-ordering operator and $c_{\boldsymbol{k}}(\tau) = e^{\mathcal{H}\tau} c_{\boldsymbol{k}} e^{-\mathcal{H}\tau}$. With a Fourier transformation, we obtain

$$G(k) = \int_0^\beta d\tau G(\boldsymbol{k},\tau) e^{-i\omega_n \tau}, \tag{2.3}$$

where ω_n is the fermionic Matsubara frequency, and $k = (\omega_n, \boldsymbol{k})$. This quantity is related to the spectral function $A(\boldsymbol{k},\omega_n)$ as

$$G(k) = \int \frac{A(\boldsymbol{k},\omega)}{i\omega_n - \omega} \mathrm{d}\omega, \tag{2.4}$$

which is called the Lehmann representation.

If we ignore the electron correlations the spectral weight is reduced to the non-interacting band dispersion $\epsilon(\boldsymbol{k})$ as

$$A(\boldsymbol{k},\omega) = \delta(\omega - \epsilon(\boldsymbol{k})). \tag{2.5}$$

Then the non-interacting Green's function $G_0(k)$ is

$$G_0(k) = \frac{1}{i\omega_n - \epsilon(\boldsymbol{k})}. \tag{2.6}$$

Also, the sum-rule for the spectral weight, $\int A(\boldsymbol{k},\omega)\mathrm{d}\omega = 1$, gives an asymptotic behavior of the Green's function,

$$G(k) \to \frac{1}{i\omega_n} \ (\omega_n \to \infty). \tag{2.7}$$

The self-energy is defined as $G(k) = G_0(k)[1 - \Sigma(k)G_0(k)]^{-1}$, or

$$\Sigma(k) \equiv G_0^{-1}(k) - G(k)^{-1}, \tag{2.8}$$

which vanishes in the absence of the interaction. In this sense, the self-energy is a measure of the correlation strength. In interacting systems, the spectral function is

$$A(\boldsymbol{k},\omega) = -\frac{1}{\pi}\frac{\mathrm{Im}\Sigma(\boldsymbol{k},\omega)}{[\omega-\epsilon(\boldsymbol{k})-\mathrm{Re}\Sigma(\boldsymbol{k},\omega)]^2+[\mathrm{Im}\Sigma(\boldsymbol{k},\omega)]^2}. \tag{2.9}$$

Thus, roughly speaking, the real part of the self-energy shifts the peak of the spectrum while the imaginary part of the self-energy gives the width of the peak (lifetime of the quasi-particle).

2.2 Two-particle quantities and equation of motion

In this section, we explain how to calculate the self-energy. For simplicity, we consider single-orbital Hubbard model described as

$$\mathcal{H} = t_{ij}\sum_{ij,\sigma}(c^\dagger_{i\sigma}c_{j\sigma}+\mathrm{h.c.}) + U\sum_i n_{i\uparrow}n_{i\downarrow} - \mu\sum_i(n_{i\uparrow}+n_{i\downarrow}), \tag{2.10}$$

where $c^\dagger_{i\sigma}$ and $c_{i\sigma}$ are the creation and annihilation operators with spin σ, respectively, t_{ij} is the hopping amplitude, and $n_{i\sigma} = c^\dagger_{i\sigma}c_{i\sigma}$. The site-represented Green's function is

$$G(\tau : i,j) \equiv -\left\langle T_\tau c_{i,\sigma}(\tau)c^\dagger_{j,\sigma}(0)\right\rangle. \tag{2.11}$$

Then we consider the imaginary time evolution, which is described by the equation of motion as

$$\frac{\partial c_{i\sigma}(\tau)}{\partial\tau} = [\mathcal{H}, c_{i\sigma}(\tau)] = e^{\mathcal{H}\tau}\,[\mathcal{H}, c_{i\sigma}]\,e^{-\mathcal{H}\tau}. \tag{2.12}$$

Calculating the commutation relations, we obtain

$$\frac{\partial c_{i\sigma}(\tau)}{\partial\tau} = -\sum_{l\neq i} t_{il}c_{l\sigma}(\tau) - Uc_{i\sigma}(\tau)c^\dagger_{i\bar{\sigma}}(\tau)c_{i\bar{\sigma}}(\tau) + \mu c_{i\sigma}(\tau), \tag{2.13}$$

where $\bar{\sigma}$ represent the opposite spin to σ. Then the time evolution of the Green's function is given by

$$\begin{aligned}
\frac{\partial G(\tau;i,j)}{\partial\tau} &= -\frac{\partial}{\partial\tau}\left[\theta(\tau)\left\langle c_{i\sigma}(\tau)c^\dagger_{j\sigma}(0)\right\rangle - \theta(-\tau)\left\langle c^\dagger_{j\sigma}(0)c_{i\sigma}(\tau)\right\rangle\right] \\
&= -\delta(\tau)\left\langle\{c_{i\sigma}(\tau), c^\dagger_{j\sigma}(0)\}\right\rangle - \left\langle T_\tau\frac{\partial c_{i\sigma}(\tau)}{\partial\tau}c^\dagger_{j\sigma}(0)\right\rangle \\
&= -\delta(\tau)\delta_{ij} + \sum_{l\neq i} t_{il}G(\tau;l,j) - \mu G(\tau;i,j) \\
&\qquad + U\left\langle T_\tau c_{i\sigma}(\tau)c^\dagger_{i\bar{\sigma}}(\tau)c_{i\bar{\sigma}}(\tau)c^\dagger_{j\sigma}(0)\right\rangle.
\end{aligned} \tag{2.14}$$

With a Fourier transform, we obtain

$$(i\omega_n - \mu)G(\omega_n; i, j) + \sum_{l \neq i} t_{il} G(\omega_n; l, j) = \delta_{ij} - U \int_0^\beta \mathrm{d}\tau \left\langle T_\tau c_{i\sigma}(\tau) c^\dagger_{i\bar{\sigma}}(\tau) c_{i\bar{\sigma}}(\tau) c^\dagger_{j\sigma}(0) \right\rangle e^{i\omega_n \tau}. \quad (2.15)$$

If we define G^{-1} as

$$\sum_j G(\omega_n; i, j) G^{-1}(\omega_n; j, k) = \delta_{ik}, \quad (2.16)$$

then

$$(i\omega_n - \mu)\delta_{ik} + \sum_{l \neq i} t_{il}\delta_{lk} = G^{-1}(\omega_n; i, k) - U \sum_j \int_0^\beta \mathrm{d}\tau \left\langle T_\tau c_{i\sigma}(\tau) c^\dagger_{i\bar{\sigma}}(\tau) c_{i\bar{\sigma}}(\tau) c^\dagger_{j\sigma}(0) \right\rangle G^{-1}(\omega_n; j, k) e^{i\omega_n \tau}. \quad (2.17)$$

From the definition of G_0, we have

$$(i\omega_n - \mu)\delta_{ik} + \sum_{l \neq i} t_{il}\delta_{lk} = G_0^{-1}(\omega_n; i, k). \quad (2.18)$$

Then, the self energy is obtained as

$$\Sigma(\omega_n; i, k) = -U \sum_j \int_0^\beta \mathrm{d}\tau \left\langle T_\tau c_{i\sigma}(\tau) c^\dagger_{i\bar{\sigma}}(\tau) c_{i\bar{\sigma}}(\tau) c^\dagger_{j\sigma}(0) \right\rangle e^{i\omega_n \tau} G^{-1}(\omega_n; j, k). \quad (2.19)$$

Now, the problem is how to calculate this quantity. If we consider the mean-field-like decoupling as

$$\left\langle T_\tau c_{i\sigma}(\tau) c^\dagger_{i\bar{\sigma}}(\tau) c_{i\bar{\sigma}}(\tau) c^\dagger_{j\sigma}(0) \right\rangle \approx \left\langle T_\tau c_{i\sigma}(\tau) c^\dagger_{j\sigma}(0) \right\rangle \left\langle T_\tau c^\dagger_{i\bar{\sigma}}(\tau) c_{i\bar{\sigma}}(\tau) \right\rangle = -G(\tau; i, j)n, \quad (2.20)$$

where n is the density (half of the band filling n_f) , the self-energy becomes

$$\Sigma \approx U n_i \delta_{i,k}. \quad (2.21)$$

This is the Hartree term.

To consider the self-energy effect beyond the mean-field level, we introduce the two-particle Green's function,

$$G_{2,\sigma\sigma'}(\tau_1, \tau_2, \tau_3; i, j, k, l) = \left\langle T_\tau c^\dagger_{i\sigma}(\tau_1) c_{j\sigma}(\tau_2) c^\dagger_{k\sigma'}(\tau_3) c_{l\sigma'}(0) \right\rangle, \quad (2.22)$$

and the fully reducible two-particle vertex F, which satisfies

$$\begin{aligned} &G(k)G(k+q)F_{\sigma\sigma'}(k,k',q)G(k')G(k'+q) \\ &\quad = -G_{2,\sigma\sigma'}(k,k',q) - \beta N_{\boldsymbol{k}}\delta_{k,k'}\delta_{\sigma,\sigma'}G(k)G(k+q) + \beta N_{\boldsymbol{k}}\delta_{q,0}G(k)G(k'), \end{aligned} \tag{2.23}$$

where the Fourier transformed $G_{2,\sigma\sigma'}(k,k',q)$ is defined as

$$\begin{aligned} G_{2,\sigma\sigma'}(k,k',q) =& \frac{1}{N_{\boldsymbol{k}}}\int_0^\beta d\tau_1 d\tau_2 d\tau_3 \sum_{i,j,k,l} G_{2,\sigma\sigma'}(\tau_1,\tau_2,\tau_3;i,j,k,l) \\ &\times e^{-i[\omega_n\tau_1 - \boldsymbol{k}(\boldsymbol{x}_i-\boldsymbol{x}_l)]}e^{i[(\omega_n+\omega_m)\tau_2 - (\boldsymbol{k}+\boldsymbol{q})(\boldsymbol{x}_j-\boldsymbol{x}_l)]}e^{-i[(\omega'_n+\omega_m)\tau_3 - (\boldsymbol{k}'+\boldsymbol{q})(\boldsymbol{x}_k-\boldsymbol{x}_l)]}. \end{aligned} \tag{2.24}$$

Then the self-energy is represented as

$$\Sigma(k) = \Sigma_H - \frac{U}{(\beta N_{\boldsymbol{k}})^2}\sum_{k',q} F_{\uparrow\downarrow}(k,k',q)G(k')G(k'+q)G(k+q). \tag{2.25}$$

This is the relation between the self-energy and the vertex function F which comes from the equation of motion. Meanwhile, we stress that all the quantities and relations are introduced non-perturbatively, so that the above argument still holds even in a strongly correlated regime. One advantage of using the Green's function is that we can use the Feynman diagram. Diagrammatically, Eq. (2.25) is represented as Fig. 2.1.

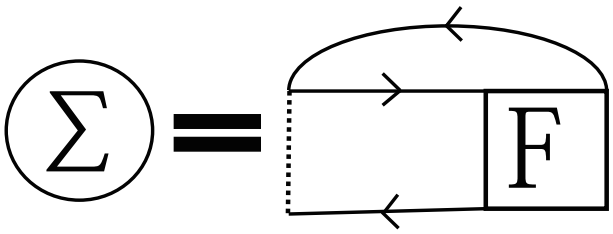

Figure 2.1: Diagrammatic representation of the equation of motion. Σ is the self-energy, while F is the vertex function. The arrow is the Green's function and the dotted line is the interaction. We ignore the Hartree term of the self-energy in this figure.

2.3 Anomalous quantities

For considering superconducting instability, we introduce the anomalous Green's function as

$$F(\boldsymbol{k},\tau) = -\left\langle T_\tau c_{\boldsymbol{k}\uparrow}(\tau)c_{-\boldsymbol{k}\downarrow}(0)\right\rangle, \tag{2.26}$$

which takes a finite value in a superconducting phase. We also introduce the Dyson-Gor'kov equation, which is a Dyson equation extended to include superconducting phases. The equation is described as

$$G(k) = G_0(k) + G_0(k)\Sigma(k)G(k) + G_0(k)\Delta(k)F^\dagger(k), \tag{2.27}$$

$$F(k) = G_0(k)\Sigma(k)F(k) + G_0(k)\Delta(k)G(-k), \tag{2.28}$$

$$F^\dagger(k) = G_0(-k)\Sigma(-k)F^\dagger(k) + G_0(-k)\Delta^*(k)G(k), \tag{2.29}$$

where Δ is the anomalous self-energy which is the gap function up to the renormalization factor.

A diagrammatic representation for the set of equations is displayed in Fig. 2.2.

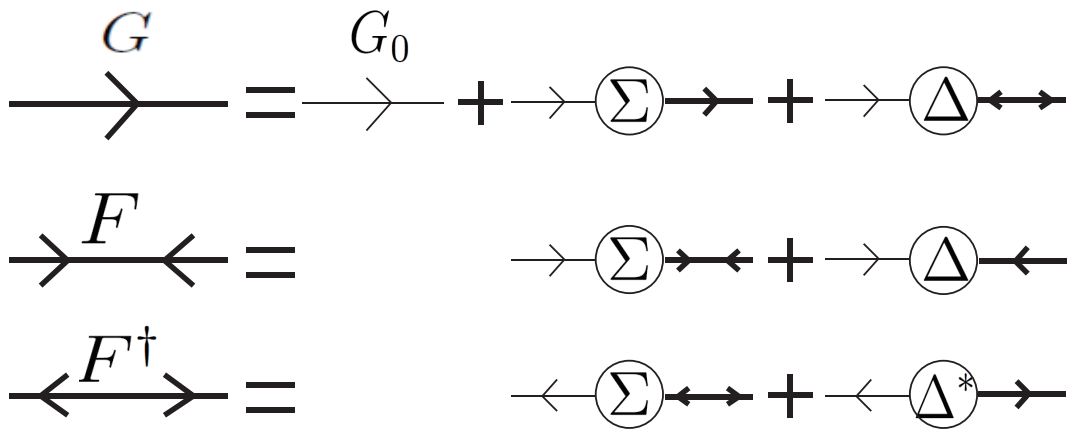

Figure 2.2: Dyson-Gor'kov equation. The thin (bold) arrow represents the non-interacting Green's function (the renormalized Green's function), the right-left arrow and the left-right arrow represent the anomalous Green's functions F and $F^\dagger$, respectively.

In this thesis, we consider a temperature infinitesimally below T_c to discuss the superconducting phase transition. Therefore we can assume that the anomalous Green's function $F(k)$ and the anomalous self-energy $\Delta(k)$ are much smaller than the normal ones. If we take the lowest order in the anomalous contributions, the Dyson-Gor'kov equation becomes

$$G(k) = G_0(k) + G_0(k)\Sigma(k)G(k), \tag{2.30}$$

$$F(k) = G(k)\Delta(k)G(-k), \tag{2.31}$$

$$F^{\dagger}(k) = G(-k)\Delta^{*}(k)G(k). \tag{2.32}$$

2.4 Diagrammatic approximations

2.4.1 Random phase approximation (RPA)

In this section, we review diagrammatic approaches to explore the superconductivity in the repulsive Hubbard model. Scalapino et al. have proposed a spin-fluctuation mediated pairing mechanism for the superconductivity in the Hubbard model by using random phase approximation (RPA) [26]. They showed that, if we consider ladder and bubble diagrams for the pairing interaction (Fig. 2.3), then the d-wave superconducting instability is enhanced toward low temperatures. After this work, there are many attempts to take into account the electron self-energy effect [27, 51, 52]. In the next section, we explain one typical method in these attempts.

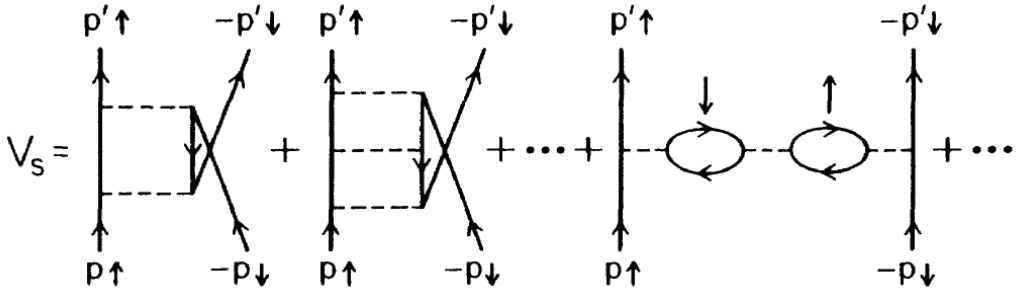

Figure 2.3: Diagrammatic representation of the pairing interaction in RPA. The arrows represent the non-interacting Green's function (from Ref. [26]).

2.4.2 FLEX

The fluctuation exchange approximation (FLEX) is a kind of many-body perturbation theory. FLEX is based on a conserved approximation scheme due to Baym and Kadanoff [53, 54]. In this scheme, we first set the Luttinger-Ward functional $\Phi[G]$ [55], which is directly related the thermodynamic potential Ω (see also Appendix A) as

$$\Omega[G] = \mathrm{Tr}\ [\ln(-G(k)) - G(k)\Sigma(k)] + \Phi[G], \tag{2.33}$$

and the self-energy is determined by

$$\Sigma = \frac{\delta\Phi}{\delta G}. \tag{2.34}$$

Diagrammatically, the exact Luttinger-Ward functional is the sum of all ring diagrams. In FLEX, we take an approximate form of $\Phi[G]$ shown in Fig. 2.4, which represents spin and charge fluctuations.

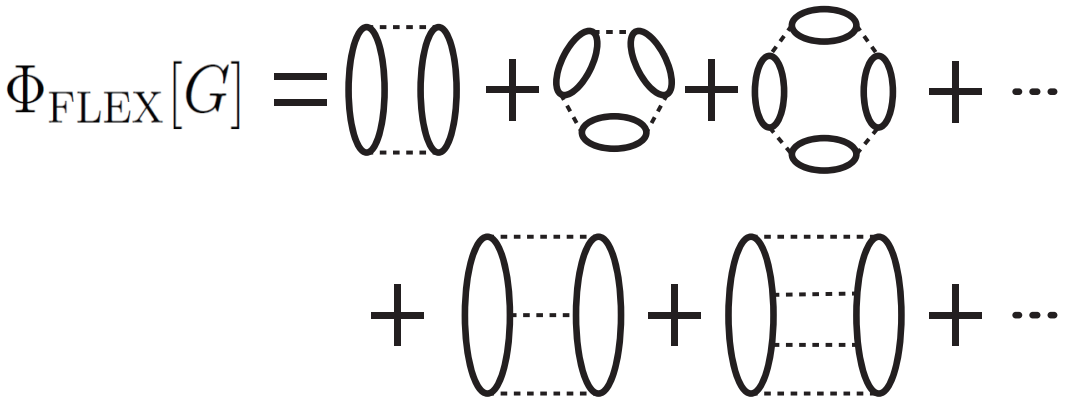

Figure 2.4: Diagrammatic representation of the approximate form of the FLEX-functional Φ_{FLEX}. Solid lines represent the renormalized Green function and dotted lines represent the interactions.

For the two-dimensional Hubbard model, the normal self-energy in FLEX is given as

$$\Sigma(k) = \frac{1}{N_{\boldsymbol{k}}\beta}\sum_{k'}\left[V_{\mathrm{ph}}(k-k')G(k') + V_{\mathrm{pp}}(k-k')G(-k')\right], \tag{2.35}$$

where V_{ph} and V_{pp} are the particle-hole and particle-particle interactions in FLEX, respectively. They are given as

$$V_{\rm ph}(k) = \frac{3}{2}U^2\frac{\chi_0(k)}{1-U\chi_0(k)} + \frac{1}{2}U^2\frac{\chi_0(k)}{1+U\chi_0(k)} - U^2\chi_0(k), \tag{2.36}$$

$$V_{\rm pp}(k) = \frac{U^3\chi_{\rm pp}(k)^2}{1+U\chi_{\rm pp}(k)}, \tag{2.37}$$

where

$$\chi_0(q) = -\frac{1}{N_{\boldsymbol{k}}\beta}\sum_k G(k+q)G(k) \tag{2.38}$$

is the irreducible particle-hole susceptibility, while

$$\chi_{\rm pp}(q) = \frac{1}{N_{\boldsymbol{k}}\beta}\sum_k G(k+q)G(-k) \tag{2.39}$$

is the irreducible particle-particle susceptibility.

We consider the superconductivity mediated by spin fluctuations in the Hubbard model which only has the onsite interaction term. In this case, $\frac{U^2\chi_0(k)}{1-U\chi_0(k)}$, which represents spin fluctuations, is much larger than $V_{\rm pp}$. Therefore we neglect $V_{\rm pp}$ hereafter. $V_{\rm ph}$ is expressed in a diagrammatic representation as in Fig. 2.5.

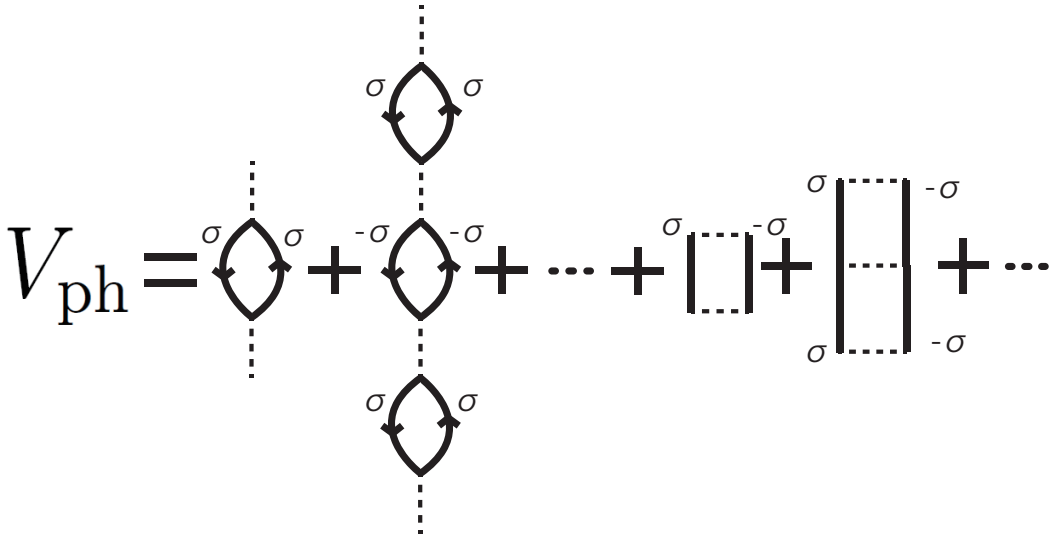

Figure 2.5: Particle-hole interaction in FLEX for the onsite Hubbard model, for which the diagrams with odd numbers of bubbles and ladders are relevant.

Thus the normal self-energy is given as

$$\Sigma(k) = \frac{1}{N_{\boldsymbol{k}}\beta}\sum_{k'}\left[\frac{3}{2}U^2\frac{\chi_0(k-k')}{1-U\chi_0(k-k')} + \frac{1}{2}U^2\frac{\chi_0(k-k')}{1+U\chi_0(k-k')} - U^2\chi_0(k-k')\right]G(k'). \tag{2.40}$$

Then we can obtain the normal Green's function numerically by using Eq. (2.40) and the Dyson equation (Eq. (2.8)).

Next, we focus on the anomalous part. In the FLEX, the anomalous self-energy is given as

$$\Delta(k) = -\frac{1}{N_{\boldsymbol{k}}\beta}\sum_{k'} V_{\text{eff}}(k-k')F(k'), \tag{2.41}$$

where V_{eff} is the effective interaction for the anomalous Green's function. A schematic diagram for this equation is displayed in Fig. 2.6.

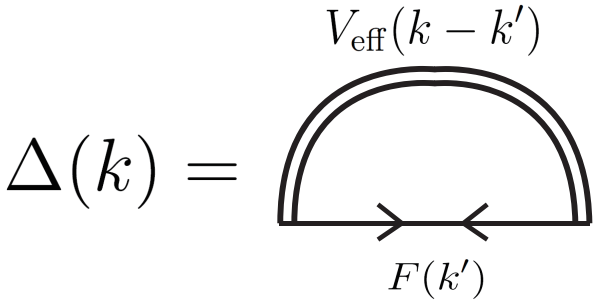

Figure 2.6: Anomalous self-energy in FLEX. A right-left arrow represents the anomalous Green's function F and a double-line represents the effective interaction.

In the FLEX, V_{eff} is given as

$$V_{\text{eff}}(k) = U + \frac{3}{2}U^2\frac{\chi_0(k)}{1-U\chi_0(k)} - \frac{1}{2}U^2\frac{\chi_0(k)}{1+U\chi_0(k)}, \tag{2.42}$$

which is expressed in diagrammatic representation as in Fig. 2.7.

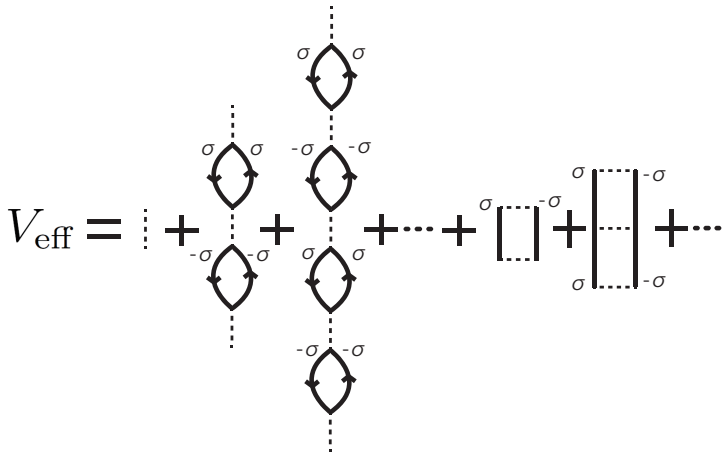

Figure 2.7: Effective interaction for the anomalous Green's function with even numbers of bubbles and ladders.

By using equations (2.31) and (2.41), we obtain an equation for Δ as

$$\Delta(k) = -\frac{1}{N_{\boldsymbol{k}}\beta}\sum_{k'} V_{\text{eff}}(k-k')G(k')G(-k')\Delta(-k'), \tag{2.43}$$

which is called the linearized Eliashberg equation."Linearized" means that we assume that the anomalous part is much smaller than the normal ones, and take only the lowest-order contribution of the anomalous part to consider a temperature infinitesimally below T_c.

To solve this equation numerically, we consider an eigenvalue problem as

$$\lambda\Delta(k) = -\frac{1}{N_{\boldsymbol{k}}\beta}\sum_{k'} V_{\text{eff}}(k-k')G(k')G(-k')\Delta(-k'). \tag{2.44}$$

λ is the eigenvalue for the Eliashberg equation, where the superconducting transition corresponds to the temperature at which $\lambda = 1$.

Chapter 3

Dynamical mean field theory (DMFT)

As explained in chapter 1, the main difficulty in treating the Hubbard model comes from the coexistence of the kinetic term which we can easily realize in the momentum space and the interaction term which we can easily realize in the real space. This suggests that both of weak and strong coupling expansions have some trouble to treat this model properly. Recently, the dynamical mean-field theory, a method which is exact in infinite dimensions is proposed [32, 33, 34]. This method basically can deal with arbitrary coupling strength, and becomes exact in the weak and strong coupling limits. Therefore it is a typical non-perturbative method for describing the Mott transition.

In Fig. 3.1, we show the typical DMFT result for the local spectral weight in the Hubbard model. For this calculation, iterated perturbation theory (IPT) [33, 57] is used for the impurity solver and the Bethe lattice is assumed. We explain details for IPT in section 3.3. We can see in Fig. 3.1 that the incoherent part (satellite peaks) of the spectral weight increases with increasing U. In the bottom panel of the figure for $U/D = 4$ with D being the half of bandwidth, we can see that the system becomes insulating, which signifies the Mott transition.

In this chapter, we explain the framework of the DMFT, and then explain some approaches for solving the impurity problem, which is the bottleneck of this algorithm.

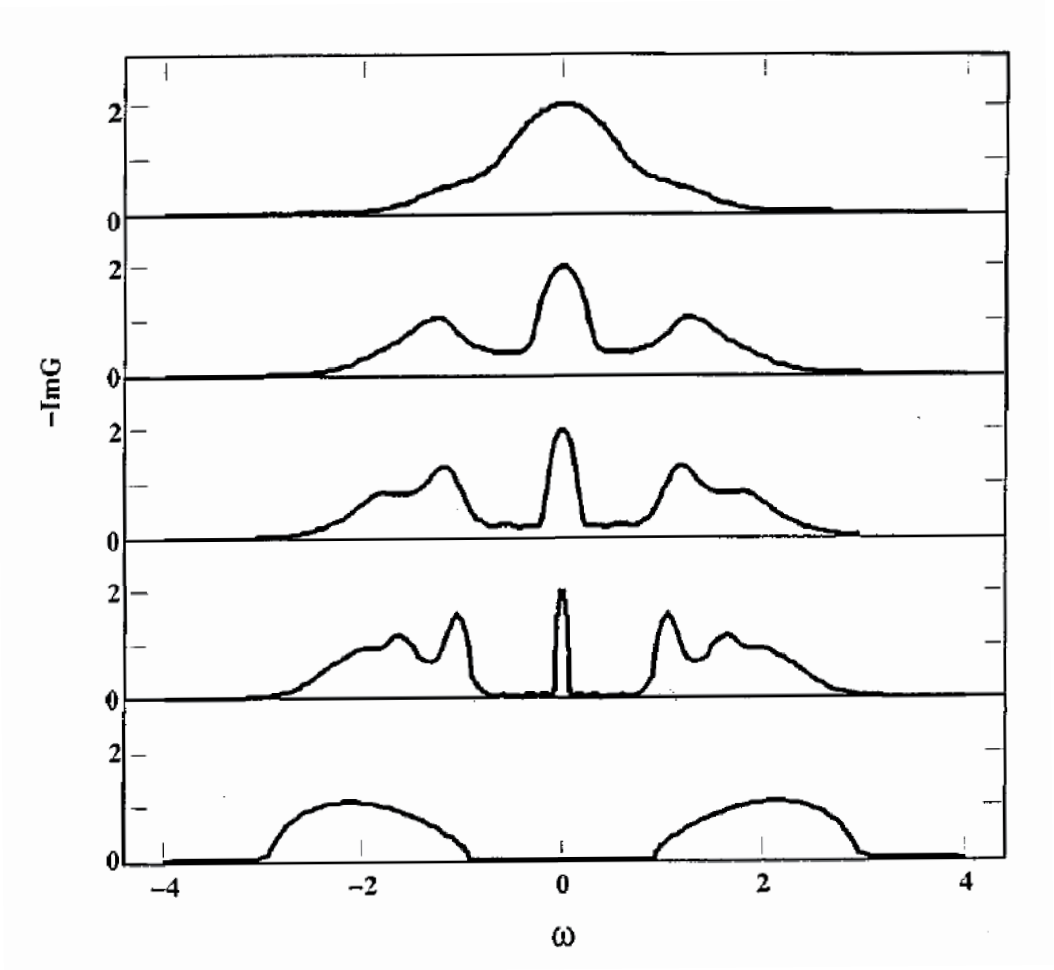

Figure 3.1: Local spectral density, $-\mathrm{Im}G$, against energy ω at temperature $T = 0$ for interaction strength $U/D = 1, 2, 2.5, 3, 4$ (from top to bottom), where D is half the bandwidth. (from Ref. [34])

3.1 Formalism

In this section, we explain the formalism of the DMFT. The DMFT gives the exact electron self-energy in the limit of infinite spatial dimensions. For finite dimensions, it gives an approximate solution that neglects spatial fluctuations. However, the method incorporates temporal fluctuations, which are important in describing the Mott transition.

In the path-integral scheme, the partition function Z for an electron system is expressed as

$$Z = \int \prod_i Dc_i^\dagger Dc_i e^{-S}, \tag{3.1}$$

$$S = \int_0^\beta d\tau \left[\sum_i c_i^\dagger(\tau)\partial_\tau c_i(\tau) + \mathcal{H}(c^\dagger(\tau), c(\tau)) \right], \tag{3.2}$$

where S is the action, $\mathcal{H}$ is the Hamiltonian of the system, and $c^\dagger, c$ are the Grassmann variables.

We take a mean-field approximation, and integrating out all the degrees of freedom except for one site (called o), we obtain the effective action S_{eff} as

$$\frac{1}{Z_{\text{eff}}} e^{-S_{\text{eff}}(c_o^\dagger, c_o)} = \frac{1}{Z} \int \prod_{i \neq o} Dc_i^\dagger Dc_i e^{-S}, \tag{3.3}$$

where Z_{eff} is defined as

$$Z_{\text{eff}} = \int Dc_o^\dagger Dc_o e^{-S_{\text{eff}}}. \tag{3.4}$$

If we take a limit of large spatial dimension $d \to \infty$, we can derive the effective action as

$$S_{\text{eff}} = -\int_0^\beta d\tau \int_0^\beta d\tau' c_o^\dagger(\tau)[\mathcal{G}(\tau - \tau')]^{-1} c_o(\tau') + U \int_0^\beta d\tau n_{o\uparrow}(\tau) n_{o\downarrow}(\tau), \tag{3.5}$$

where $[\mathcal{G}(\tau - \tau')]^{-1}$ is the Weiss function, which includes the effect from local fluctuations [34, 56].

Then the original model (Eq. (3.2)) becomes an impurity model (Eq. (3.5)). To obtain the self-energy of this impurity problem is much easier than the original one. There are many methods (impurity solvers) to solve the impurity problem. We discuss this in detail in section 3.3.

After we solve the impurity problem, we come back to the original lattice model. We ignore the momentum dependence of the self-energy of the lattice model and assume that the Green's function G is given as

$$G(\boldsymbol{k},\omega_n)^{-1} = G_0(\boldsymbol{k},\omega_n)^{-1} - \Sigma_{\rm imp}(\omega_n), \tag{3.6}$$

where $\Sigma_{\rm imp}$ is the self-energy of the mapped impurity model. The local Green's function is given as

$$G_{\rm loc}(\omega_n) = \frac{1}{N_{\boldsymbol{k}}}\sum_{\boldsymbol{k}} G(\boldsymbol{k},\omega_n), \tag{3.7}$$

where $N_{\boldsymbol{k}}$ is the total number of k-points. Then we reproduce the Weiss function from the local Green's function and the local self-energy as

$$\mathcal{G}(\omega_n)^{-1} = G_{\rm loc}(\omega_n)^{-1} + \Sigma_{\rm imp}(\omega_n). \tag{3.8}$$

This equation provides a new Weiss function, which in turn provides a new impurity problem. Therefore, Eq. (3.8) is a self-consistent equation, and we calculate with a self-consistent loop (Fig. 3.2).

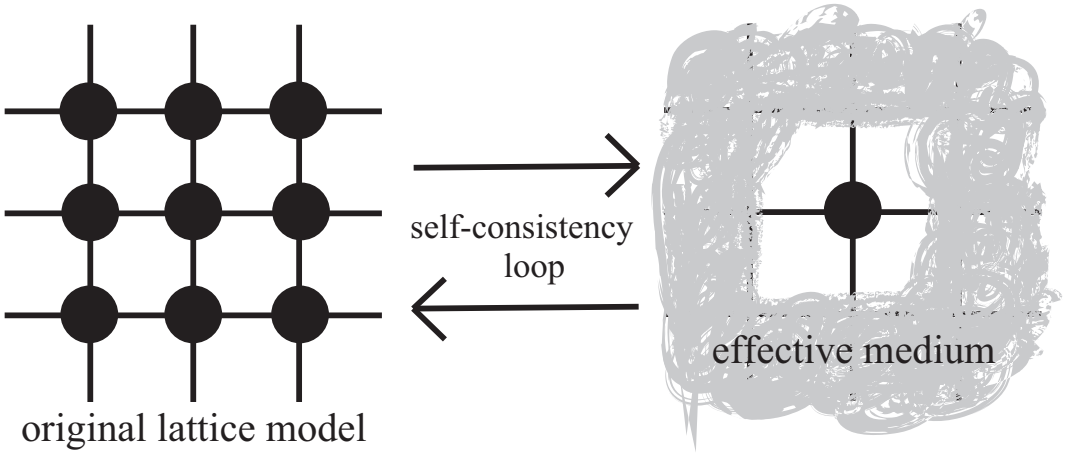

Figure 3.2: Schematic picture of the DMFT loop.

3.2 Functional point of view

Similarly to the FLEX, the DMFT can also be viewed as an approximation for the Luttinger-Ward functional. To see this, we write the action for the original model as

$$S = -\sum_{i,j} \int_0^\beta d\tau \int_0^\beta d\tau' c_i^\dagger(\tau)[G_0(\tau - \tau' : i, j)]^{-1} c_j(\tau') + U \sum_i \int_0^\beta d\tau n_{i\uparrow}(\tau) n_{i\downarrow}(\tau). \tag{3.9}$$

Comparing the action for the impurity model (Eq. (3.5)) and the action for the original Hubbard model (Eq. (3.9)), we realize that the only difference is that the former only involves local propagators, while the latter contains nonlocal propagators. This means that, if we consider a diagrammatic expansion for each system, then the Luttinger-Ward functional Φ_{imp} for the impurity model and that for the original model Φ_{exact} gives the same series except that Φ_{imp} is constructed from local propagator G_{ii} only, while Φ_{exact} is constructed from all the propagators G_{ij}. Therefore we can regard DMFT as an approximation for the Luttinger-Ward functional,

$$\Phi^{\text{DMFT}} = \Phi_{\text{imp}} = \Phi_{\text{exact}}[G_{ii}], \tag{3.10}$$

with the self-energy given as

$$\begin{aligned} \Sigma^{\text{DMFT}} =& \frac{\delta \Phi^{\text{DMFT}}}{\delta G_{ij}} \\ =& \frac{\delta \Phi_{\text{exact}}[G_{ii}]}{\delta G_{ii}}. \end{aligned} \tag{3.11}$$

This is consistent with the previous argument that the DMFT ignores the nonlocal self-energy (spatial fluctuation) effects.

3.3 Impurity solvers

In performing the DMFT procedure, solving the mapped impurity model is the bottleneck of the calculation. While there exist various impurity solvers, we employ the modified IPT (in chapters 4 and 5) and the exact diagonalization method (in chapter 6) in this thesis.

3.3.1 Modified iterative perturbation theory (mIPT)

In this subsection, we explain the iterative perturbation theory (IPT) and its modification for systems that do not have particle-hole symmetries.

The IPT is the simplest way to solve the impurity problem in DMFT. While we use second-order perturbation to solve the impurity problem in this scheme, the IPT is the perturbation theory in the self-consistent loop, and this scheme is expected to describe non-perturbative effects, and it is indeed known to describe the Mott transition in particular. The IPT gives a good result when the system has a particle-hole symmetry. However, we want to investigate the doping dependence of the superconductivity, hence we have to solve the impurity problem away from half-filling. There is an idea for modifying the iterative perturbation theory for non-half-filled cases [58], so that we use this method to solve the impurity problem.

In the original IPT, the self-energy Σ_{IPT} is approximated as

$$\Sigma_{\mathrm{IPT}}(\omega_n) = \Sigma_{\mathrm{H}} - U^2 \int_0^\beta d\tau e^{i\omega_n \tau} \hat{\mathcal{G}}(\tau)^2 \hat{\mathcal{G}}(-\tau), \tag{3.12}$$

where Σ_{H} is the Hartree term, and $\hat{\mathcal{G}}^{-1}$ is defined as

$$\hat{\mathcal{G}}^{-1}(\omega_n) = \mathcal{G}^{-1}(\omega_n) - \frac{U}{2}. \tag{3.13}$$

The IPT self-energy becomes exact in the atomic limit or the high-frequency limit in addition to the weak-coupling limit if the system has a particle-hole symmetry. Away from half-filling, these exact limiting behaviors do not hold, and the original IPT does not work well. There are some proposals to modify the original IPT so as to reproduce some limiting behaviors well even if the system does not have a particle-hole symmetry [58].

In the modified IPT, we first define $\Sigma^{(2)}$ as

$$\Sigma^{(2)}(\omega_n) = -U^2 \int_0^\beta d\tau e^{i\omega_n \tau} \bar{\mathcal{G}}(\tau)^2 \bar{\mathcal{G}}(-\tau), \tag{3.14}$$

where

$$\bar{\mathcal{G}}^{-1}(\omega_n) = \mathcal{G}^{-1}(\omega_n) - \frac{U}{2} - U\delta n \tag{3.15}$$

with δn being a fitting parameter. Then we approximate the self-energy as

$$\Sigma_{\mathrm{IPT}}(\omega_n) = \Sigma_{\mathrm{H}} + \frac{A\Sigma^{(2)}(\omega_n)}{1 - B/U\Sigma^{(2)}(\omega_n)}, \tag{3.16}$$

where A and B are also fitting parameters which should be determined to match the exact self-energy in a few limiting cases (a detailed calculation is described in

appendix B). The Green's function in the impurity problem $G_{\rm imp}$ is obtained by the Dyson equation for the impurity problem as

$$G_{\rm imp}^{-1}(\omega_n) = \mathcal{G}^{-1}(\omega_n) - \Sigma_{\rm IPT}(\omega_n). \tag{3.17}$$

In the high-frequency limit, $\Sigma^{(2)}$ becomes

$$\Sigma^{(2)}(\omega_n) \to \frac{U^2 n_0(1-n_0)}{i\omega_n}, \tag{3.18}$$

where

$$n_0 = \frac{1}{\beta}\sum_{\rm n} \bar{\mathcal{G}}(i\omega_n) e^{i\omega_n 0^+}, \tag{3.19}$$

then $\Sigma_{\rm IPT}$ becomes

$$\Sigma_{\rm IPT}(\omega_n) \to \Sigma_{\rm H} + A\frac{U^2 n_0(1-n_0)}{i\omega_n}. \tag{3.20}$$

On the other hand, the self-energy has an exact high-frequency asymptote,

$$\Sigma_{\rm exact}(\omega_n) \to \Sigma_{\rm H} + \frac{U^2 n(1-n)}{i\omega_n}, \tag{3.21}$$

where

$$n = \frac{1}{\beta}\sum_{\rm n} G_{\rm imp}(i\omega_n) e^{i\omega_n 0^+}. \tag{3.22}$$

Comparing Eq. (3.20) and Eq. (3.21), we obtain A as

$$A = \frac{n(1-n)}{n_0(1-n_0)}. \tag{3.23}$$

In the atomic limit $t/U \to 0$, $\Sigma^{(2)}$ becomes

$$\Sigma^{(2)}(\omega_n) \to \frac{U^2 n_0(1-n_0)}{i\omega_n - (\epsilon-\mu) - U\delta n - U/2}, \tag{3.24}$$

then $\Sigma_{\rm IPT}$ becomes

$$\Sigma_{\rm IPT}(\omega_n) \to \Sigma_{\rm H} + \frac{AU^2 n_0(1-n_0)}{i\omega_n - (\epsilon-\mu) - U\delta n - U/2 - BUn_0(1-n_0)}. \tag{3.25}$$

On the other hand, the exact self-energy in the atomic limit is

$$\Sigma_{\rm exact}(\omega_n) \to \Sigma_{\rm H} + \frac{U^2 n(1-n)}{i\omega_n - (\epsilon-\mu) - U + Un}. \tag{3.26}$$

Comparing Eqs. (3.25) and (3.26), we obtain B as

$$B = \frac{1/2 - n - \delta n}{n_0(1 - n_0)}. \tag{3.27}$$

The remaining fitting parameter is δn, which must vanish in the weak-coupling limit as

$$\delta n \to n - \frac{1}{2} \ (U \to 0). \tag{3.28}$$

However, δn is not determined by Eq. (3.28) alone and there is a freedom of choice to determine δn. A widely used condition to determine δn is to put $n = n_0$ in Eq. (3.15), and it works quite well compared with the exact diagonalize method [59]. So we choose this condition.

We mention that if the system has the particle-hole symmetry, $n = n_0 = 1/2$ and $\delta n = 0$, so that $A = 1$ and $B = 0$, and the scheme is reduced to the original IPT. We use this method in chapters 4 and 5.

3.3.2 Exact diagonalization method (ED)

In DMFT calculation with an exact diagonalization impurity solver [60, 61], we diagonalize the effective Anderson impurity Hamiltonian matrix exactly, and calculate the (one- and two-particle) Green's functions from the Lehmann (spectral) representation. For this diagonalization procedure, we need to reduce the number of the bath sites to a finite number in the impurity model. We note that this does not mean that we deal with a finite size for the original lattice. We consider the Anderson impurity model with finite bath sites,

$$\mathcal{H}_{\rm imp} = \sum_{\sigma,l=1}^{n_s} \epsilon_l a_{l\sigma}^\dagger a_{l\sigma} - \sum_\sigma \mu c_\sigma^\dagger c_\sigma + \sum_{\sigma,l=1}^{n_s} V_l (a_{l\sigma}^\dagger c_\sigma + c_\sigma^\dagger a_{l\sigma}) + U n_\uparrow n_\downarrow, \tag{3.29}$$

where $c_\sigma^\dagger$ (c_σ) is the creation (annihilation) operator at the impurity site, while $a_{l\sigma}^\dagger$ ($a_{l\sigma}$) is the creation (annihilation) operator at a bath site, V_l is the transition matrix element between the impurity site and the bath sites. For a finite number n_s of the bath sites, the Weiss function is given as

$$\mathcal{G}_0^{n_s}(i\omega_n)^{-1} = i\omega_n + \mu - \sum_{l=1}^{n_s} \frac{V_l^2}{i\omega_n - \epsilon_l}, \tag{3.30}$$

and the impurity problem can be solved exactly. The parameters of the Anderson model are determined in such a way that the "distance" defined as

$$d \equiv \frac{1}{n_{\rm max} + 1} \sum_{n=0}^{n_{\rm max}} |\omega_n|^{-\frac{1}{2}} |\mathcal{G}_0(i\omega_n)^{-1} - \mathcal{G}_0^{n_s}(i\omega_n)^{-1}|^2, \tag{3.31}$$

is minimized. The Green's function is computed as

$$G(i\omega_n) = \frac{1}{Z}\sum_{i,j}\frac{\langle i \mid c \mid j\rangle\langle j \mid c^\dagger \mid i\rangle}{E_i - E_j - i\omega_n}(e^{-\beta E_i} + e^{-\beta E_j}), \tag{3.32}$$

where $\mid i\rangle$ is the eigenvector of the impurity Hamiltonian $\mathcal{H}_{\mathrm{imp}}$ with an eigenvalue E_i, and Z is the partition function. Then the self-energy is derived from the Dyson equation for the impurity model (Eq. (3.17)), and the Green's function of the lattice model is obtained through Eq. (3.6).

In chapter 6, we also need to calculate the generalized susceptibility within the DMFT defined as

$$\begin{aligned}\chi_{\mathrm{loc},\sigma\sigma'}(\omega_n,\omega_{n'},\omega_m) \equiv & \frac{1}{\beta^2}\int_0^\beta d\tau_1 d\tau_2 d\tau_3 e^{-i\tau_1\omega_n} e^{i\tau_2(\omega_n+\omega_m)} e^{-i\tau_3(\omega_{n'}+\omega_m)} \\ & \times \Big[\Big\langle T_\tau c^\dagger_{i\sigma}(\tau_1) c_{i\sigma}(\tau_2) c^\dagger_{i\sigma'}(\tau_3) c_{i\sigma'}(0)\Big\rangle \\ & - \Big\langle T_\tau c^\dagger_{i\sigma}(\tau_1) c_{i\sigma}(\tau_2)\Big\rangle \Big\langle T_\tau c^\dagger_{i\sigma'}(\tau_3) c_{i\sigma'}(0)\Big\rangle\Big].\end{aligned} \tag{3.33}$$

This term is calculated with a rather complicated form because we need the Lehmann representation of two-particle quantities, which are shown in Appendix C.

Chapter 4

FLEX+DMFT for superconducting phases

DMFT gives us a new perspective which is exact in the infinite spatial dimensions, where we can ignore the momentum-dependence of the self-energy. This approximation is applicable to arbitrary coupling strength in contrast to weak or strong coupling expansions, which is the main feature of this scheme. The DMFT can describe the Mott insulator as a local correlation effect, but real systems have finite dimensions, and in many cases the momentum-dependence of the self-energy plays important roles. There are many approaches to extend the DMFT for incorporating the momentum-dependence of the self-energy. One of the most successful approaches is the cluster extension of the DMFT. In this approach, the original lattice model is mapped to a few-site cluster model, instead of the one-site impurity problem in the DMFT. This approach is suggested to explain pseudogap phenomena in cuprates as a momentum-dependent Mott transition [39][40]. However, this scheme ignores long-range fluctuations, and we can only take a small-site cluster because numerical effort exponentially grows with the cluster size. It is known to be difficult to obtain converged results against the cluster size at low temperatures [62]. Superconductivity in the two-dimensional Hubbard model appears near the SDW transition points and it is questionable whether we can ignore long-range fluctuations in a situation where spin-fluctuation mediated pairing occurs.

While diagrammatic methods can take account of long-range fluctuation effects, typical diagrammatic methods introduced in section 2.4 are insufficient for reproducing the T_c-dome.

Here, we propose the FLEX+DMFT method as a new approach to overcome this point. The motivation is that local correlation effects, which cause the Mott gap to appear for example, are taken into account by DMFT while the momentum-dependence of effective electron-electron interaction, which is essential for uncon-

ventional superconductivity, is taken into account by FLEX. To put it simply, we combine in this scheme the FLEX self-energy and the DMFT self-energy, and calculate them self-consistently (with a schematic picture displayed in figure 4.1). More precisely, the theory is constructed in terms of the Luttinger-Ward functional.

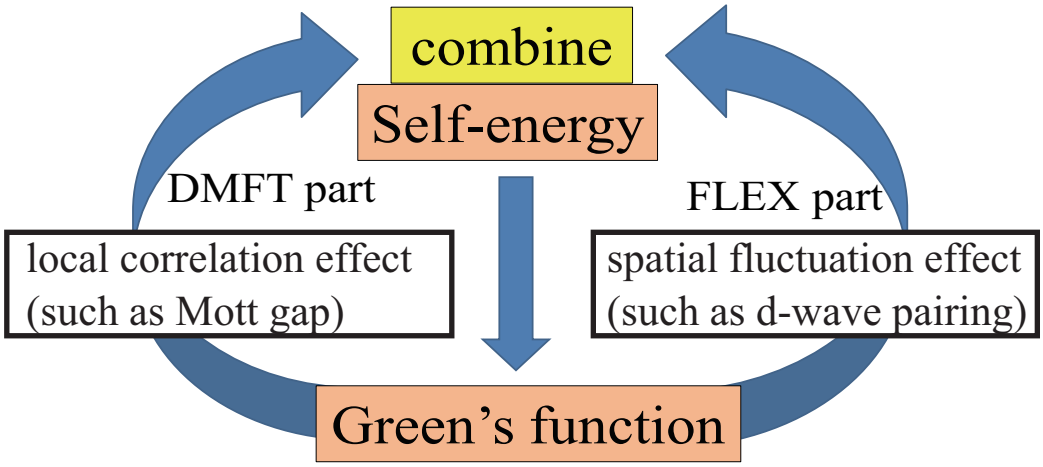

Figure 4.1: Schematic FLEX+DMFT formalism.

In this chapter, we introduce the formulation for the FLEX+DMFT. While this kind of scheme has been considered in Refs. [63, 64], there is ambiguity for the double-counting term, and the calculation is only performed for the normal state. We formulate the present scheme based on the Luttinger-Ward functional so that the double-counting term can be uniquely determined if we impose the conserving nature of the combined method. We then apply this method to discuss the superconductivity in the square-lattice repulsive Hubbard model.

4.1 Formalism

We achieve combining the perturbative FLEX and non-perturbative DMFT through the Luttinger-Ward functional $\Phi[G]$. As mentioned in chapters 2 and 3, we can regard each of the DMFT and the FLEX as an approximation for the Luttinger-Ward functional, $\Phi_{\rm imp}$ and $\Phi_{\rm FLEX}$, respectively. Then we can propose an approximate Luttinger-Ward functional in the FLEX+DMFT formalism, in which we have

$$\Phi_{\rm FLEX+DMFT} = \Phi_{\rm imp}[G_{\rm loc}] + \Phi^{\rm nonloc}_{\rm FLEX}[G], \tag{4.1}$$

$$\Phi^{\rm nonloc}_{\rm FLEX}[G] = \Phi_{\rm FLEX}[G] - \Phi^{\rm loc}_{\rm FLEX}[G_{\rm loc}]. \tag{4.2}$$

Here $\Phi^{\rm loc}_{\rm FLEX}[G_{\rm loc}]$ is the part of the $\Phi_{\rm FLEX}[G]$ diagrams that only contains the local Green's functions $G_{\rm loc}$. Since both $\Phi_{\rm imp}$ and $\Phi_{\rm FLEX}$ are expressed as functionals of the dressed Green's functions, the double counting between the two is uniquely determined as a set of diagrams in $\Phi_{\rm FLEX}[G]$ that only contain the local dressed Green's functions, which is $\Phi^{\rm local}_{\rm FLEX}[G_{\rm loc}]$.

Then we obtain the non-local and local self-energies as functional derivatives of the Luttinger-Ward functional as

$$\Sigma_{ij} = \frac{\delta \Phi^{\rm nonloc}_{\rm FLEX}[G]}{\delta G_{ij}} \ \ (i \neq j), \tag{4.3}$$

$$\Sigma_{ii} = \frac{\delta \Phi_{\rm imp}[G]}{\delta G_{ii}} + \frac{\delta \Phi^{\rm nonloc}_{\rm FLEX}[G]}{\delta G_{ii}}, \tag{4.4}$$

where i and j are site indices.

We note that $\Phi^{\rm nonloc}_{\rm FLEX}[G]$ affects not only the nonlocal self-energy Σ_{ij} but also the local self-energy Σ_{ii}, because the local self-energy Σ_{ii} is constructed not from the local Green's function alone as depicted in Fig. 4.2.

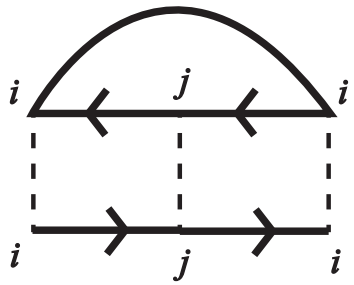

Figure 4.2: An example of the local self-energy diagrams that are obtained from $\Phi^{\rm nonloc}_{\rm FLEX}$.

From the Dyson equation (Eq. (2.8)), the Green's function G and the local Green's function $G_{\rm loc}$ are expressed as

$$G(k) = \frac{1}{G_0(k)^{-1} - \Sigma_{\rm imp}(\omega_n) - \Sigma^{\rm nonloc}_{\rm FLEX}(k)}, \tag{4.5}$$

$$G_{\rm loc}(\omega_n) = \frac{1}{N_{\boldsymbol{k}}} \sum_{\boldsymbol{k}} G(k), \tag{4.6}$$

where $k = (\omega_n, \boldsymbol{k})$, and $\Sigma_{\rm imp}$ and $\Sigma^{\rm nonloc}_{\rm FLEX}$ are defined respectively as

$$\Sigma_{\rm imp} = \frac{\delta \Phi_{\rm imp}[G_{\rm loc}]}{\delta G_{\rm loc}}, \tag{4.7}$$

$$\Sigma^{\rm nonloc}_{\rm FLEX} = \frac{\delta \Phi^{\rm nonloc}_{\rm FLEX}[G]}{\delta G}. \tag{4.8}$$

Now, we have to construct self-consistent loops in the FLEX+DMFT approach. In other words, we have to obtain $\Sigma_{\rm imp}$ and $\Sigma^{\rm nonloc}_{\rm FLEX}$ from G and $G_{\rm loc}$, which are obtained from Eq. (4.7) and Eq. (4.8). Then G and $G_{\rm loc}$ are obtained recursively from Eq. (4.5) and Eq. (4.6).

$\Sigma^{\rm nonloc}_{\rm FLEX}$ is obtained by the FLEX loop which is represented by the right panel in figure 4.1. We can calculate $\Sigma_{\rm FLEX}$ and $\Sigma^{\rm loc}_{\rm FLEX}$ from G and $G_{\rm loc}$, respectively, in the ordinary way (e.g. Eq. (2.40) for the single-band Hubbard model). Then $\Sigma^{\rm nonloc}_{\rm FLEX}$ is obtained as the difference between $\Sigma_{\rm FLEX}$ and $\Sigma^{\rm loc}_{\rm FLEX}$,

$$\Sigma^{\rm nonloc}_{\rm FLEX} = \Sigma_{\rm FLEX} - \Sigma^{\rm loc}_{\rm FLEX}. \tag{4.9}$$

This equation is obtained from the functional derivative in Eq. (4.2).

On the other hand, $\Sigma_{\rm imp}$ is obtained from the DMFT loop, which is represented by the left panel in figure 4.1. In the DMFT, we map the original lattice model to an impurity problem as in Eq. (3.5). According to section 3.3, if the impurity problem in Eq. (3.5) is solved exactly, the resultant Green's function ($G_{\rm output}$) and the self-energy of the impurity problem ($\Sigma_{\rm output}$) satisfy the relations,

$$\Sigma_{\rm output} = \frac{\delta \Phi_{\rm imp}[G_{\rm output}]}{\delta G_{\rm output}}, \tag{4.10}$$

$$G^{-1}_{\rm output} = \mathcal{G}^{-1} - \Sigma_{\rm output}, \tag{4.11}$$

where $\mathcal{G}$ is the Weiss function which characterises the mapped impurity model. We want to connect these quantities in the impurity problem to the self-energy of the original lattice model defined as a functional derivative of $\Phi_{\rm FLEX+DMFT}$. From Eq. (4.10), if the Green's function $G_{\rm output}$ in the impurity problem coincides with the local Green's function $G_{\rm loc}$ of the original lattice model, then the self-energy

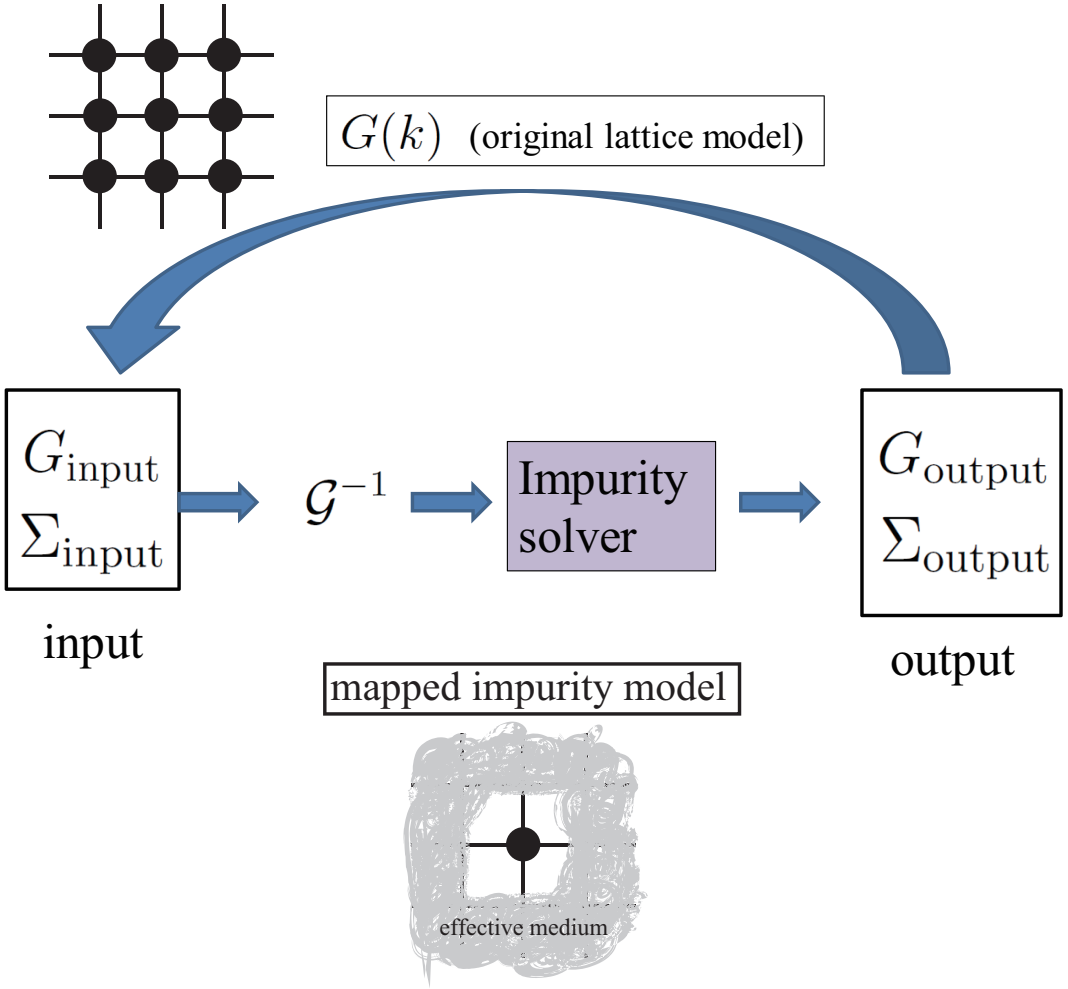

Figure 4.3: Self-consistent loop for the DMFT part.

Σ_{output} in the impurity problem should be the same as Σ_{imp}, which is defined in Eq. (4.7).

Therefore, we construct the self-consistent loop for the DMFT part as in figure 4.3. Namely, we first set an input for the lattice problem as

$$G_{\text{input}} = G_{\text{loc}}, \tag{4.12}$$

$$\Sigma_{\text{input}} = \Sigma_{\text{output}} \text{ (the result of the previous loop)}, \tag{4.13}$$

and define the lattice problem (which means defining $\mathcal{G}$) as

$$\mathcal{G}^{-1} = G_{\text{input}}^{-1} + \Sigma_{\text{input}}, \tag{4.14}$$

and we solve the impurity problem. After solving the impurity problem, we set the Green's function of the original lattice model as

$$G = \frac{1}{G_0^{-1} - \Sigma_{\text{output}} - \Sigma_{\text{FLEX}}^{\text{nonloc}}}. \tag{4.15}$$

From this equation, we obtain the local Green's function G_{loc} from Eq. (4.6), and we then move on to the next iteration.

If the loop in the DMFT part converges, which means $\mathcal{G}$ (the impurity problem) remains the same after further iterations, the resultant self-energy in the impurity problem must remains the same, so that we obtain

$$\Sigma_{\text{input}} = \Sigma_{\text{output}}. \tag{4.16}$$

Then, using Eqs. (4.11) and (4.14), we obtain

$$G_{\text{output}} = G_{\text{loc}}. \tag{4.17}$$

Therefore, Σ_{output} should be the same as Σ_{imp}, and Eq. (4.15) is reduced to Eq. (4.5).

We can then combine the FLEX loop and the DMFT loop to obtain the self-consistent FLEX+DMFT loop as depicted in figure 4.4. This is the double loop which contains the FLEX part and DMFT part.

If the whole loops converge, the result should satisfy Eqs. (4.5), (4.7) and (4.9). We define $\Sigma_{\text{FLEX+DMFT}}$ from the functional derivative of Eq. (4.1),

$$\Sigma_{\text{FLEX+DMFT}} = \Sigma_{\text{imp}} + \Sigma_{\text{FLEX}}^{\text{nonloc}}. \tag{4.18}$$

Then Eqs. (4.5), (4.7) and (4.9) reduce to two equations,

$$\Sigma_{\text{FLEX+DMFT}} = \frac{\delta \Phi_{\text{FLEX+DMFT}}}{\delta G}, \tag{4.19}$$

$$G^{-1} = G_0^{-1} - \Sigma_{\text{FLEX+DMFT}}. \tag{4.20}$$

Therefore, the resultant Green's function in the FLEX+DMFT is the stationary point of the thermodynamic potential, whose Luttinger-Ward functional Φ is approximated as $\Phi_{\text{FLEX+DMFT}}$. Thus, the DMFT+FLEX method is seen to be a kind of conserving approximations.

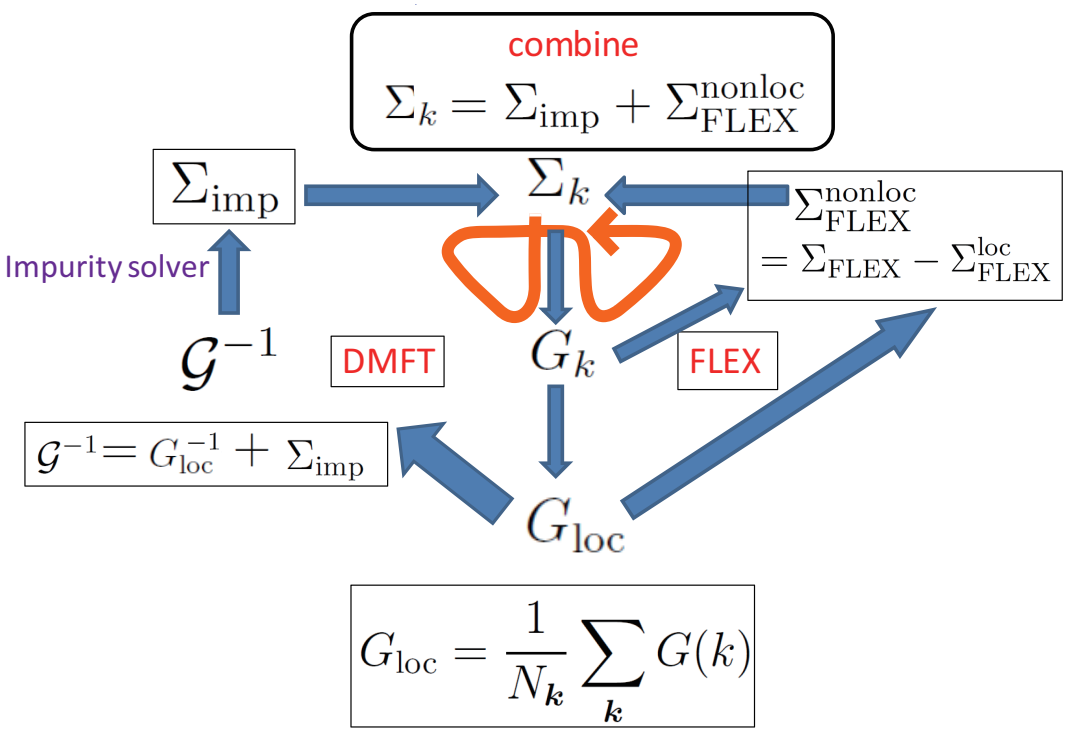

Figure 4.4: Self-consistent double loop in the FLEX+DMFT formalism. In actual calculations, we perform the DMFT loop and the FLEX loop in turns (indicated by the red arrow).

After obtaining the Green's function, we calculate the superconducting T_c. We consider anisotropic pairing on the repulsive model, then superconducting T_c is calculated in the same way as the ordinary FLEX scheme, Eq. (2.44). Here, we comment on the relation between the approximation for the Luttinger-Ward functional and usage of the linearized Eliashberg equation, Eq. (2.44). Similarly to the normal self-energy (Eq. (4.18)), the anomalous self-energy Δ has a DMFT (local) correction term as

$$\Delta_{\mathrm{FLEX+DMFT}} = \Delta_{\mathrm{FLEX}} + \Delta_{\mathrm{loc}}. \tag{4.21}$$

Since we focus on the anisotropic gap function in the repulsive Hubbard model, the isotropic (DMFT) part of the anomalous self-energy Δ_{loc} can be ignored. If we linearize the anomalous part, the remaining term,

$$\Delta_{\mathrm{FLEX}} = \delta\Phi_{\mathrm{FLEX}}[G, F^\dagger, F]/\delta F^\dagger, \tag{4.22}$$

gives the linearized Eliashberg equation (2.43) [65]. In this sense, this formalism treats the normal and anomalous parts on an equal footing in terms of functional derivatives of the same approximate functional. Incidentally, in chapter 5, we consider mixture of the ordinary d-wave and a small extended s-wave pairing. The effect of the DMFT vertex in such a situation is discussed there.

4.2 Superconducting phase diagram

In this section, we apply the FLEX+DMFT to the two-dimensional repulsive Hubbard model and calculate the superconducting T_c. Then, comparing with the FLEX results, we discuss the local correlation effect on d-wave superconductivity.

4.2.1 Phase diagram

In the right panels of Fig. 4.5(a) and(b), we show the superconducting transition temperature of the two-dimensional repulsive Hubbard model in the FLEX+DMFT. The parameters are $t'/t = t''/t = 0$ in Fig. 4.5(a) while $t'/t = -0.20$ and $t''/t = 0.16$ in Fig. 4.5(b). The latter parameters are determined to fit the band calculation of the Hg-based hole-doped cuprate, $HgBa_2CuO_{4+\delta}$ [66, 67]. In the left panels, we show the ordinary FLEX result for comparison. We can see that T_c dome appears in the FLEX+DMFT, both in the absence (panel(a)) and in the presence (panel(b)) of the second and third-neighbor hoppings. In the FLEX, on the other hand, superconducting T_c monotonically increases toward half-filling with some rounding-off [23]. This rounding-off is considered to be due to the fact that the van Hove filling shifts toward a finite doping level as finite (t', t'') are introduced, while the rounding-off disappears if we go to stronger coupling or

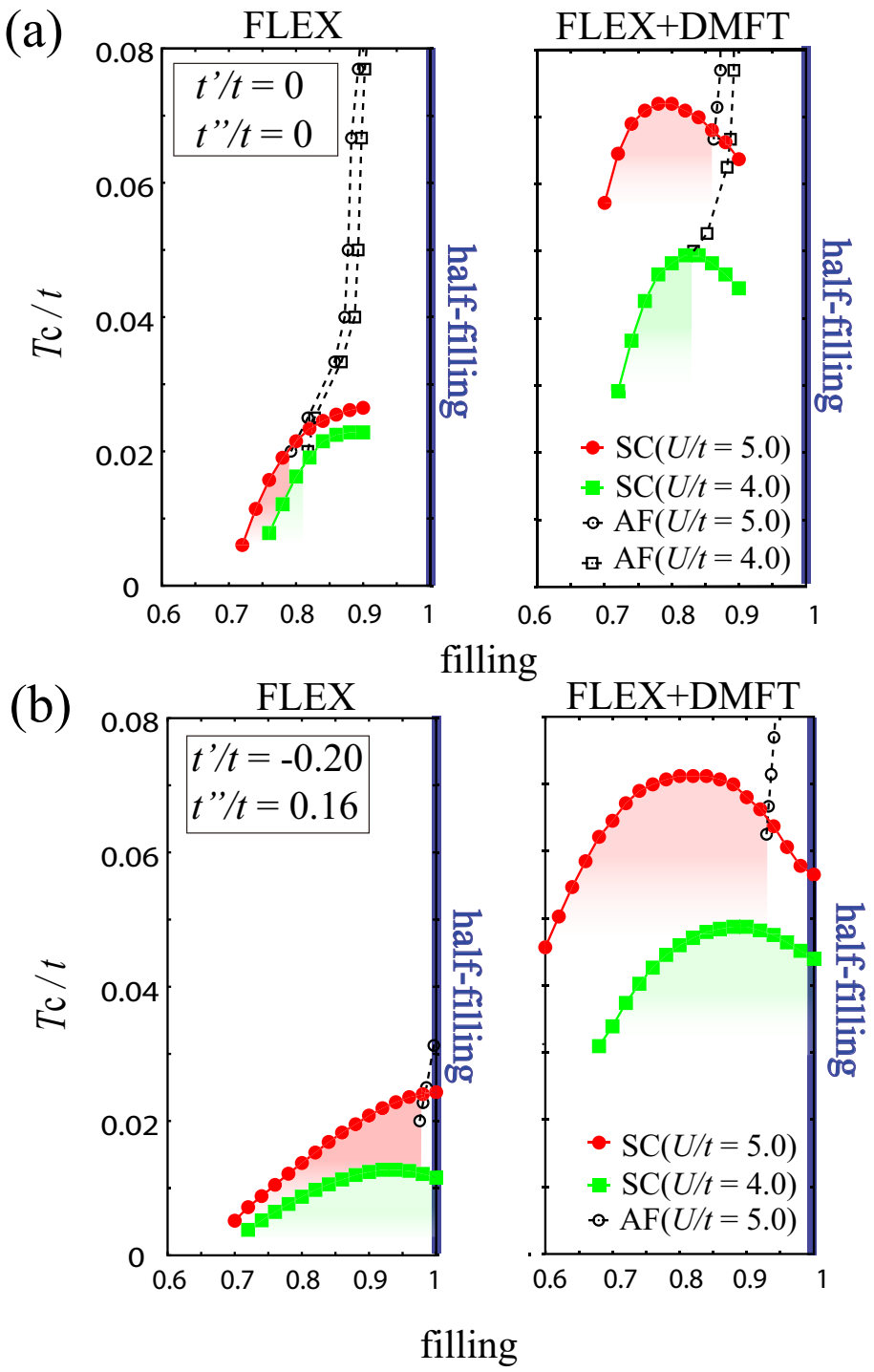

Figure 4.5: Phase diagram against the band filling $n_{\rm f}$ and the temperature T/t in the FLEX+DMFT (right panels) as compared with FLEX (left). Here we take $U/t = 4.0, 5.0$ and (a) $t'/t = t''/t = 0$, or (b) $t'/t = -0.20, t''/t = 0.16$. We also plot the AF phase boundaries (dotted lines) in the normal region, while color shading highlights the superconducting region with $T_c > T_{\rm AF}$ at each filling.

less frustrated regime (smaller t', t''), so that the FLEX is indeed insufficient for describing the T_c-dome structure which is the general nature in cuprates.

Near the half-filling, it is difficult to obtain converged result due to the strong antiferromagnetic (AF) fluctuations for the unfrustrated system ($t'/t = t''/t = 0$). Due to the strong AF fluctuation, it becomes difficult to attain well converged results for large values of U. As a measure of the AF, we plot the antiferromagnetic $T_c^{\rm AF}$ with dashed lines in Fig. 4.5, where $T_c^{\rm AF}$ is estimated as a temperature at which $\max_k[U\chi_0(k)]$ becomes close to unity ($= 0.99$ here). This estimation is often used in FLEX-type schemes for quasi-two-dimensional systems (e.g., layered systems), while FLEX-type schemes are known to satisfy the Mermin-Wagner theorem which prohibits (antiferromagnetic) phase transitions at finite temperatures in purely two-dimensional systems [68]. This (quasi-two-dimensional) antiferromagnetic $T_c^{\rm AF}$ is higher than the superconducting T_c around half-filling as shown in Fig. 4.5.

We also comment on the finite superconducting T_c for the two-dimensional system. While it is well-known that the Mermin-Wagner theorem can be extended to the superconducting phase transitions [69, 70], we regard the present results as the transition temperatures in the quasi-two-dimensional system where the layers are stacked and weakly interacted each other via the Josephson coupling. There, we expect that the transition temperatures in the quasi-two-dimensional systems are mainly determined by the inplane parameters, while the magnitude of a weak interlayer coupling has only a secondary effect, which is observed with FLEX for the superconductivity [71] and the QMC calculations for the antiferromagnetic transition temperatures of the Heisenberg model [72].

The color shaded regions represent superconducting states with $T_c > T_c^{\rm AF}$ (i.e., superconductivity dominating antiferromagnetism). We can see a part of each T_c dome is covered by AF phase both in Fig. (4.5)(a), right ($t'/t = t''/t = 0$) and Fig. (4.5)(b), right ($t'/t = -0.20, t''/t = 0.16, U/t = 5$). This occurs well away from the T_c peak in the latter case.

A similar dome structure in the superconducting order parameter has been obtained with DCA (16-site) for $U/t = 4, T = 0.02t$ [40], but the DCA result strongly depends on the cluster size, where e.g. the superconductivity is absent for the same parameters in the 8-site calculations. The dual-fermion approach also reported the superconductivity around $T_c \approx 0.05t$ for $U/t = 8$ [44], but it is difficult to discuss the T_c dome due to the difficulty in the calculation near the half-filling. A dome structure, at zero temperature, in the order parameter is obtained with the density matrix embedding theory (DMET) for $U/t = 4$ [73] and a variational Monte Carlo (VMC) for $U/t = 10$ [74], while in the latter they reported the phase separation dominates the superconductivity in a wide doping region for this coupling.

Next, we consider physical reason for the emergence of the T_c dome in the

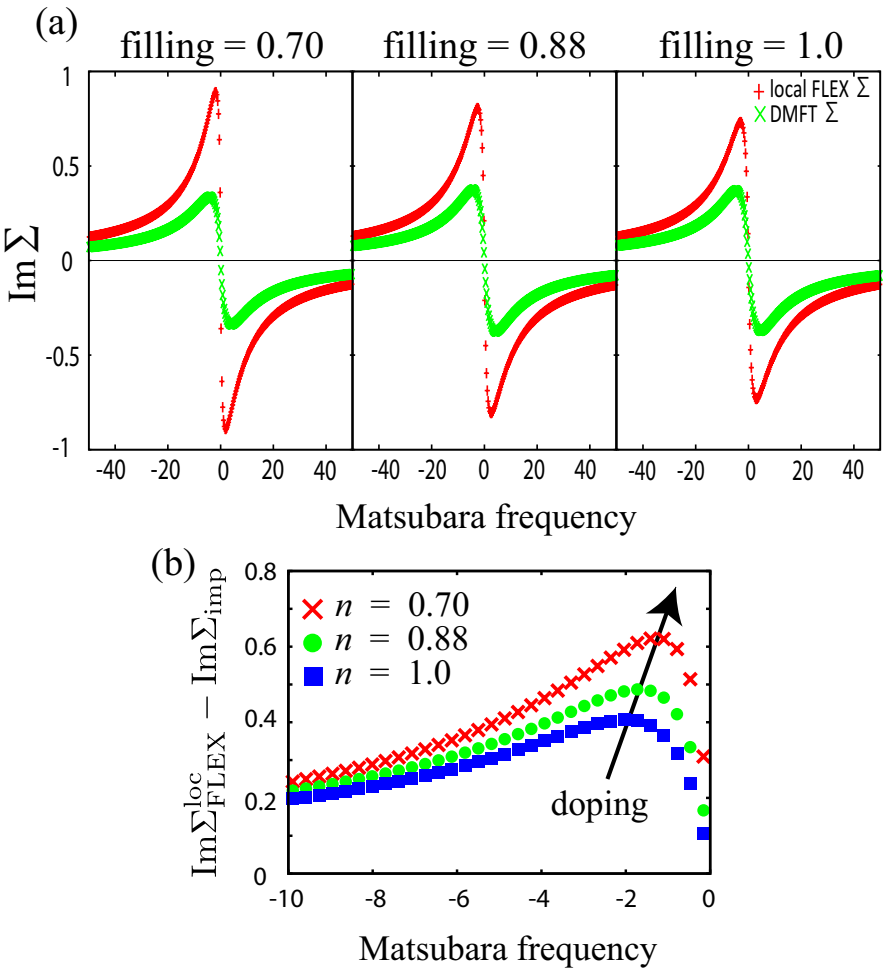

Figure 4.6: (a) Comparison between the FLEX local self-energy $\mathrm{Im}\Sigma^{\mathrm{loc}}_{\mathrm{FLEX}}$ (red plus signs) and the DMFT self-energy $\mathrm{Im}\Sigma_{\mathrm{imp}}$ (green crosses) against the Matsubara frequency for the filling $n_{\mathrm{f}} = 0.70$ (underdoped; left panel), 0.88 (optimally doped; center), and 1.0 (half-filled; right). (b) The difference, $\mathrm{Im}\Sigma^{\mathrm{loc}}_{\mathrm{FLEX}} - \mathrm{Im}\Sigma_{\mathrm{imp}}$, for $n_{\mathrm{f}} = 0.70$ (red crosses), 0.88 (green circles), 1.0 (blue squares). Here we take $U/t = 4.0$, $\beta t = 20$, $t'/t = -0.20$ and $t''/t = 0.16$.

FLEX+DMFT scheme. From Eqs. (4.18) and (4.9), the FLEX+DMFT self-energy is computed as

$$\Sigma_{\mathrm{FLEX+DMFT}} = \Sigma_{\mathrm{FLEX}} - (\Sigma^{\mathrm{loc}}_{\mathrm{FLEX}} - \Sigma_{\mathrm{imp}}), \tag{4.23}$$

which means that the difference between Σ_{FLEX} and $\Sigma_{\mathrm{FLEX+DMFT}}$ amounts to replacing the local FLEX self-energy with the DMFT self-energy $(\Sigma^{\mathrm{loc}}_{\mathrm{FLEX}} - \Sigma_{\mathrm{imp}})$. In Fig. 4.6, we show the respective imaginary parts of $\Sigma^{\mathrm{loc}}_{\mathrm{FLEX}}$ and Σ_{imp} against the Matsubara frequency, for fillings $n_{\mathrm{f}} = 0.7$ (underdoped), 0.88 (optimally doped), and 1.0 (half-filled). The parameters are taken to be $U/t = 4.0, \beta t = 20, t'/t = -0.20, t''/t = 0.16$, which is the same as in the right panel of Fig. 4.5(b). First, we can see the DMFT self-energy, Σ_{imp}, is smaller than that of FLEX, $\Sigma^{\mathrm{loc}}_{\mathrm{FLEX}}$, which implies that the overestimation of the self-energy generally known to exist in FLEX is remedied in FLEX+DMFT by the DMFT (local) vertex corrections. Furthermore, the difference, $\mathrm{Im}\Sigma^{\mathrm{loc}}_{\mathrm{FLEX}} - \mathrm{Im}\Sigma_{\mathrm{imp}}$ [Fig. 4.6(b)], significantly depends on the band filling and increases with doping, which indicates that the magnitude of the self-energy reduction in FLEX+DMFT due to the DMFT correction decreases toward the half-filling (see Eq. (4.23)). Thus T_c tends to be more enhanced when we go away from half-filling because of the *filling-dependent local (DMFT) vertex correction effect* in FLEX+DMFT. On the other hand, the effective pairing interaction mediated by spin fluctuations is stronger near half-filling because of the better band nesting as reflected in the FLEX result [Fig. 4.5, left panels] with T_c almost monotonically increasing toward half-filling. Therefore, in FLEX+DMFT, there are two opposite factors that affect the filling dependence of the transition temperature T_c (i.e., the self-energy reduction effect which enhances T_c away from half-filling vs. the strength of the pairing interaction which becomes stronger toward half-filling), and we can conclude that the appearance of the T_c dome in FLEX+DMFT is due to the *combined effect* of these two factors.

In the present calculation, we do not consider the d-wave pairing fluctuation effect for the self-energy, which is another factor for reducing T_c near the half-filling [75]. If we take account of this effect, we can expect the T_c is more reduced near half-filling, which is closer to the experimental phase diagram of the cuprates.

We also have to note that in the FLEX+DMFT scheme, the overestimated self-energy is remedied only in the local part, while the non-local self-energy is considered to be still overestimated, especially for ladder diagrams [64]. For considering this effect, we compare the FLEX+DMFT with GW+DMFT, where only the bubble diagrams are taken for an approximate Luttinger-Ward functional (while both bubbles and ladders are taken in FLEX+DMFT). We show the phase diagram in GW+DMFT in the right panel of Fig. 4.7 for $t'/t = -0.20$ and $t''/t = 0.16$, where the GW result is displayed on the left for comparison. We can see that a T_c dome also appears in GW+DMFT, but T_c is much reduced from the T_c in FLEX+DMFT. On the other hand, the AF transition temperature in GW+DMFT is higher than that in FLEX+DMFT. This makes the color shaded

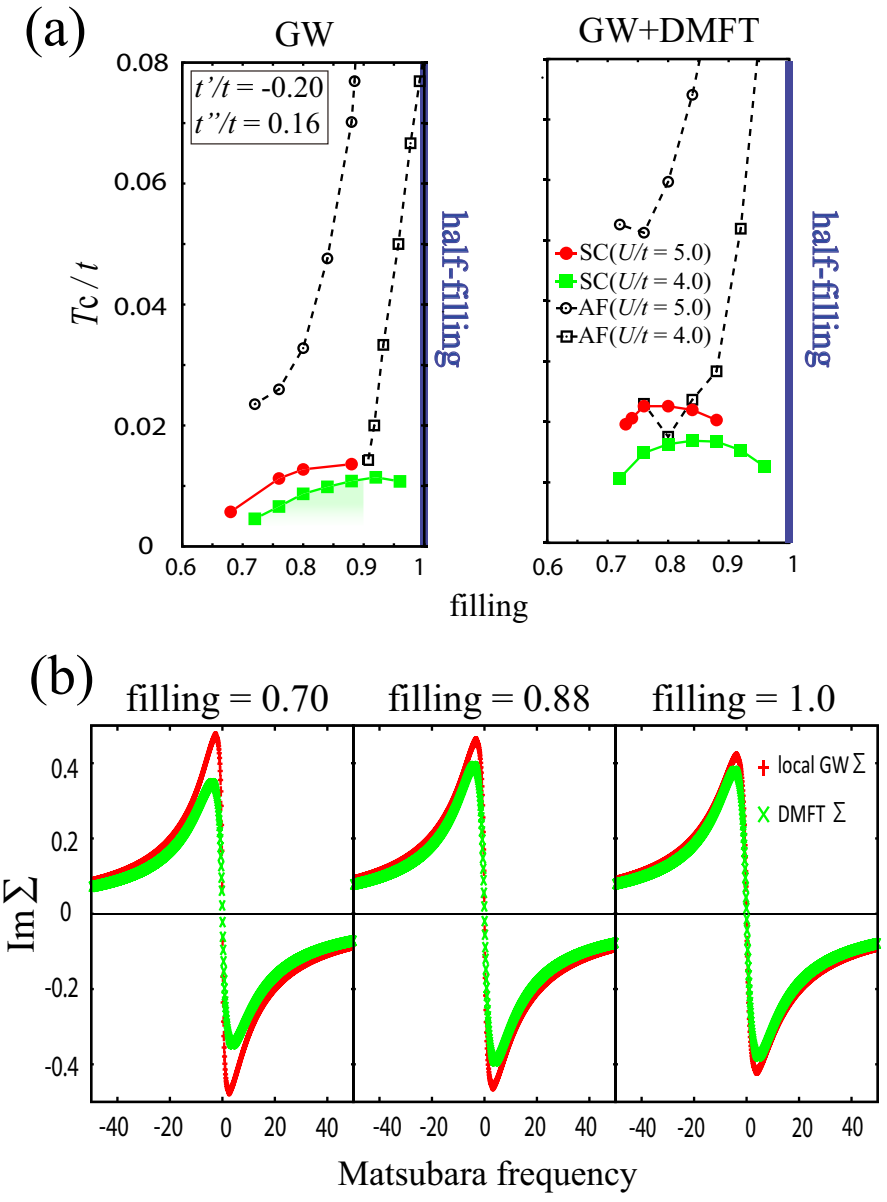

Figure 4.7: (a) Phase diagram against temperature T/t and band filling $n_{\rm f}$ in GW+DMFT approximation (right) as compared with that in GW approximation (left) for $U/t = 4.0$ (green squares) or $U/t = 5.0$ (red circles). (b) Comparison between the GW local self-energy $\mathrm{Im}\Sigma^{\rm loc}_{\rm GW}$ (red plus signs) and the DMFT self-energy $\mathrm{Im}\Sigma_{\rm imp}$ (green crosses) for the filling $n_{\rm f} = 0.70$ (left panel), 0.88 (center), and 1.0 (right) with $U/t = 4.0$ and $\beta t = 50$. Here we take $t'/t = -0.20$, $t''/t = 0.16$. We also plot antiferromagnetic (AF) phase boundaries (dotted lines) in the normal region, while color shading highlights the dome in the region where T_c is above the AF boundary.

region (for $T_c > T_c^{\mathrm{AF}}$) very narrow in GW+DMFT. Actually, for unfrustrated system ($t' = t'' = 0$), the AF fluctuation is so strong that we cannot even obtain superconducting phase boundaries.

Similarly to the FLEX+DMFT case, let us compare the GW local self-energy $\mathrm{Im}\Sigma_{\mathrm{GW}}^{\mathrm{loc}}$ and the DMFT self-energy $\mathrm{Im}\Sigma_{\mathrm{imp}}$ for the filling $n_{\mathrm{f}} = 0.70, 0.88, 1.0$ with $U/t = 4.0$ and $\beta t = 50$ in Fig. 4.7(b). The difference in the two self-energies is seen to decrease toward half-filling, which is the same trend with those in the FLEX+DMFT. Therefore, we can conclude that the appearance of T_c dome is not an artifact in FLEX+DMFT, but is robust in both FLEX+DMFT and GW+DMFT arising due to the same local self-energy correction effect. The overestimation of non-local self-energy thus does not affect the existence of the T_c dome itself. The fact that T_c is much lower in GW+DMFT than in FLEX+DMFT comes from ignoring the ladder diagrams in GW+DMFT. In this sense, GW+DMFT is closer to the mean-field theory than FLEX+DMFT, which is also reflected in the higher AF transition temperature in GW+DMFT. Concomitantly, the pairing interaction mediated by spin fluctuations is reduced, which acts to reduce the superconducting T_c in GW+DMFT than in FLEX+DMFT.

4.2.2 Double occupancy

As another important quantity in correlated electron systems, we measure the double occupancy. From Eq. (2.19), the double occupancy $\langle d \rangle \equiv \langle n_{i\uparrow} n_{i\downarrow} \rangle$ can be calculated as

$$\begin{aligned}\langle d \rangle =& \frac{1}{\beta U} \sum_{\omega_n} e^{i\omega_n 0^+} \sum_j \Sigma(\omega_n; i, j) G(\omega_n; , j, i) \\ =& \frac{1}{U} \mathrm{Tr}(\Sigma G). \end{aligned} \tag{4.24}$$

If we only consider the Hartree term $\Sigma = Un$ for the self-energy, the double occupancy takes $\langle d \rangle = n^2$, which is the value in the weak-coupling limit (i.e., independent up-spin and down-spin electrons). As we increase the Hubbard interaction from the weak-coupling limit, the double occupancy decreases in general, hence the double occupancy measures the strength of the correlation effect. In Fig. 4.8, we can see the double occupancy within the FLEX takes negative values in the overdoped region, which is unphysical. In FLEX+DMFT, on the other hand, this unphysical behavior disappears. We can regard this improvement as another effect of the local self-energy reduction (i.e., the correlation effect, overestimated in the FLEX is improved by combining it with the DMFT). There is a similar behavior between the double occupancy in GW and that in GW+DMFT, but the difference is smaller. This is consistent with the results in the previous

section that the self-energy reduction effect is smaller for GW and GW+DMFT [see Fig. 4.6(a) and Fig. 4.7(b)].

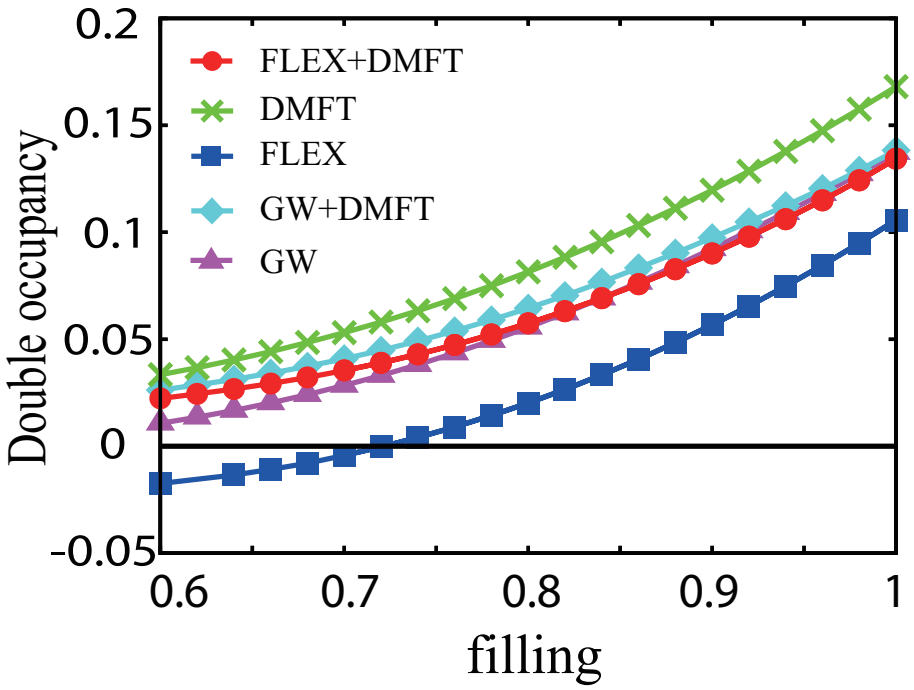

Figure 4.8: Double occupancy against band filling $n_{\rm f}$ in the FLEX+DMFT (red circles), DMFT (green crosses), FLEX (blue squares), GW+DMFT (light blue diamonds) and GW (purple triangles). Here we take $U/t = 4.0$, $\beta t = 20$, $t'/t = -0.20$ and $t''/t = 0.16$.

4.2.3 Spectral weight

Next, we turn to discuss the spectral weight, which is computed via Padé approximation as a numerical analytical continuation (explained in appendix D). In Fig. 4.9, we show the spectral function in FLEX+DMFT, FLEX, GW+DMFT, GW and DMFT at three different fillings ($n_{\rm f} = 0.70, 0.88, 1.0$). The filling dependence is similar among FLEX, GW and DMFT (right panels in Fig. 4.9) in that we have a single peak that slightly shifts and broadens toward the half-filling in each case. On the other hand, the shape of the spectral function strongly depends on the band filling in FLEX+DMFT and GW+DMFT, and a double peak structure appears at the half-filling. Similar double-peaks have been reported in the dual-fermion method [77], where the emergence of this structure is consistent with the lattice QMC result. We can see that both of the local and non-local

long-range correlation effects are important to describe the double-peak structure, which is considered to be a precursor of the Hubbard bands with two peaks separated by about U, while the system is metallic. We mention that due to the strong fluctuation, it is difficult to perform calculation for the insulating region.

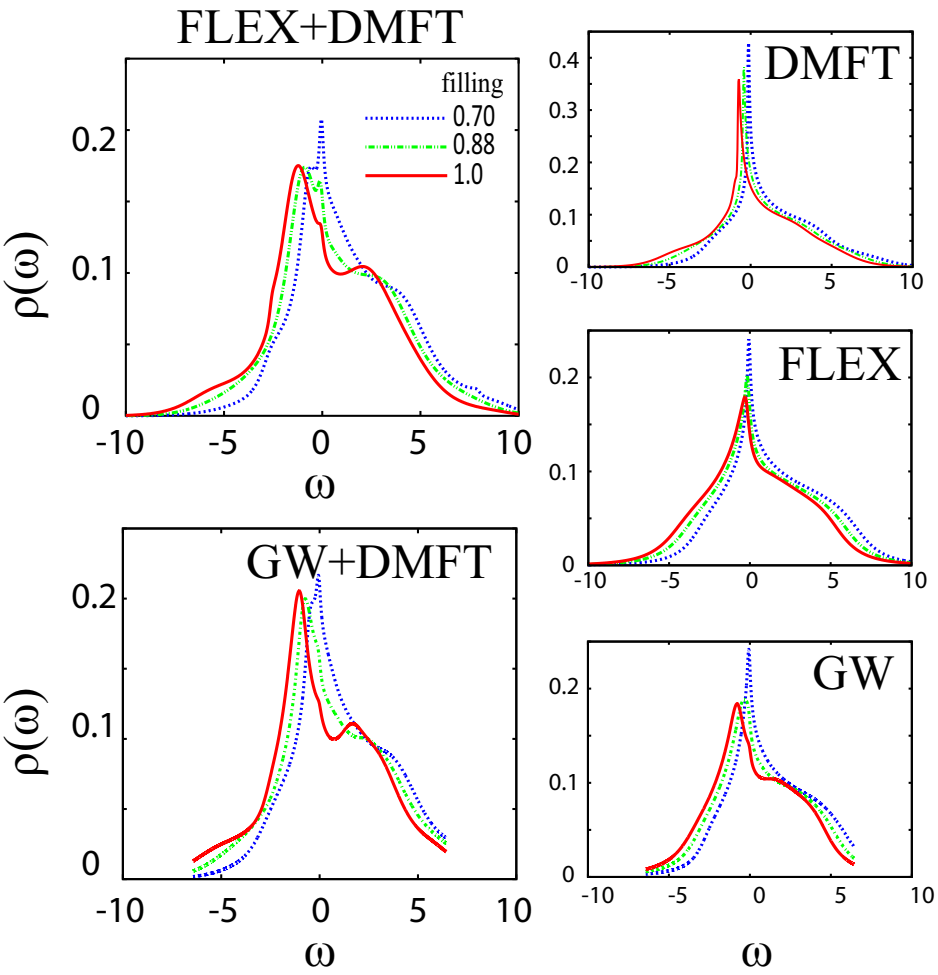

Figure 4.9: Spectral functions at filling $n_{\rm f} = 0.70$ (underdoped; blue lines), 0.88 (optimally doped; green), 1.0 (half-filling; red) in the FLEX+DMFT (top left) or GW+DMFT (bottom left) are compared with those in DMFT (top right), FLEX (middle right) and GW (bottom right). Here we take $U/t = 4.0$, $\beta t = 20$, $t'/t = -0.20$ and $t''/t = 0.16$.

If we look closely at the momentum-resolved spectral function $A(\boldsymbol{k}, \omega)$ (not shown), we observe a region of slightly negative spectral weight away from the Fermi surface. Since the magnitude of the negative part is negligibly small ($< 1\%$) in the present calculation, this does not affect the phase diagram and the density

of states [Figs. 4.5 and 4.9]. We mention that many diagrammatic extensions of DMFT do not guarantee positive-definite spectral weights [50, 76, 78].

Chapter 5

Pomeranchuk instability

As mentioned in chapter 1, there is growing realization that charge instabilities also exist in cuprate superconductors. There are various kinds of charge instabilities, for which some experimental results suggest electron nematic states in cuprates, and theoretically, the effect of nematicity on the quasiparticle excitation for the d-wave superconductivity is studied phenomenologically [79, 80]. There are some explanations for the nematicity, e.g. in the context of fluctuating stripe orders [81]. The Pomeranchuk instability, spontaneous breaking of the four-fold symmetry of the Fermi surface without lattice distortion, is evoked as another possible candidate for the nematicity in cuprate superconductors [82].

Theoretically, the existence of the Pomeranchuk instability in two-dimensional lattice systems has been proposed in Refs. [83, 84], where the forward scattering was found to induce this instability. After that, the Pomeranchuk instability has been studied mainly in mean-field models (called "f-model"), where the forward scattering is only considered for the interaction [85, 86]. For the two-dimensional square lattice Hubbard model, the existence of this instability is yet to be fully clarified. Functional renormalization group (fRG) calculations suggest that the superconducting fluctuation is stronger than the Pomeranchuk instability [87], while other numerical renormalization-group approaches suggest the Pomeranchuk instability to be stronger around van Hove fillings [88]. The Gutzwiller wave functions combined with an efficient diagrammatic expansion technique (DE-GWF) produces a ground state where the superconductivity coexists with this nematicity [89]. Also, the dynamical cluster approximation (DCA) and cellular dynamical-mean-field theory (CDMFT) showed large response against small distortions of the lattice [90, 91], from which a possibility of spontaneous symmetry breaking is suggested to occur at lower temperatures or for larger cluster sizes. While these results suggest that the two-dimensional square-lattice Hubbard model has a strong tendency toward the Pomeranchuk instability, whether this instability is stronger than the superconductivity (i.e., $T_c^{\mathrm{PI}} > T_c^{\mathrm{SC}}$) has to be examined. Furthermore, whether they are cooperative or competing is an intriguing question. While the

study for the mean-field model suggests that they are competing with each other with T_c^{SC} suppressed in the coexistence region [92], the relation should be studied beyond mean-field levels.

Given this situation, here we apply FLEX+DMFT for studying the interplay of the Pomeranchuk instability and superconductivity in the two-dimensional repulsive Hubbard model. Compared with the conventional methods which have been used for studying the Pomeranchuk instability, the present method has, first, no finite-size effects in contrast to DCA and CDMFT, which should be important for capturing small Fermi surface deformations, and second, we can treat finite-temperature regions in contrast to DE-GWF to capture the effect of this nematicity on the superconducting T_c^{SC}. This also enables us to systematically examine the relation between superconductivity and the Pomeranchuk instability for various hopping parameters. In this framework, we can discuss superconductivity for finite distortions, because we deal with finite Pomeranchuk order parameters, while we linearize anomalous quantities.

5.1 Pomeranchuk order parameter

The order parameter of the Pomeranchuk instability, for tetragonal systems such as the square lattice, is defined as

$$\eta = \sum_{\boldsymbol{k}} (\cos k_y - \cos k_x) \left\langle c_{\boldsymbol{k}}^{\dagger} c_{\boldsymbol{k}} \right\rangle . \tag{5.1}$$

We show the FLEX+DMFT result for the temperature and filling dependences of η in Fig. 5.1. To allow the Pomeranchuk instability to occur, we introduce a seed to deform the Fermi surface in the initial input for the Green's function as

$$G_{\mathrm{input}}(k) = \frac{1}{i\omega_n - \epsilon(\boldsymbol{k}) + \delta(\cos k_x - \cos k_y)}, \tag{5.2}$$

where δ is the magnitude of the initial small distortion. We set $\delta = 0.05t$ in the present study. In Fig. 5.1(a), we can see that the order parameter starts to grow continuously with decreasing temperature, which indicates a second-order phase transition. To check the validity of mIPT solver employed here, we have confirmed that the continuous-time quantum Monte Carlo (CT-QMC) impurity solver [93, 94] gives basically similar results to mIPT even away from half-filling in the intermediate-coupling regime [see Fig. 5.1(a)], by using the ALPS library [95, 96]. If we turn to the filling dependence, we observe the order parameter abruptly growing around the edges of the Pomeranchuk phase [see Fig. 5.1(b),(c),(d)], indicative of transferring to the first-order phase transition consistently with the previous work [85]. Hereafter, we focus on the filling region around the peak of

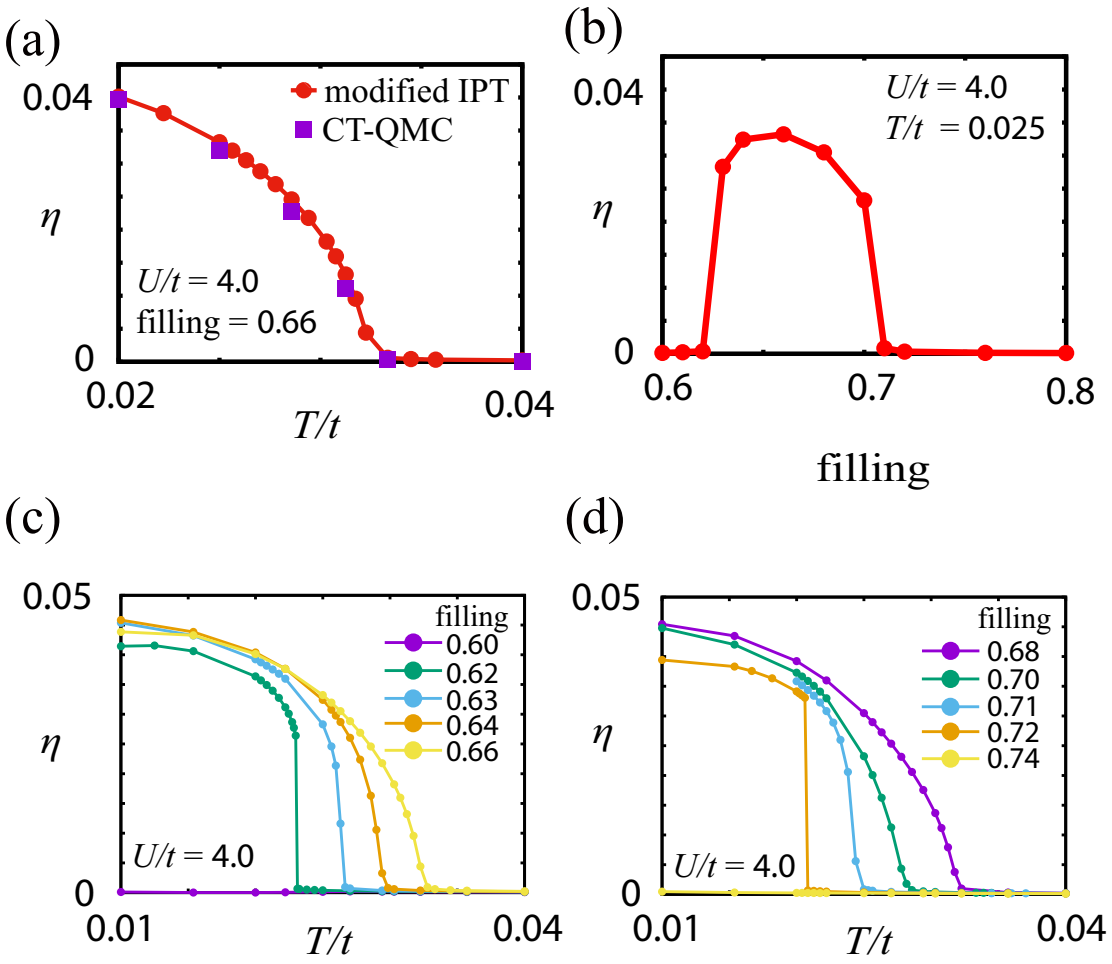

Figure 5.1: (a) Temperature dependence (for $n_{\rm f} = 0.66$), and (b) filling dependence (for $T = 0.025t$) of the Pomeranchuk order parameter η for $U/t = 4.0, (t', t'') = (-0.20, 0.16)$. In (a), the circles and squares correspond to the results of FLEX+DMFT using the modified IPT and CT-QMC as a DMFT impurity solver, respectively. (c),(d) T-dependence of η for $0.60 < n_{\rm f} < 0.66$(c) or $0.68 < n_{\rm f} < 0.74$ (d).

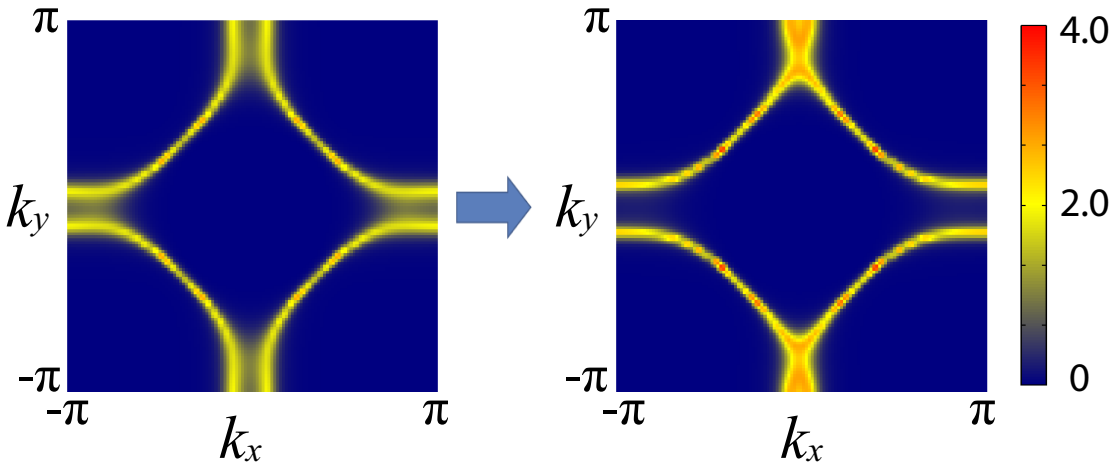

Figure 5.2: Fermi surface [as represented by the color-coded spectral weight $A(\boldsymbol{k}, \omega = 0)$] with $n_{\rm f} = 0.66, U/t = 4.0, (t', t'') = (-0.20, 0.16)$, for $T = 0.0333t > T_c^{\rm PI}$ ($\beta t = 30$; left) and $T = 0.0286t < T_c^{\rm PI}$ ($\beta t = 35$; right).

$T_c^{\rm PI}$, where the transition is of second order. The peak sits around $n_{\rm f} = 0.66$ for the value of the parameter considered ($U/t = 4.0, (t', t'') = (-0.20, 0.16)$). If we look at the Fermi surface in Fig. 5.2, we can see that the Fermi surface, identified as the ridges in the spectral function $A(\boldsymbol{k}, \omega = 0)$, indeed becomes distorted at lower temperatures, $T < T_c^{\rm PI}$.

5.2 Phase diagram

We show the obtained phase diagram in Fig. 5.3(a). We can see that the Pomeranchuk phase transition temperature is peaked around $n_{\rm f} = 0.66$ for $(t', t'') = (-0.20, 0.16)$. An yellow arrow indicates the van Hove filling in the interacting system where the density of states is peaked at the Fermi energy. In Fig. 5.3(b), we show the density of states obtained with Padé approximation. We can see that the peak position exists at the Fermi energy. (We also confirmed that the peak position does not change for $T > T_c^{\rm PI}$). In the previous works with a mean-field model [85, 92], the Pomeranchuk instability is strong near the van Hove filling. In the present work, the peak in the Pomeranchuk dome does not precisely coincide with the van Hove filling, which may be an effect of the asymmetric density of states [85] as in Fig. 5.3(b), or the filling dependence of the effective interaction for the Pomeranchuk instability. More importantly, the superconducting $T_c^{\rm SC}$ monotonically increases toward low-doping regime around the van Hove filling.

In the previous study with a mean-field model [92] that does not take account of the filling dependence of the effective pairing interaction, both $T_c^{\rm SC}$ and $T_c^{\rm PI}$ are

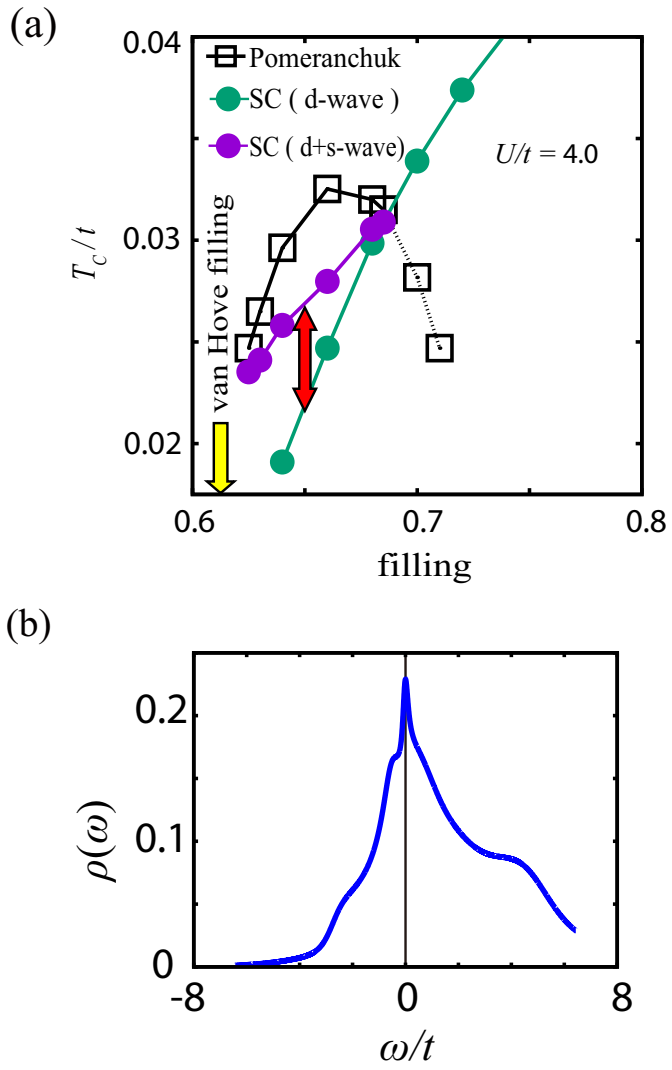

Figure 5.3: (a) Phase diagram against temperature T/t and band filling $n_{\rm f}$ for $U/t = 4.0, (t', t'') = (-0.20, 0.16)$. We show the superconducting $T_c^{\rm SC}$ with undistorted Fermi surface (green circles), superconducting $T_c^{\rm SC}$ with Fermi surface distortion (purple circles), and Pomeranchuk $T_c^{\rm PI}$ (open squares). The dotted line represents $T_c^{\rm PI}$ when we ignore the superconductivity. The yellow arrow indicates the van Hove filling in the interacting system. (b) Density of states at the filling indicated by the yellow arrow in (a) for $\beta t = 20, U/t = 4.0, (t', t'') = (-0.20, 0.16)$.

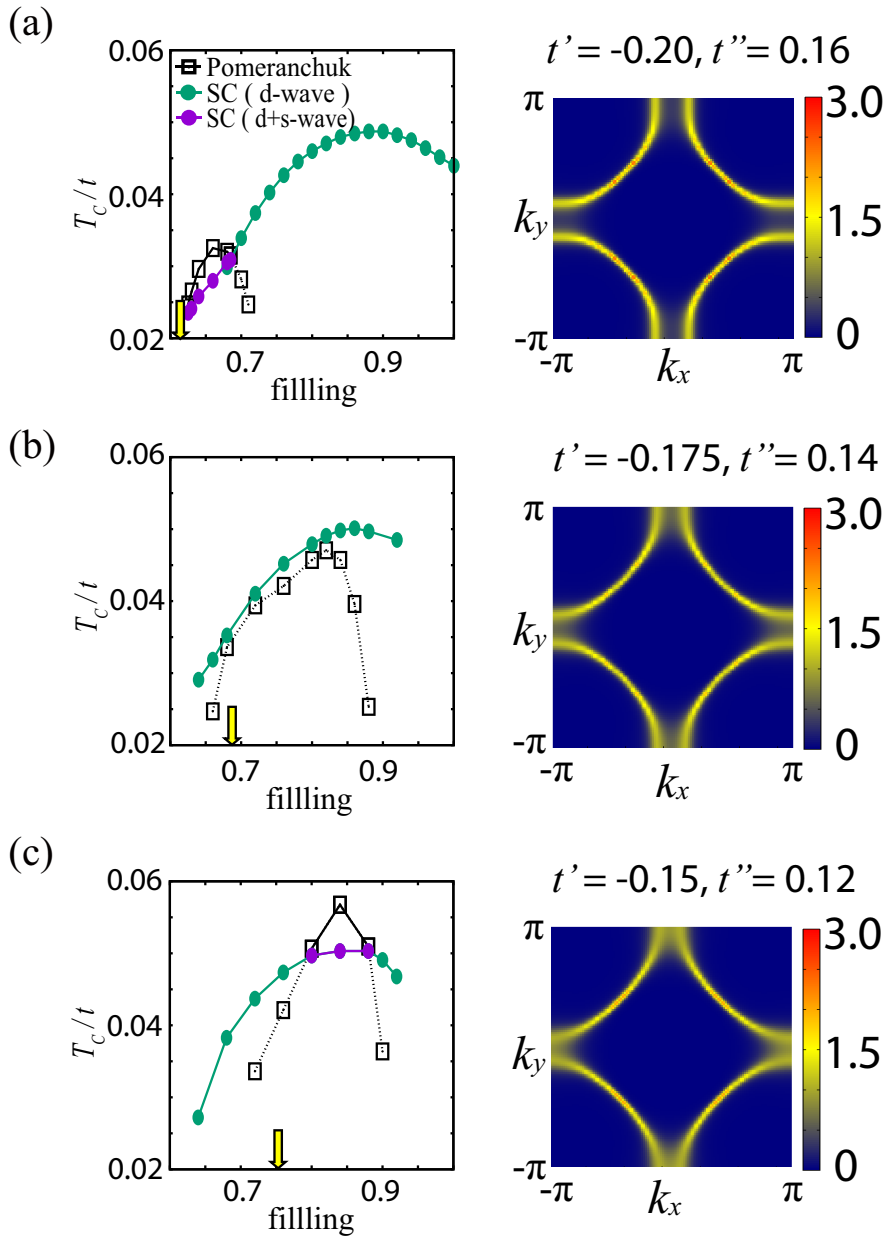

Figure 5.4: The superconducting and Pomeranchuk phase boundaries against filling for $U/t = 4.0$ (left panels), and the spectral weight $A(\boldsymbol{k}, \omega = 0)$ at $n_{\rm f} = 0.80, U/t = 4.0$ (right) are shown for $(t', t'') = (-0.20, 0.16)$ (a), $(-0.175, 0.14)$ (b), and $(-0.15, 0.12)$ (c) with $\beta t = 20$. The symbols are the same as in Fig. 5.3(a), while yellow arrows indicate respective van Hove fillings in the interacting system.

peaked near the van Hove filling. Therefore the present result indicates that the filling dependence of the effective interaction has an important effect of rendering the peak in the Pomeranchuk $T_c^{\rm PI}$ dome distinct from the peak in the superconducting $T_c^{\rm SC}$ dome against filling. To check this argument, we show in Fig. 5.4 the result when we systematically vary the second and further hoppings (t', t''), which change the Fermi surface warping as well as the van Hove filling. We can see that, for a fixed $n_{\rm f} = 0.80$, the change in the parameters shifts the distance of the filling from the van Hove filling as represented. Figure 5.4 plots three typical cases with different Fermi surface warping. Then we notice the position of the Pomeranchuk $T_c^{\rm PI}$ dome changes along with the van Hove filling (indicated by yellow arrows), while the superconducting $T_c^{\rm SC}$ is much less sensitive. Right panels in Fig. 5.4 plot the spectral weight at $n_{\rm f} = 0.80$. We can see that we are approaching to the van Hove filling as we go from (a) to (c) from the blurring of the spectral function around $(0, \pi), (\pi, 0)$. We can thus conclude that, despite both of superconductivity and the Pomeranchuk instabilities being Fermi surface instabilities that should be affected by the spectral weight at the Fermi energy, the Pomeranchuk instability is much more sensitive to the Fermi surface shape (distance from the van Hove filling) than $T_c^{\rm SC}$. Hence the present result suggests that we can separate the dominant regions for the two instabilities by changing the position against the van Hove filling (dominated by t', t'').

5.3 Superconductivity under Fermi surface distortions

Next, an important question is how superconductivity behaves in the presence of the Pomeranchuk Fermi surface distortion. Figure 5.5(a) shows the superconducting order parameter under the Pomeranchuk distortion, where the pairing symmetry is seen to be distorted from the ordinary d-wave to d+(extended)s-wave. There, an interesting observation is that the superconducting $T_c^{\rm SC}$ can be enhanced by the Pomeranchuk distortion as shown in Fig. 5.3, where we have also plotted the superconducting $T_c^{\rm SC}$ when the four-fold Fermi surface is artificially imposed below Pomeranchuk $T_c^{\rm PI}$(green dots). We can see that $T_c^{\rm SC}$ with the distorted Fermi surface (purple dots) is higher. To consider the origin of this enhancement, we go back to the pairing interaction to compare between the cases of Pomeranchuk-distorted and the four-fold-imposed Fermi surfaces. In Fig. 5.5(b), we show the difference in the pairing interaction $V_{\rm eff}$ between these two cases for $U/t = 4.0$, $n_{\rm f} = 0.66$ and $\beta t = 31$. The result indicates that the Pomeranchuk instability in fact distorts the pairing interaction, with a d-wave like anisotropy.

Then we can discuss the distortion effect on the superconducting $T_c^{\rm SC}$. We consider the perturbational effect for small distortions, based on a general linearized

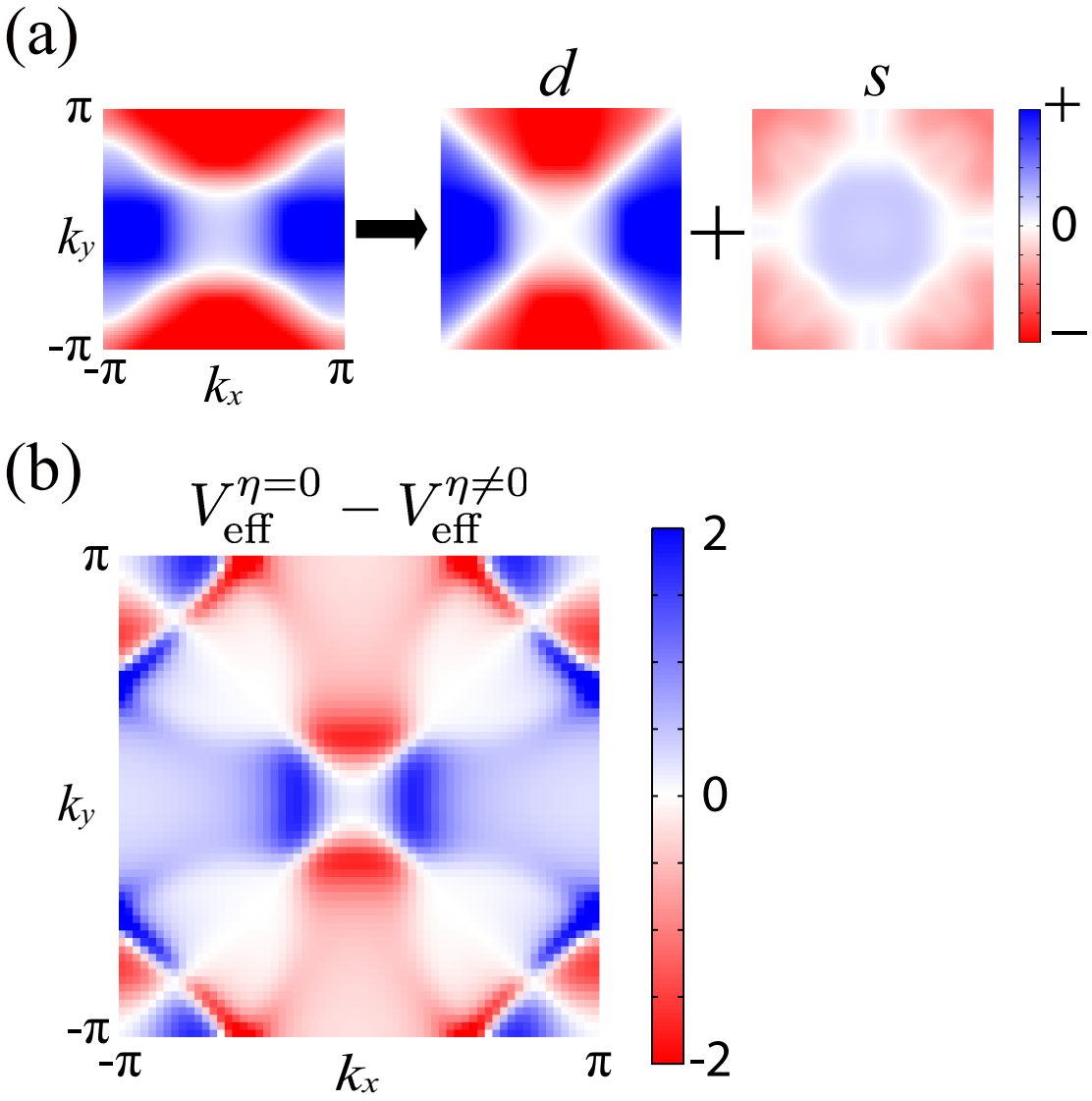

Figure 5.5: (a) Momentum dependence of the gap function for $T = 0.0286t < T_c^{\rm PI}$ with $n_{\rm f} = 0.66, U/t = 4.0, (t', t'') = (-0.20, 0.16)$ (left panel), which can be decomposed into a d-wave part and an (extended) s-wave (four-fold symmetric) part (right). (b) Difference in the pairing interaction with the Fermi surface distortion ($V_{\rm eff}^{\eta\neq 0}$) and without ($V_{\rm eff}^{\eta=0}$), for $\beta t = 31$ with the same $n_{\rm f}, U, t', t''$.

gap equation,

$$\lambda\phi(k) = -\frac{1}{N_{\boldsymbol{k}}\beta}\sum_{k'} K(k,k')\phi(k'), \tag{5.3}$$

where $\phi(k) = |G(k)|\Delta(k)$, while $K(k,k')$ is the kernel, given as $K(k,k') = |G(k)|V_{\rm eff}(k-k')|G(k')|$ in FLEX+DMFT (as seen by multiplying $|G|$ to both sides in Eq. (2.44)). If we consider small d-wave-like distortions for this kernel,

$$K(k,k') \to K(k,k') + \delta K^{\rm d}(k,k'), \tag{5.4}$$

the first-order perturbation for the maximum eigenvalue $\lambda_{\rm max}$ satisfies

$$\delta\lambda^{(1)}_{\rm max} = \sum_{k,k'} \phi^*_{\rm max}(k)\delta K^{\rm d}(k,k')\phi_{\rm max}(k') = 0, \tag{5.5}$$

where $\phi_{\rm max}$ is the eigenvector for $\lambda_{\rm max}$.

Since $\delta\lambda^{(1)}_{\rm max}$ identically vanishes due to the d-wave nature of the $\delta K^{\rm d}$, the leading term is the second-order one,

$$\delta\lambda^{(2)}_{\rm max} = \sum_{i,k,k'} \frac{|\phi^*_{\rm max}(k)\delta K^{\rm d}(k,k')\phi_i(k')|^2}{\lambda_{\rm max}-\lambda_i} > 0, \tag{5.6}$$

where i is the index for the eigenvalue λ_i and eigenvector ϕ_i of the kernel matrix K. Since this expression is positive-definite, we find that small d-wave deformations of the kernel in the linearized gap equation always enhance the superconducting $T_c^{\rm SC}$. This explains the $T_c^{\rm SC}$ enhancement in Fig. 5.3(a), and can provide a *new pathway* for enhancing superconducting $T_c^{\rm SC}$ in terms of Fermi surface distortion. However, it should be difficult to achieve purely d-wave like distortions for the kernel, and the terms having some other symmetries should in general arise even from purely d-wave distortions of the Fermi surface. We can elaborate this by introducing a parameter g_k which represents either (i) spontaneous distortion of the electronic states ($\delta g_k = G(k) - G_{\rm undistorted}(k)$) or (ii) small d-wave modulation of the Hamiltonian ($\delta\mathcal{H} = \sum_{\boldsymbol{k},\sigma}\delta g_k c^\dagger_{\boldsymbol{k},\sigma}c_{\boldsymbol{k},\sigma}$). Then we can expand the interaction kernel in g_k, which gives, up to the second order,

$$K(k,k') \to K(k,k') + \sum_p \frac{\delta K}{\delta g_p}\delta g_p + \frac{1}{2}\sum_{p,q}\frac{\delta^2 K}{\delta g_p \delta g_q}\delta g_p \delta g_q, \tag{5.7}$$

and the effect on the eigenvalue λ reads

$$\begin{aligned}\delta\lambda^{(2)}_{\rm max} = &\sum_{i,k,k'} \frac{|\phi^*_{\rm max}(k)\sum_p \frac{\delta K}{\delta g_p}\delta g_p \phi_{\rm i}(k')|^2}{\lambda_{\rm max}-\lambda_{\rm i}} \\ &- \sum_{k,k'}\phi^*(k)\frac{1}{2}\sum_{p,q}\frac{\delta^2 K}{\delta g_p\delta g_q}\delta g_p\delta g_q\phi(k').\end{aligned} \tag{5.8}$$

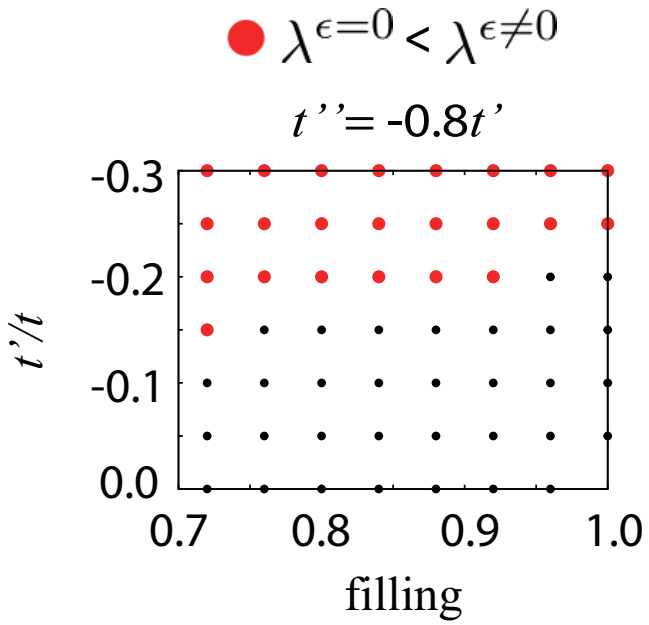

Figure 5.6: Comparison of the eigenvalue λ calculated within RPA between the four-fold symmetric Fermi surface ($\epsilon = 0$) and the distorted Fermi surface ($\epsilon = 0.01$) against the filling and t' with $t'' = -0.8t'$ (which includes the parameter set used in the Fig. 5.4). Red (black) dots representing the case of $\lambda^{\epsilon=0} < \lambda^{\epsilon=0.01}$ ($\lambda^{\epsilon=0} > \lambda^{\epsilon=0.01}$) for $\beta t = 5, U/t = 2.0$.

We can see that whether $T_c^{\rm SC}$ can be enhanced depends on the second term on the right-hand side of Eq. (5.8). From this we expect that the enhancement tends to occur when the second-largest eigenvalue is close to the largest one, for which the first term on the right-hand side of Eq. (5.8) becomes dominant.

We can actually check this argument in the weak-coupling case. To obtain qualitative tendencies, we have performed the RPA calculation at relatively high temperatures for various values of parameters where we make the nearest-neighbor hopping anisotropy by hand like

$$t_x = 1 + \epsilon, t_y = 1 - \epsilon. \tag{5.9}$$

Then the two-dimensional dispersion becomes

$$\epsilon(\boldsymbol{k}) = -2t_x \cos\, k_x - 2t_y \cos\, k_y - 4t' \cos k_x \cos k_y - 2t''(\cos 2k_x + \cos 2k_y) - \mu, \tag{5.10}$$

and we compare the four-fold symmetric case ($\epsilon = 0$) and the weakly distorted case ($\epsilon = 0.01$). In the RPA, we ignore the self-energy effect in the Eliashberg equation (2.44). In Fig. 5.6, we compare the eigenvalue λ of distorted ($\epsilon = 0.01$) and undistorted ($\epsilon = 0$) case for $U/t = 2.0, \beta t = 5$. We can see that there is indeed

a region (red circles) where the distortion enhances the eigenvalue ($\lambda^{\epsilon=0.01} > \lambda^{\epsilon=0}$). Thus we confirm that the small distortions can indeed enhance the superconductivity at least in the weak-coupling limit where we can ignore the self-energy effect. This enhancement occurs away from half-filling, and for larger values of second and third neighbor hoppings t', t'' (i.e., more frustrated cases). It has been known that the gap symmetry (for the leading eigenvalue) tends to be changed for higher doping or more frustrated cases [97]. The present result suggests that the $T_c^{\rm SC}$ enhancement arising from the distortion of the Fermi surface tends to occur around the boundary for different gap symmetries where the leading and subleading eigenvalues are close to each other. This is also consistent with the above result for the t' dependence in FLEX+DMFT (Fig. 5.4), where the enhancement of $T_c^{\rm SC}$ occurs for $(t', t'') = (-0.20, 0.16)$.

We also notice that the structure of Eq. (5.8) is similar to *the pseudo Jahn-Teller effect*, where a Jahn-Teller-like distortion occurs without degeneracies due to a second-order effect of the distortion [98]. In this context we can also recall a well-known property that, if the eigenvalues are degenerate (as in p-wave pairing in a tetragonal system where p_x-wave and p_y-wave are degenerate, so that we end up with $p + ip$ pairing), $T_c^{\rm SC}$ can be enhanced by a strain effect [99]. In this sense, the present result may also be viewed as a possibility for this kind of $T_c^{\rm SC}$ enhancement revealed even for the (non-degenerate) d-wave dominate regime in two-dimensional repulsive Hubbard model, where the distortion in the present case comes from a spontaneous symmetry breaking due to a many-body effect.

5.4 Effect of the DMFT vertex $\Gamma_{\rm DMFT}$

According to the formulation in section 4.1, we should consider the local anomalous self-energy $\Delta_{\rm loc}$ coming from the DMFT functional (see Eq. (4.21)). Then the linearized Eliashberg equation becomes

$$\lambda\Delta(k) = -\frac{1}{N_{\boldsymbol{k}}\beta}\sum_{k'}[V_{\rm eff}(k-k') + \Gamma_{\rm DMFT}(\omega_n, \omega_m)] \times |G(k')|^2\Delta(k'), \tag{5.11}$$

where $\Gamma_{\rm DMFT} = \delta\Delta_{\rm loc}/\delta F$ is the functional derivative of the local anomalous self-energy. While this term can be ignored for studying pure d-wave pairing as in section 4.2, here we examine its effect on the $d + s$ pairing. We consider this effect to be small, because the additional term is an extended s-wave (off-site) pairing rather than the ordinary s-wave, so that a cancellation should occur in the momentum summation. To check this, we can estimate a lower bound of the maximal eigenvalue when $\Gamma_{\rm DMFT}$ is considered without calculating $\Gamma_{\rm DMFT}$ directly. From the eigenvector $\Delta_{\rm max}$ of Eq. (2.44), we extract the part, Δ', of the

gap function that is not affected by $\Gamma_{\rm DMFT}$ as

$$\Delta'(k) = \Delta_{\rm max}(k) - \frac{\sum_{\boldsymbol{k}} |G(k)|^2 \Delta_{\rm max}(k)}{\sum_{\boldsymbol{k}} |G(k)|^2}. \tag{5.12}$$

Then a quantity,

$$\lambda' = -\frac{\sum_{k,k'} \Delta'^*(k)|G(k)|^2 V_{\rm eff}(k-k')|G(k')|^2 \Delta'(k')}{\sum_k \Delta'^*(k)|G(k)|^2 \Delta(k)}, \tag{5.13}$$

gives a lower bound for the maximal eigenvalue when $\Gamma_{\rm DMFT}$ is considered. We have actually confirmed that the difference between λ' and λ (without $\Gamma_{\rm DMFT}$) is very small, $(\lambda - \lambda')/\lambda < 0.01$. Thus we conclude that the effect of the DMFT vertex $\Gamma_{\rm DMFT}$ does not significantly change the the result for the $T_c^{\rm SC}$ enhancement.

Chapter 6

Dynamical vertex approximation (DΓA) for superconducting phases

本章については、5年以内に雑誌等で刊行予定のため、非公開。

Chapter 7

Conclusion and discussions

7.1 Summary of the thesis

In the present thesis, we have studied the superconductivity in the square-lattice Hubbard model, employing diagrammatic extensions of the dynamical mean-field theory. We briefly summarize the results obtained in this thesis.

- In chapter 4, we have formulated the FLEX+DMFT in terms of the Luttinger-Ward functional, where the self-consistent loops fix the double-counting terms uniquely. We have then applied the formalism to superconductivity in the Hubbard model on the square lattice. We have revealed that the method gives a superconducting T_c dome structure in the T_c-filling phase diagram, while the ordinary FLEX fails to reproduce the dome. We have traced back the physical origin of the T_c dome to a combined effect of the filling dependent self-energy reduction and the filling dependent pairing interaction. We have also shown a double-peak structure for a filling closer to the Mott transition is obtained in this formalism, which is difficult to obtain within small-size cluster algorithms.

- In chapter 5, we have studied the Pomeranchuk instability in the Hubbard model by employing the FLEX+DMFT method developed here. We find that the Pomeranchuk instability temperature is much more sensitive to the frustration (second and further neighbor hoppings) and hence the van Hove filling than the superconducting T_c. We have revealed that the superconductivity in the presence of the distortion of the Fermi surface has the gap function changing from d-wave to $(d + s)$-wave. Furthermore, we find that the Pomeranchuk Fermi-surface distortion can enhance the superconducting T_c in the overdoped regime. We have traced the physical origin from a perturbational picture for small distortions.

- In chapter 6, to further improve the method by incorporating nonlocal self-energy effects, we have newly formulated a dynamical vertex approximation for superconducting phases. The numerical result shows that we also obtain the dome structure of the leading eigenvalue of the Eliashberg equation, where the eigenvalue (a measure of T_c) is reduced. To examine this, we examined the vertex-correction effect on the pairing interaction, and found a strong screening effect around the Fermi level, which cannot be captured in the conventional one-boson exchange pictures. The frequency-dependent pairing interaction as revealed here may open a possibility of having an important effect on various kinds of pairing symmetries.

7.2 Future prospect

We can think of many future problems as follows:

1. In chapter 5, we have studied a charge instability, but we have assumed the translational invariance, i.e., we have only considered uniform instabilities. For considering charge instabilities with a finite wavenumber $\boldsymbol{q}$, one possible way is to assume an important interaction and study the divergence of the susceptibility, as in the Eliashberg equation for superconductivity.

2. As mentioned in chapter 4, our results are considered to represent the phase diagrams for the quasi-two-dimensional systems where the layers are weakly coupled as in real materials. On the other hand, purely two-dimensional superconductors can accommodate the Berezinskii-Kosterlitz-Thouless (BKT) transition [109] at finite temperatures, and the superconducting systems that can be regarded as purely two-dimensional are actually realized experimentally [110]. While a DCA study [111] discusses the BKT transition in the Hubbard model, they also mention that the results may possibly contain a very slow, logarithmic cluster-size dependence. From the present diagrammatic perspective, we expect to deal with the pure two-dimensionality if we can take account of the superconducting fluctuation effects, so that its implementation will be an important future problem. In particular, the full-parquet DΓA formalism should enable us to take account of all types of fluctuation effects on an equal footing.

3. Throughout the thesis, we have focused on the two-dimensional repulsive, single-orbital Hubbard model. Applying the methods developed in the present thesis to more complicated models, such as multi-orbital systems, offsite repulsions, etc, will also be an interesting future direction. For examining real materials, combination of these methods with the first-principle electronic structure calculations should also be necessary.

Appendix A

Relationship between the thermodynamic potential and Luttinger-Ward functional

The Luttinger-Ward functional Φ is defined as

$$\Phi[G] \equiv \frac{1}{\beta}\sum_{k}\sum_{n=1}^{\infty}\frac{1}{2n}G(k)\Sigma^{(n)}(k;[G]), \tag{A.1}$$

where $\Sigma^{(n)}(k;[G])$ is the nth-order diagram that is constructed from the renormalized Green's function G and interaction U. Then $\Phi[G]$ satisfies

$$\frac{\delta\Phi[G]}{\delta G(k)} = \sum_{n=1}^{\infty}\Sigma^{(n)}(k;[G]). \tag{A.2}$$

The thermodynamic potential Ω is defined as

$$\Omega \equiv -\frac{1}{\beta}\ln \mathrm{Tr} e^{-\beta\mathcal{H}}. \tag{A.3}$$

Considering a perturbation expansion of the thermodynamic potential Ω, we obtain

$$\Omega - \Omega_0 = \sum_{n=1}^{\infty}\Omega^{(n)}, \tag{A.4}$$

$$\Omega^{(n)} = \frac{1}{2n}\sum_{k}G_0(k)\Sigma^{(n)}(k;[G_0]), \tag{A.5}$$

where Ω_0 is the non-interacting thermodynamic potential and $\Sigma^{(n)}(k)$ is the nth-order diagram that is constructed from the non-interacting Green's function G_0 and U.

We note that

$$\sum_{n=1}^{\infty} \Sigma^{(n)}(k;[G]) = \Sigma(k), \tag{A.6}$$

while $\Sigma^{(n)}(k)$ contains one-particle reducible diagrams as

$$\begin{aligned}\sum_{n=1}^{\infty} \Sigma^{(n)}(k) &= \Sigma(k) + \Sigma(k)G_0(k)\Sigma(k) + \Sigma(k)G_0\Sigma(k)G_0\Sigma(k) + \cdots \\ &\neq \Sigma(k).\end{aligned} \tag{A.7}$$

We introduce a scaling parameter λ to consider the perturbation under the scaled interaction Hamiltonian $\lambda\mathcal{H}_I$. This means $G_0 \to G_0$ and $U \to \lambda U$ in the diagrams. We obtain

$$\begin{aligned}\frac{\delta\Omega}{\delta\lambda} &= \sum_{n=1}^{\infty} \frac{\delta\Omega^{(n)}}{\delta\lambda} \\ &= \frac{1}{2\lambda}\sum_k G_0(k)\left[\sum_{n=1}^{\infty}\Sigma^{(n)}(k)\right] \\ &= \frac{1}{2\lambda}\sum_k G_0(k)\left[\Sigma(k) + \Sigma(k)G_0(k)\Sigma(k) + \Sigma(k)G_0\Sigma(k)G_0\Sigma(k) + \cdots\right] \\ &= \frac{1}{2\lambda}\sum_k \Sigma(k)\left[G_0(k) + G_0(k)\Sigma(k)G_0(k) + G_0\Sigma(k)G_0\Sigma(k)G_0\Sigma(k)G_0 + \cdots\right] \\ &= \frac{1}{2\lambda}\sum_k G(k)\Sigma(k).\end{aligned} \tag{A.8}$$

On the other hand,

$$\begin{aligned}\frac{\delta\Phi[G]}{\delta\lambda} &= \frac{1}{2\lambda}\sum_k\sum_{n=1}^{\infty} G(k)\Sigma^{(n)}(k;[G]) + \sum_k \frac{\delta\Phi[G]}{\delta G(k)}\frac{\delta G(k)}{\delta\lambda} \\ &= \frac{1}{2\lambda}\sum_k G(k)\Sigma(k) + \sum_k \Sigma(k)\frac{\delta G(k)}{\delta\lambda},\end{aligned} \tag{A.9}$$

then

$$\begin{aligned}\frac{\delta}{\delta\lambda}(\Omega - \Phi[G]) &= -\sum_k [G_0(k)^{-1} - G(k)^{-1}]\frac{\delta G(k)}{\delta\lambda} \\ &= -\sum_k \left[\frac{\delta \ln(-G(k)^{-1})}{\delta\lambda} + G_0(k)^{-1}\frac{\delta G(k)}{\delta\lambda}\right].\end{aligned} \tag{A.10}$$

Integrating Eq.(A.10) from $\lambda = 0$ to $\lambda = 1$, we obtain

$$\begin{aligned}[\Omega - \Phi[G]]_{\lambda=0}^{\lambda=1} &= \Omega - \Phi[G] - \Omega_0, \\ &= -\sum_k \left\{ \ln[-G(k)^{-1}] - \ln[-G_0(k)^{-1}] + G_0(k)^{-1}[G(k) - G_0(k)] \right\}, \quad \text{(A.11)}\end{aligned}$$

then

$$\begin{aligned}\Omega &= \Phi[G] - \sum_k \left[\ln[-G(k)^{-1}] + \Sigma(k)G(k) \right], \\ &= \mathrm{Tr}\, \ln(-G) - \mathrm{Tr}(G\Sigma) + \Phi[G]. \quad \text{(A.12)}\end{aligned}$$

Appendix B

Atomic and high-frequency limits of the impurity model

We take the Anderson impurity model and compare the exact self-energy and the modified IPT self-energy in the high-frequency limit and the atomic limit. The Anderson impurity model Hamiltonian $\mathcal{H}_{\mathrm{AIM}}$ is expressed as

$$\mathcal{H}_{\mathrm{AIM}} = \sum_{\sigma}(\epsilon_d - \mu)c^{\dagger}_{d,\sigma}c_{d,\sigma} + Un_{d,\uparrow}n_{d,\downarrow} + \sum_{\boldsymbol{k},\sigma}(\epsilon_{\boldsymbol{k}} - \mu)c^{\dagger}_{\boldsymbol{k},\sigma}c_{\boldsymbol{k},\sigma} + \sum_{\boldsymbol{k},\sigma} V_{\boldsymbol{k}d}(c^{\dagger}_{d,\sigma}c_{\boldsymbol{k},\sigma} + c^{\dagger}_{\boldsymbol{k},\sigma}c_{d,\sigma}), \tag{B.1}$$

where $c^{\dagger}_{d,\sigma}$ and $c_{d,\sigma}$ are respectively the creation and annihilation operators at the impurity site, $c^{\dagger}_{\boldsymbol{k},\sigma}$ and $c_{\boldsymbol{k},\sigma}$ are respectively the creation and annihilation operators at a bath site, U is the strength of the interaction at the impurity site, μ is the chemical potential, and $V_{\boldsymbol{k},d}$ is the hybridization between the impurity site and bath sites.

The action for this Hamiltonian is the same as Eq. (3.5), and the Weiss field is obtained as

$$\mathcal{G}^{-1}(\omega_n) = i\omega_n - (\epsilon_d - \mu) - \Delta(\omega_n), \tag{B.2}$$

where Δ is called the hybridization function and defined as

$$\Delta(\omega_n) = \sum_{\boldsymbol{k}} \frac{V^2_{\boldsymbol{k}d}}{i\omega_n - \epsilon_{\boldsymbol{k}}}. \tag{B.3}$$

B.1 High-frequency limit of the second-order perturbation

The second-order perturbation self-energy $\Sigma^{(2)}$ is

$$\begin{aligned}
\Sigma^{(2)}(\omega_n) &= -U^2 \int_0^\beta d\tau e^{i\omega_n \tau} \bar{\mathcal{G}}(\tau)^2 \bar{\mathcal{G}}(-\tau) \\
&= -U^2 \left[\frac{e^{i\omega_n \tau}}{i\omega_n} \bar{\mathcal{G}}(\tau)^2 \bar{\mathcal{G}}(-\tau) \right]_0^\beta + O\left(\frac{1}{(i\omega_n)^2} \right) \\
&= \frac{-U^2}{i\omega_n} \left[-\bar{\mathcal{G}}(\beta)^2 \bar{\mathcal{G}}(-\beta) - \bar{\mathcal{G}}(+0)^2 \bar{\mathcal{G}}(-0) \right] + O\left(\frac{1}{(i\omega_n)^2} \right) \\
&= \frac{-U^2}{i\omega_n} \bar{\mathcal{G}}(0) \bar{\mathcal{G}}(\beta) (\bar{\mathcal{G}}(0) + \bar{\mathcal{G}}(\beta)) + O\left(\frac{1}{(i\omega_n)^2} \right), \qquad \text{(B.4)}
\end{aligned}$$

where $\bar{\mathcal{G}}$ is defined in Eq. (3.15). Then we consider a high-frequency expansion of $\bar{\mathcal{G}}(\omega_n)$ as

$$\begin{aligned}
\bar{\mathcal{G}}(\omega_n) &= \int_0^\beta d\tau e^{i\omega_n \tau} \bar{\mathcal{G}}(\tau) \\
&= \left[\frac{e^{i\omega_n \tau}}{i\omega_n} \bar{\mathcal{G}}(\tau) \right]_0^\beta + O\left(\frac{1}{(i\omega_n)^2} \right) \\
&= -\frac{\bar{\mathcal{G}}(0) + \bar{\mathcal{G}}(\beta)}{i\omega_n} + O\left(\frac{1}{(i\omega_n)^2} \right). \qquad \text{(B.5)}
\end{aligned}$$

From Eqs. (B.2) and (B.3), $\bar{\mathcal{G}}(\omega_n)$ becomes

$$\bar{\mathcal{G}}(\omega_n) \to \frac{1}{i\omega_n} \ (|\omega_n| \to \infty), \qquad \text{(B.6)}$$

in the high-frequency limit. Comparing Eqs. (B.5) and (B.6), we obtain

$$\bar{\mathcal{G}}(0) + \bar{\mathcal{G}}(\beta) = -1. \qquad \text{(B.7)}$$

If we define n_0 as

$$n_0 \equiv \frac{1}{\beta} \sum_{\omega_n} \bar{\mathcal{G}}(\omega_n) e^{-i\omega_n 0^-} = \bar{\mathcal{G}}(-0) = -\bar{\mathcal{G}}(\beta), \qquad \text{(B.8)}$$

then we obtain

$$\begin{aligned}
\bar{\mathcal{G}}(0) &= n_0 - 1, \qquad \text{(B.9)} \\
\bar{\mathcal{G}}(\beta) &= -n_0. \qquad \text{(B.10)}
\end{aligned}$$

We thus obtain the high-frequency limit of $\Sigma^{(2)}$ as

$$\Sigma^{(2)}(\omega_n) \to \frac{U^2 n_0 (1 - n_0)}{i\omega_n} \ (|\omega_n| \to \infty). \qquad \text{(B.11)}$$

B.2 Atomic limit of the second-order perturbation

In the atomic limit ($U >> V$), the Hamiltonian becomes

$$\mathcal{H}_{\rm AIM} \rightarrow \sum_{\sigma}(\epsilon_d - \mu)c^{\dagger}_{d,\sigma}c_{d,\sigma} + Un_{d,\uparrow}n_{d,\downarrow}, \tag{B.12}$$

in which the Weiss field becomes

$$\mathcal{G}^{-1}(\omega_n) = i\omega_n - (\epsilon_d - \mu), \tag{B.13}$$

and

$$\bar{\mathcal{G}}^{-1}(\omega_n) = i\omega_n - (\epsilon_d - \mu) - U\delta n - U/2. \tag{B.14}$$

If we define $x \equiv \epsilon_d - \mu + U\delta n + U/2$, $\bar{\mathcal{G}}(\tau)$ is obtained as

$$\begin{aligned} \bar{\mathcal{G}}(\tau) &= \frac{1}{\beta}\sum_{\omega_n}\frac{e^{-i\omega_n\tau}}{i\omega_n - x} \\ &= -f(-x)e^{-x\tau}, \end{aligned} \tag{B.15}$$

where $f(x)$ is the Fermi distribution function.

Then the second-order perturbation self-energy is obtained as

$$\begin{aligned} \Sigma^{(2)}(\omega_n) &= U^2\int_0^{\beta} d\tau \bar{\mathcal{G}}(\tau)^2\bar{\mathcal{G}}(\beta-\tau)e^{i\omega_n\tau} \\ &= -U^2\int_0^{\beta} d\tau f^3(-x)e^{(i\omega_n - x)\tau}e^{-\beta x} \\ &= U^2 f^3(-x)\frac{e^{-\beta x}(e^{-\beta x}+1)}{i\omega_n - x} \\ &= \frac{U^2 f(x)(1-f(x))}{i\omega_n - x}. \end{aligned} \tag{B.16}$$

From Eq. (B.15),

$$\bar{\mathcal{G}}(\beta) = -f(-x)e^{-x\beta}, \tag{B.17}$$

and

$$\begin{aligned} f(x) &= e^{-\beta x}f(-x) \\ &= -\bar{\mathcal{G}}(\beta) \\ &= n_0, \end{aligned} \tag{B.18}$$

then we obtain the second-order perturbation self-energy $\Sigma^{(2)}$ in the atomic limit as

$$\Sigma^{(2)}(\omega_n) \rightarrow \frac{U^2 n_0(1-n_0)}{i\omega_n - (\epsilon_d - \mu) - U\delta n - U/2}. \tag{B.19}$$

B.3 High-frequency limit of the exact self-energy of the impurity model

In the high-frequency limit, the Green's function can be expanded as

$$
\begin{aligned}
&G_{\rm imp}(\omega_n) = \int_0^\beta d\tau e^{i\omega_n\tau} G_{\rm imp}(\tau) \\
&= \left[\frac{e^{i\omega_n\tau}}{i\omega_n} G_{\rm imp}(\tau)\right]_0^\beta - \left[\frac{e^{i\omega_n\tau}}{(i\omega_n)^2} G'_{\rm imp}(\tau)\right]_0^\beta + \left[\frac{e^{i\omega_n\tau}}{(i\omega_n)^3} G''_{\rm imp}(\tau)\right]_0^\beta - \cdots \\
&= -\frac{G_{\rm imp}(+0) - G_{\rm imp}(-0)}{i\omega_n} + \frac{G'_{\rm imp}(+0) - G'_{\rm imp}(-0)}{(i\omega_n)^2} - \frac{G''_{\rm imp}(+0) - G''_{\rm imp}(-0)}{(i\omega_n)^3} + \cdots ,
\end{aligned}
\tag{B.20}
$$

From the Heisenberg equation of motion, we obtain

$$
\begin{aligned}
G_{\rm imp}(\tau) &= -\left\langle T_\tau c_{{\rm d},\sigma}(\tau) c^\dagger_{{\rm d},\sigma}(0)\right\rangle , \\
\frac{d}{d\tau} G_{\rm imp}(\tau) &= -\left\langle T_\tau [\mathcal{H}_{\rm AIM}, c_{{\rm d},\sigma}(\tau)] c^\dagger_{{\rm d},\sigma}(0)\right\rangle , \\
\frac{d^2}{d^2\tau} G_{\rm imp}(\tau) &= -\left\langle T_\tau [\mathcal{H}_{\rm AIM}, [\mathcal{H}_{\rm AIM}, c_{{\rm d},\sigma}(\tau)]] c^\dagger_{{\rm d},\sigma}(0)\right\rangle .
\end{aligned}
\tag{B.21}
$$

Then we obtain

$$
\begin{aligned}
&G_{\rm imp}(\omega_n) \\
&= \frac{\left\langle \left\{ c_{{\rm d},\sigma}, c^\dagger_{{\rm d},\sigma} \right\} \right\rangle}{i\omega_n} - \frac{\left\langle \left\{ [\mathcal{H}_{\rm AIM}, c_{{\rm d},\sigma}], c^\dagger_{{\rm d},\sigma} \right\} \right\rangle}{(i\omega_n)^2} + \frac{\left\langle \left\{ [\mathcal{H}_{\rm AIM}, [\mathcal{H}_{\rm AIM}, c_{{\rm d},\sigma}]], c^\dagger_{{\rm d},\sigma} \right\} \right\rangle}{(i\omega_n)^3} - \cdots ,
\end{aligned}
\tag{B.22}
$$

where $\{\ ,\ \}$ is an anti-commutator. We calculate the commutation relation as

$$
[\mathcal{H}_{\rm AIM}, c_{d,\sigma}] = -(\epsilon_d - \mu) c_{d,\sigma} - U n_{d,-\sigma} c_{d,\sigma} - \sum_{\boldsymbol{k}} V_{\boldsymbol{k}d} c_{\boldsymbol{k},\sigma},
\tag{B.23}
$$

$$
\begin{aligned}
&[\mathcal{H}_{\rm AIM}, [\mathcal{H}_{\rm AIM}, c_{i,\sigma}]] \\
&= (\epsilon_d - \mu + U n_{d,-\sigma})^2 c_{d,\sigma} + \sum_{\boldsymbol{k}} V^2_{\boldsymbol{k}d} c_{d,\sigma} + \sum_{\boldsymbol{k}} V_{\boldsymbol{k}d} (\epsilon_d - \epsilon_{\boldsymbol{k}} + n_{d,-\sigma}) c_{\boldsymbol{k},\sigma}.
\end{aligned}
\tag{B.24}
$$

Then

$$
\{[\mathcal{H}_{\rm AIM}, c_{d,\sigma}], c^\dagger_{d,\sigma}\} = -(\epsilon_d - \mu) - U n_{d,-\sigma},
\tag{B.25}
$$

$$\{[\mathcal{H}_{\rm AIM},[\mathcal{H}_{\rm AIM},c_{d,\sigma}]],c^\dagger_{d,\sigma}\}$$
$$=(\epsilon_d-\mu)^2+2U(\epsilon_d-\mu)n_{d,-\sigma}+U^2n_{d,-\sigma}+\sum_{\boldsymbol{k}}V^2_{\boldsymbol{k}d}, \tag{B.26}$$

and we obtain the high-frequency expansion of the Green's function of the impurity problem as

$$G_{\rm imp}(\omega_n)$$
$$=\frac{1}{i\omega_n}+\frac{(\epsilon_d-\mu)+Un}{(i\omega_n)^2}+\frac{(\epsilon_d-\mu)^2+2Un(\epsilon_d-\mu)+U^2n+\sum_{\boldsymbol{k}}V^2_{\boldsymbol{k}d}}{(i\omega_n)^3}+\cdots, \tag{B.27}$$

where n is the density ($n=n_{d,\uparrow}=n_{d,\downarrow}$).

The high-frequency expansion of $\mathcal{G}^{-1}$ is

$$\mathcal{G}^{-1}=i\omega_n-(\epsilon_d-\mu)-\frac{\sum_{\boldsymbol{k}}V^2_{\boldsymbol{k}d}}{i\omega_n}+O\left(\frac{1}{(i\omega_n)^2}\right), \tag{B.28}$$

and the high-frequency expansion of $G^{-1}_{\rm imp}$ is

$$G^{-1}_{\rm imp}$$
$$=i\omega_n\left[1+\frac{(\epsilon_d-\mu)+Un}{i\omega_n}+\frac{(\epsilon_d-\mu)^2+2Un(\epsilon_d-\mu)+U^2n+\sum_{\boldsymbol{k}}V^2_{\boldsymbol{k}d}}{(i\omega_n)^2}+\cdots\right]^{-1}$$
$$=i\omega_n-(\epsilon_d-\mu)-Un-\frac{U^2n(1-n)+\sum_{\boldsymbol{k}}V^2_{\boldsymbol{k}d}}{i\omega_n}+O\left(\frac{1}{(i\omega_n)^2}\right). \tag{B.29}$$

Then the self-energy of the impurity problem becomes

$$\begin{aligned}\Sigma_{\rm imp}(\omega_n) &= \mathcal{G}^{-1}(\omega_n)-G^{-1}_{\rm imp}(\omega_n)\\ &= Un+\frac{U^2n(1-n)}{i\omega_n}+O\left(\frac{1}{(i\omega_n)^2}\right),\end{aligned} \tag{B.30}$$

and we obtain the high-frequency limit of the self-energy of the impurity problem $\Sigma_{\rm imp}$ as

$$\Sigma_{\rm imp}(\omega_n)=\Sigma_{\rm H}+\frac{U^2n(1-n)}{i\omega_n}+O\left(\frac{1}{(i\omega_n)^2}\right). \tag{B.31}$$

B.4 Atomic limit of the exact self-energy of the impurity model

In the atomic limit, we take a one-site problem as

$$\mathcal{H}=\sum_\sigma(\epsilon_d-\mu)c^\dagger_{d,\sigma}c_{d,\sigma}+Un_{d,\uparrow}n_{d,\downarrow}. \tag{B.32}$$

This model is exactly solvable, for the eigenstate

$$
\begin{aligned}
\mid 0\rangle &= \mid vac\rangle, && \text{(B.33)}\\
\mid 1,\uparrow\rangle &= c^{\dagger}_{d,\uparrow} \mid \text{vac}\rangle, && \text{(B.34)}\\
\mid 1,\downarrow\rangle &= c^{\dagger}_{d,\downarrow} \mid \text{vac}\rangle, && \text{(B.35)}\\
\mid 2\rangle &= c^{\dagger}_{d,\uparrow} c^{\dagger}_{d,\downarrow} \mid \text{vac}\rangle, && \text{(B.36)}
\end{aligned}
$$

with respective eigenvalues

$$
\begin{aligned}
E_0 &= 0, && \text{(B.37)}\\
E_{1,\uparrow} = E_{1,\downarrow} &= \epsilon_d - \mu, && \text{(B.38)}\\
E_2 &= 2(\epsilon_d - \mu) + U. && \text{(B.39)}
\end{aligned}
$$

We then obtain the exact Green's function as

$$
\begin{aligned}
G_{\text{loc}}(\tau) &= -\left\langle T_\tau c_{d,\sigma}(\tau) c^{\dagger}_{d,\sigma}(0) \right\rangle \\
&= \frac{1}{Z} \sum_{m,l} -\theta(\tau) e^{-\beta E_m} \langle m \mid e^{\mathcal{H}\tau} c_{d,\sigma} e^{-\mathcal{H}\tau} \mid l\rangle\langle l \mid c^{\dagger}_{d,\sigma} \mid m\rangle \\
&\qquad +\theta(-\tau) e^{-\beta E_m} \langle m \mid c^{\dagger}_{d,\sigma} \mid l\rangle\langle l \mid e^{\mathcal{H}\tau} c_{d,\sigma} e^{-\mathcal{H}\tau} \mid m\rangle \\
&= -\frac{\theta(\tau)}{Z} \left[e^{-\beta E_0} e^{(E_0 - E_1)\tau} + e^{-\beta E_1} e^{(E_1 - E_2)\tau} \right] \\
&\qquad +\frac{\theta(-\tau)}{Z} \left[e^{-\beta E_1} e^{(E_0 - E_1)\tau} + e^{-\beta E_2} e^{(E_1 - E_2)\tau} \right], \qquad \text{(B.40)}
\end{aligned}
$$

where $m, l = 0, 1\uparrow, 1\downarrow, 2$, $E_1 = E_{1,\uparrow} = E_{1,\downarrow}$, $\theta(\tau)$ is the step function and Z is the partition function defined as

$$
Z = e^{-\beta E_0} + 2e^{-\beta E_1} + e^{-\beta E_2}. \qquad \text{(B.41)}
$$

Then we have

$$
\begin{aligned}
&G_{\text{loc}}(\omega_n) \\
&= \frac{e^{-\beta E_0} + e^{-\beta E_1}}{Z} \frac{1}{i\omega_n + E_0 - E_1} + \frac{e^{-\beta E_1} + e^{-\beta E_2}}{Z} \frac{1}{i\omega_n + E_1 - E_2}. \qquad \text{(B.42)}
\end{aligned}
$$

The density $n = n_\uparrow = n_\downarrow$ is

$$
n = \frac{e^{-\beta E_1} + e^{-\beta E_2}}{Z}. \qquad \text{(B.43)}
$$

Then we obtain the Green's function in the atomic limit as

$$
\begin{aligned}
G_{\text{loc}}(\omega_n) &= \frac{1 - n}{i\omega_n - (\epsilon_d - \mu)} + \frac{n}{i\omega_n - (\epsilon_d - \mu) - U} \\
&= \frac{1}{i\omega_n - (\epsilon_d - \mu) - \frac{Un(i\omega_n - (\epsilon_d - \mu))}{i\omega_n - (\epsilon_d - \mu) - U(1-n)}}. \qquad \text{(B.44)}
\end{aligned}
$$

Finally, we obtain the self-energy of the atomic limit as

$$\begin{aligned}\Sigma(\omega_n) &= \frac{Un(i\omega_n - (\epsilon_d - \mu))}{i\omega_n - (\epsilon_d - \mu) - U(1-n)} \\ &= \Sigma_{\mathrm{H}} + \frac{U^2 n(1-n)}{i\omega_n - (\epsilon_d - \mu) - U(1-n)}. \end{aligned} \tag{B.45}$$

Appendix C

Lehmann representation for the two-particle quantity

From Eq. (3.33), we need the Lehmann representation of $\bar{\chi}_{\mathrm{loc},\sigma\sigma'}$ defined as

$$\bar{\chi}_{\mathrm{loc},\sigma\sigma'}(\omega_n,\omega_{n'},\omega_m) \equiv \frac{1}{\beta^2}\int_0^\beta d\tau_1 d\tau_2 d\tau_3 e^{-i\tau_1\omega_n} e^{i\tau_2(\omega_n+\omega_m)} e^{-i\tau_3(\omega_{n'}+\omega_m)} \times \left\langle T_\tau c^\dagger_{i\sigma}(\tau_1) c_{i\sigma}(\tau_2) c^\dagger_{i\sigma'}(\tau_3) c_{i\sigma'}(0)\right\rangle . \tag{C.1}$$

Considering the arrangement of the time order, we can decompose $\bar{\chi}$ into six different terms as

$$\bar{\chi}_{\mathrm{loc},\sigma\sigma'}(\omega_n,\omega_{n'},\omega_m) = \frac{1}{\beta^2 Z}(\chi^{123}_{\sigma\sigma'} + \chi^{132}_{\sigma\sigma'} + \chi^{312}_{\sigma\sigma'} + \chi^{213}_{\sigma\sigma'} + \chi^{231}_{\sigma\sigma'} + \chi^{321}_{\sigma\sigma'}), \tag{C.2}$$

where $\chi^{123}_{\sigma\sigma'}$ is

$$\begin{aligned}
\chi^{123}_{\sigma\sigma'} \equiv & \int_0^\beta d\tau_1 \int_0^{\tau_1} d\tau_2 \int_0^{\tau_2} d\tau_3 e^{-i\tau_1\omega_n} e^{i\tau_2(\omega_n+\omega_m)} e^{-i\tau_3(\omega_{n'}+\omega_m)} \\
& \times \sum_i \langle i \mid c^\dagger_{i\sigma}(\tau_1) c_{i\sigma}(\tau_2) c^\dagger_{i\sigma'}(\tau_3) c_{i\sigma'}(0) \mid i\rangle e^{-\beta E_i} \\
= & \sum_{i,j,k,l} \langle i \mid c^\dagger \mid j\rangle\langle j \mid c \mid k\rangle\langle k \mid c^\dagger \mid l\rangle\langle l \mid c \mid i\rangle e^{-\beta E_i} \\
& \times \int_0^\beta d\tau_1 e^{[E_i - E_j - i\omega_n]\tau_1} \int_0^{\tau_1} d\tau_2 e^{[E_j - E_k + i(\omega_n+\omega_m)]\tau_2} \int_0^{\tau_3} d\tau_3 e^{[E_k - E_l - i(\omega_{n'}+\omega_m)]\tau_3} \\
= & \sum_{i,j,k,l} \frac{-1}{i(\omega_{n'}+\omega_m) - E_k + E_l} \\
& \times \left[\frac{1}{i(\omega_n - \omega_{n'}) + E_j - E_l} \left(\frac{e^{-\beta E_i} + e^{-\beta E_l}}{i\omega_{n'} - E_i + E_l} - \frac{e^{-\beta E_j} + e^{-\beta E_i}}{i\omega_n - E_i + E_j} \right) \right. \\
& \left. - \frac{1}{i(\omega_n + \omega_m) + E_j - E_k} \left(\frac{e^{-\beta E_k} - e^{-\beta E_i}}{i\omega_m + E_i - E_k} - \frac{e^{-\beta E_j} + e^{-\beta E_i}}{i\omega_n - E_i + E_j} \right) \right] \\
& \times \langle i \mid c^\dagger_\sigma \mid j\rangle\langle j \mid c_\sigma \mid k\rangle\langle k \mid c^\dagger_{\sigma'} \mid l\rangle\langle l \mid c_{\sigma'} \mid i\rangle. \qquad \text{(C.3)}
\end{aligned}$$

Similarly, $\chi^{132}_{\sigma\sigma'}, \ldots$ are computed as follows:

$$\begin{aligned}
\chi^{132}_{\sigma\sigma'} = & \sum_{i,j,k,l} \frac{1}{i(\omega_{n'}+\omega_m) - E_j + E_k} \\
& \times \left[\frac{1}{i(\omega_n + \omega_m) + E_k - E_l} \left(\frac{e^{-\beta E_i} + e^{-\beta E_l}}{i\omega_{n'} - E_i + E_l} - \frac{e^{-\beta E_i} - e^{-\beta E_k}}{i(\omega_n + \omega_{n'} + \omega_m) - E_i + E_k} \right) \right. \\
& \left. + \frac{1}{i(\omega_n - \omega_{n'}) + E_j - E_l} \left(\frac{e^{-\beta E_j} + e^{-\beta E_i}}{i\omega_n + E_j - E_i} - \frac{e^{-\beta E_l} + e^{-\beta E_i}}{i\omega_{n'} - E_i + E_l} \right) \right] \\
& \times \langle i \mid c^\dagger_\sigma \mid j\rangle\langle j \mid c^\dagger_{\sigma'} \mid k\rangle\langle k \mid c_\sigma \mid l\rangle\langle l \mid c_{\sigma'} \mid i\rangle, \qquad \text{(C.4)}
\end{aligned}$$

$$\begin{aligned}
\chi^{213}_{\sigma\sigma'} = & \sum_{i,j,k,l} \frac{1}{i(\omega_{n'}+\omega_m) + E_k - E_j} \\
& \times \left[\frac{1}{i(\omega_n + \omega_m) + E_l - E_i} \left(\frac{e^{-\beta E_j} - e^{-\beta E_l}}{i\omega_m + E_l - E_j} + \frac{e^{-\beta E_k} - e^{-\beta E_i}}{i(\omega_n + \omega_{n'} + \omega_m) - E_i + E_k} \right. \right. \\
& \left. \left. + \frac{e^{-\beta E_j} + e^{-\beta E_i}}{i\omega_n + E_j - E_i} - \frac{e^{-\beta E_l} + e^{-\beta E_k}}{i\omega_{n'} + E_k - E_l} \right) \right] \\
& \times \langle i \mid c^\dagger_\sigma \mid j\rangle\langle j \mid c^\dagger_{\sigma'} \mid k\rangle\langle k \mid c_{\sigma'} \mid l\rangle\langle l \mid c_\sigma \mid i\rangle, \qquad \text{(C.5)}
\end{aligned}$$

$$\chi^{231}_{\sigma\sigma'} = \sum_{i,j,k,l} \frac{-1}{i(\omega_{n'}+\omega_m)+E_j-E_i}$$
$$\times \left[\frac{1}{i(\omega_n-\omega_{n'})-E_j+E_l} \left(\frac{e^{-\beta E_j}+e^{-\beta E_k}}{i\omega_n+E_k-E_j} - \frac{e^{-\beta E_k}+e^{-\beta E_l}}{i\omega_{n'}-E_l+E_k} \right) \right.$$
$$\left. - \frac{1}{i(\omega_n+\omega_m)+E_l-E_i} \left(\frac{e^{-\beta E_k}-e^{-\beta E_i}}{i(\omega_n+\omega_{n'}+\omega_m)-E_i+E_k} - \frac{e^{-\beta E_k}+e^{-\beta E_l}}{i\omega_{n'}+E_k-E_l} \right) \right]$$
$$\times \langle i \mid c^\dagger_{\sigma'} \mid j\rangle\langle j \mid c^\dagger_\sigma \mid k\rangle\langle k \mid c_{\sigma'} \mid l\rangle\langle l \mid c_\sigma \mid i\rangle, \tag{C.6}$$

$$\chi^{312}_{\sigma\sigma'} = \sum_{i,j,k,l} \frac{-1}{i(\omega_{n'}+\omega_m)+E_j-E_i}$$
$$\times \left[\frac{1}{i(\omega_n+\omega_m)+E_k-E_l} \left(\frac{e^{-\beta E_j}-e^{-\beta E_l}}{i\omega_m+E_j-E_l} + \frac{e^{-\beta E_k}+e^{-\beta E_j}}{i\omega_n+E_k-E_j} \right.\right.$$
$$\left.\left. - \frac{e^{-\beta E_i}+e^{-\beta E_l}}{i\omega_{n'}+E_l-E_i} + \frac{e^{-\beta E_i}-e^{-\beta E_k}}{i(\omega_n+\omega_{n'}+\omega_m)+E_k-E_i} \right) \right]$$
$$\times \langle i \mid c^\dagger_{\sigma'} \mid j\rangle\langle j \mid c^\dagger_\sigma \mid k\rangle\langle k \mid c_\sigma \mid l\rangle\langle l \mid c_{\sigma'} \mid i\rangle, \tag{C.7}$$

$$\chi^{321}_{\sigma\sigma'} = \sum_{i,j,k,l} \frac{1}{i(\omega_{n'}+\omega_m)+E_j-E_i}$$
$$\times \left[\frac{1}{i(\omega_n+\omega_m)+E_j-E_k} \left(\frac{e^{-\beta E_l}+e^{-\beta E_k}}{i\omega_n+E_l-E_k} + \frac{e^{-\beta E_l}-e^{-\beta E_j}}{i\omega_m+E_j-E_l} \right) \right.$$
$$\left. - \frac{1}{i(\omega_n-\omega_{n'})+E_i-E_k} \left(\frac{e^{-\beta E_l}+e^{-\beta E_k}}{i\omega_n+E_l-E_k} - \frac{e^{-\beta E_l}+e^{-\beta E_i}}{i\omega_{n'}+E_l-E_i} \right) \right]$$
$$\times \langle i \mid c^\dagger_{\sigma'} \mid j\rangle\langle j \mid c_\sigma \mid k\rangle\langle k \mid c^\dagger_\sigma \mid l\rangle\langle l \mid c_{\sigma'} \mid i\rangle. \tag{C.8}$$

Appendix D

Padé approximation

In this appendix, we explain the formulation of the Padé approximation [112], which is a typical method of numerical analytical continuation. In this thesis, this method is used to obtain spectral function from the Matsubara Green's function. Then problem is, when the value of the Green's function on the imaginary axis is known as

$$G_n^{\text{input}} = G(i\omega_n), \tag{D.1}$$

how to obtain the Green's function on the real axis. In the Padé approximation, we assume that the Green's function can be expressed as

$$G(\omega) \approx G_N^{\text{pade}}(\omega) = \cfrac{a_1}{1 + \cfrac{a_2(\omega-\omega_1)}{1+\cfrac{a_3(\omega-\omega_2)}{\cdots 1+\cfrac{a_N(\omega-\omega_{N-1})}{1}}}}, \tag{D.2}$$

where $\{a_i\}$ are the fitting parameters. The parameters $\{a_i\}$ are determined such that the approximate function Eq. (D.2) satisfy Eq. (D.1).

We first define $\{f_N(\omega_n)\}$ recursively as

$$f_1(\omega_n) = G_n^{\text{input}}, \tag{D.3}$$

$$f_N(\omega_n) = \frac{f_{N-1}(\omega_{N-1}) - f_{N-1}(\omega_n)}{(i\omega_n - i\omega_{N-1})f_{N-1}(\omega_n)},\ (N > 1), \tag{D.4}$$

then a_N is determined through

$$a_N = f_N(\omega_N) \tag{D.5}$$

in order to satisfy Eq. (D.1) as

$$\begin{aligned} G_N^{\text{input}} &= f_1(\omega_N) \\ &= \frac{a_1}{1+\frac{\omega_N-\omega_1}{1}} f_2(\omega_N) \\ &= \frac{a_1}{1+\frac{a_2(\omega_N-\omega_1)}{1+\frac{(\omega_N-\omega_2)}{1}}} f_3(\omega_N) \\ &= \frac{a_1}{1+\frac{a_2(\omega_N-\omega_1)}{1+\frac{a_3(\omega_N-\omega_2)}{\cdots 1+\frac{a_N(\omega_N-\omega_{N-1})}{1}}}} \\ &= G^{\text{pade}}(i\omega_N). \end{aligned} \tag{D.6}$$

After determining the parameters $\{a_N\}$, we calculate $G(\omega)$ on real axis from Eq. (D.2). There is a useful algorithm: first we define P_N and Q_N recursively as

$$P_0 = 0,\ Q_0 = 1, \tag{D.7}$$

$$P_1 = a_1,\ Q_1 = 1, \tag{D.8}$$

$$P_{N+1}(\omega) = P_N(\omega) + a_{N+1}(\omega - i\omega_N)P_{N-1}(\omega), \tag{D.9}$$

$$Q_{N+1}(\omega) = Q_N(\omega) + a_{N+1}(\omega - i\omega_N)Q_{N-1}(\omega), \tag{D.10}$$

then the Green's function can be computed through

$$G_N^{\text{pade}}(\omega) = \frac{P_N(\omega)}{Q_N(\omega)}. \tag{D.11}$$

In each loop, we replace P and Q as

$$P_{N+1} \leftarrow \frac{P_{N+1}}{Q_{N+1}},\ P_N \leftarrow \frac{P_N}{Q_{N+1}}, \tag{D.12}$$

$$Q_{N+1} \leftarrow \frac{Q_{N+1}}{Q_{N+1}},\ Q_N \leftarrow \frac{Q_N}{Q_{N+1}}, \tag{D.13}$$

in order to avoid overflow and underflow of P and Q.

D.1 Derivation of Eq. (D.11)

For $N = 1, 2$,

$$G_1^{\text{pade}} = a_1 = \frac{P_1(\omega)}{Q_1(\omega)}, \tag{D.14}$$

$$G_2^{\text{pade}} = \frac{a_1}{1 + a_2(\omega - \omega_1)} = \frac{P_2(\omega)}{Q_2(\omega)}. \tag{D.15}$$

Also, if

$$G^{\text{pade}}_{N+1}(\omega) = \frac{P_{N+1}(\omega)}{Q_{N+1}(\omega)} = \frac{P_N(\omega) + a_{N+1}(\omega - \omega_N)P_{N-1}(\omega)}{Q_N(\omega) + a_{N+1}(\omega - \omega_N)Q_{N-1}(\omega)}, \tag{D.16}$$

then

$$\begin{aligned} G^{\text{pade}}_{N+2}(\omega) &= \frac{P_N(\omega) + \frac{a_{N+1}(\omega-\omega_N)}{1+a_{N+2}(\omega-\omega_{N+1})}P_{N-1}(\omega)}{Q_N(\omega) + \frac{a_{N+1}(\omega-\omega_N)}{1+a_{N+2}(\omega-\omega_{N+1})}Q_{N-1}(\omega)} \\ &= \frac{P_{N+1}(\omega) + a_{N+2}(\omega - \omega_{N+1})P_N(\omega)}{Q_{N+1}(\omega) + a_{N+2}(\omega - \omega_{N+1})Q_N(\omega)} \\ &= \frac{P_{N+2}(\omega)}{Q_{N+2}(\omega)}. \end{aligned} \tag{D.17}$$

Therefore Eq. (D.11) is satisfied for all N.

Bibliography

[1] L. D. Landau, Sov. Phys. JETP **3**, 920 (1957).

[2] J. H. de Boer and E. J. W. Verway, Proc. Phys. Soc. London, Sect A **49**, 59 (1937).

[3] N. F. Mott and R. Peierls, Proc. Phys. Soc. London, Sect A **49**, 72 (1937).

[4] H. Kamerlingh-Onnes, Leiden Comm. **120b, 122b, 124c** (1911).

[5] W. Meissner and R. Ochsenfeld, Naturwissenshaften **21**, 787 (1933).

[6] J. Bardeen, L. N. Cooper, and J. R. Schrieffer, Phys. Rev. **108**, 1175 (1957).

[7] J. G. Bednorz and K. A. Muller, Z. Phys. B **64**, 189 (1986).

[8] M. K. Wu, J. R. Ashburn, C. J. Torng, P. H. Hor, R. L. Meng, L. Gao, Z. J. Huang, Y. Q. Wang, and C. W. Chu, Phys. Rev. Lett. **58**, 908 (1987).

[9] S. N. Putilin, E. V. Antipov, O. Chmaissem, and M. Marezio, Nature **362**, 226 (1993).

[10] Y. Tokura, H. Takagi, and S. Uchida, Nature **337**, 345 (1989).

[11] N. P. Armitage, P. Fournier, and R. L. Greene, Rev. Mod. Phys. **82**, 2421 (2010).

[12] M. Horio, T. Adachi, Y. Mori, A. Takahashi, T. Yoshida, H. Suzuki, L. C. C. Ambolode II, K. Okazaki, K. Ono, H. Kumigashira, H. Anzai, M. Arita, H. Namatame, M. Taniguchi, D. Ootsuki, K. Sawada, M. Takahashi, T. Mizokawa, Y. Koike, and A. Fujimori, Nature Commun. **7**, 10567 (2016).

[13] D. A. Wollman, D. J. Van Harlingen, W. C. Lee, D. M. Ginsberg, and A. J. Leggett, Phys. Rev. Lett. **71**, 2134 (1993).

[14] J. M. Tranquada, B. J. Sternlieb, J. D. Axe, Y. Nakamura, and S. Uchida, Nature **375** 561 (1995).

[15] T. Wu, H. Mayaffre, S. Krämer, M. Horvatić, C. Berthier, W. N. Hardy, R. Liang, D. A. Bonn, and M.-H. Julien, Nature **477**, 191 (2011).

[16] E. H. da Silva Neto, P. Aynajian, A. Frano, R. Comin, E. Schierle, E. Weschke, A. Gyenis, J. Wen, J. Schneeloch, Z. Xu, S. Ono, G. Gu, M. Le Tacon, A. Yazdani, Science **343**, 393 (2014).

[17] R. Comin, A. Frano, M. M. Yee, Y. Yoshida, H. Eisaki, E. Schierle, E. Weschke, R. Sutarto, F. He, A. Soumyanarayanan, Y. He, M. Le Tacon, I. S. Elfimov, J. E. Hoffman, G. A. Sawatzky, B. Keimer, and A. Damascelli, Science **343**, 390 (2014).

[18] W. Tabis, Y. Li, M. Le Tacon, L. Braicovich, A. Kreyssig, M. Minola, G. Dellea, E. Weschke, M. J. Veit, M. Ramazanoglu, A. I. Goldman, T. Schmitt, G. Ghiringhelli, N. Barišić, M. K. Chan, C. J. Dorow, G. Yu, X. Zhao, B. Keimer, and M. Greven, Nature Commun. **5**, 5875 (2014).

[19] B. Keimer, S. A. Kivelson, M. R. Norman, S. Uchida, and J. Zaanen, Nature **518**, 179 (2015).

[20] V. Hinkov, D. Haug, B. Fauqué, P. Bourges, Y. Sidis, A. Ivanov, C. Bernhard, C. T. Lin, B. Keimer, Science **319**, 597 (2008).

[21] M. J. Lawler, K. Fujita, J. Lee, A. R. Schmidt, Y. Kohsaka, C. K. Kim, H. Eisaki, S. Uchida, J. C. Davis, J. P. Sethna, E.-A. Kim, Nature **466**, 347 (2010).

[22] Y. Ando, K. Segawa, S. Komiya, and A. N. Lavrov, Phys. Rev. Lett. **88**, 137005 (2002).

[23] Y. Yanase, T. Jujo, T. Nomura, H. Ikeda, T. Hotta, and K. Yamada, Physics Reports **387**, 1 (2003).

[24] J. Hubbard, Proc. R. Soc. London A **276**, 238 (1963).

[25] F. C. Zhang and T. M. Rice, Phys. Rev. B **37**, 3759 (1988).

[26] D. J. Scalapino, E. Loh, Jr., and J. E. Hirsch, Phys. Rev. B **35**, 6694 (1987).

[27] N. E. Bickers, D. J. Scalapino, and S. R. White, Phys. Rev. Lett. **62**, 961 (1989).

[28] S. R. White, D. J. Scalapino, R. L. Sugar, N. E. Bickers, and R. T. Scalettar, Phys. Rev. B **39**, 839 (1989)(R).

[29] S. Zhang, J. Carlson, and J. E. Gubernatis, Phys. Rev. Lett. **78**, 4486 (1997).

[30] K. Kuroki and H. Aoki, Phys. Rev. B **56**, R14287 (1997).

[31] K. Kuroki, H. Aoki, T. Hotta, and Y. Takada, Phys. Rev. B **55**, 2764 (1997).

[32] W. Metzner and D. Vollhardt, Phys. Rev. Lett. **62**, 324 (1989).

[33] A. Georges and G. Kotliar, Phys. Rev. B **45**, 6479 (1992).

[34] A. Georges, G. Kotliar, W. Krauth, and M. J. Rozenberg, Rev. Mod. Phys. **68**, 13 (1996).

[35] M. H. Hettler, A. N. Tahvildar-Zadeh, M. Jarrell, T. Pruschke, and H. R. Krishnamurthy, Phys. Rev. B **58**, 7475 (1998).

[36] A. I. Lichtenstein and M. I. Katsnelson, Phys. Rev. B **62**, 9283 (2000).

[37] G. Kotliar, S. Y. Savrasov, G. Palsson, and G. Biroli, Phys. Rev. Lett. **87**, 186401 (2001).

[38] Th. Maier, M. Jarrell, Th. Pruschke, and J. Keller, Phys. Rev. Lett. **85**, 1524 (2000).

[39] S. Sakai, Y. Motome, and M. Imada, Phys. Rev. B **82**, 134505 (2010).

[40] E. Gull, O. Parcollet, and A. J. Millis, Phys. Rev. Lett. **110**, 216405 (2013).

[41] A. Toschi, A. A. Katanin, and K. Held, Phys. Rev. B **75**, 045118 (2007).

[42] A. N. Rubtsov, M. I. Katsnelson, and A. I. Lichtenstein, Phys. Rev. B **77**, 033101 (2008).

[43] S. Brener, H. Hafermann, A. N. Rubtsov, M. I. Katsnelson, and A. I. Lichtenstein, Phys. Rev. B **77**, 195105 (2008).

[44] J. Otsuki, H. Hafermann, and A. I. Lichtenstein, Phys. Rev. B **90**, 235132 (2014).

[45] C. Taranto, S. Andergassen, J. Bauer, K. Held, A. Katanin, W. Metzner, G. Rohringer, and A. Toschi, Phys. Rev. Lett. **112**, 196402 (2014).

[46] G. Rohringer, A. Toschi, A. A. Katanin, and K. Held, Phys. Rev. Lett. **107**, 256402 (2011).

[47] T. Schäfer, F. Geles, D. Rost, G. Rohringer, E. Arrigoni, K. Held, N. Blümer, M. Aichhorn, and A. Toschi, Phys. Rev. B **91**, 125109 (2015).

[48] M. Kitatani, N. Tsuji, and H. Aoki, Phys. Rev. B **92**, 085104 (2015).

[49] M. Kitatani, N. Tsuji, and H. Aoki, Phys. Rev. B **95**, 075109 (2017).

[50] A. A. Katanin, A. Toschi, and K. Held, Phys. Rev. B **80**, 075104 (2009).

[51] H. Shimahara and S. Takada, J. Phys. Soc. Jpn. **57**, 1044 (1988).

[52] Y. M. Vilk and A.-M. S. Tremblay, J. Phys. I France **7**, 1309 (1997).

[53] G. Baym and L. P. Kadanoff, Phys. Rev. **124**, 287 (1961).

[54] G. Baym, Phys. Rev. **127**, 1391 (1962).

[55] J. M. Luttinger and J. C. Ward, Phys. Rev. **118**, 1417 (1960).

[56] M. Jarrell, Phys. Rev. Lett. **69**, 168 (1992).

[57] X. Y. Zhang, M. J. Rozenberg, and G. Kotliar Phys. Rev. Lett. **70**, 1666 (1993).

[58] H. Kajueter and G. Kotliar, Phys. Rev. Lett. **77**, 1 (1996).

[59] M. Potthoff, T. Wegner, and W. Nolting, Phys. Rev. B **55**, 24 (1997).

[60] M. Caffarel and W. Krauth, Phys. Rev. Lett. **72**, 1545 (1994).

[61] Q. Si, M. Rozenberg, G. Kotoliar, and A. Ruckenstein, Phys. Rev. Lett. **72**, 2761 (1994).

[62] S. Moukouri and M. Jarrell, Phys. Rev. Lett. **87**, 167010 (2001).

[63] J. P. Hague, M. Jarrell, and T. C. Schulthess, Phys. Rev. B **69**, 165113 (2004).

[64] J. Gukelberger, L. Huang, and P. Werner, Phys. Rev. B **91**, 235114 (2015).

[65] Y. Yanase and M. Ogata, J. Phys. Soc. Jpn. **74**, 1534 (2005).

[66] K. Nishiguchi, K. Kuroki, R. Arita, T. Oka, and H. Aoki, Phys. Rev. B **88**, 014509 (2013); K. Nishiguchi, Ph. D. Thesis, Univ. of Tokyo (2013).

[67] Similar values are also obtained in H. Sakakibara, H. Usui, K. Kuroki, R. Arita, and H. Aoki, Phys. Rev. Lett. **105**, 057003 (2010).

[68] N. D. Mermin and H. Wagner, Phys. Rev. Lett. **17**, 1133 (1966).

[69] T. Koma and H. Tasaki, Phys. Rev. Lett. **68**, 3248 (1992).

[70] G. Su and M. Suzuki, Phys. Rev. B **58**, 117 (1998).

[71] R. Arita, K. Kuroki, and H. Aoki, J. Phys. Soc. Jpn. **69**, 1181 (2000).

[72] C. Yasuda, S. Todo, K. Hukushima, F. Alet, M. Keller, M. Troyer, and H. Takayama, Phys. Rev. Lett. **94**, 217201 (2005).

[73] B.-X. Zheng and G. K.-L. Chan, Phys. Rev. B **93**, 035126 (2016).

[74] T. Misawa and M. Imada, Phys. Rev. B **90**, 115137 (2014).

[75] Y. Yanase and K. Yamada, J. Phys. Soc. Jpn. **70**, 1659 (2001).

[76] A. N. Rubtsov, M. I. Katsnelson, A. I. Lichtenstein, and A. Georges, Phys. Rev. B **79**, 045133 (2009).

[77] H. Hafermann, G. Li, A. N. Rubtsov, M. I. Katsnelson, A. I. Lichtenstein, and H. Monien, Phys. Rev. Lett. **102**, 206401 (2009).

[78] G. Rohringer, A. Toschi, H. Hafermann, K. Held, V. I. Anisimov, and A. A. Katanin, Phys. Rev. B **88**, 115112 (2013).

[79] E.-A. Kim, M. J. Lawler, P. Oreto, S. Sachdev, E. Fradkin, and S. A. Kivelson, Phys. Rev. B **77**, 184514 (2008).

[80] Y. Huh and S. Sachdev, Phys. Rev. B **78**, 064512 (2008).

[81] S.A. Kivelson, E. Fradkin, and V. J. Emery, Nature **393**, 550 (1998).

[82] H. Yamase and W. Metzner, Phys. Rev. B **73**, 214517 (2006).

[83] C. J. Halboth and W. Metzner, Phys. Rev. Lett. **85**, 5162 (2000).

[84] H. Yamase and H. Khono, J. Phys. Soc. Jpn. **69**, 332 (2000).

[85] H. Yamase, V. Oganesyan, and W. Metzner, Phys. Rev. B **72**, 35114 (2005).

[86] P. Jakubczyk, W. Metzner, and H. Yamase, Phys. Rev. Lett. **103**, 239904 (2009).

[87] C. Honerkamp, M. Salmhofer, and T. M. Rice, Eur. Phys. J. B **27**, 127 (2002).

[88] V. Hankevych, I. Grote, and F. Wegner, Phys. Rev. B **66**, 094516 (2002).

[89] J. Kaczmarczyk, T. Schickling, and J. Bunemann, Phys. Rev. B **94**, 085152 (2016).

[90] S. Su and T. A. Maier, Phys. Rev. B **84**, 220506(R) (2011).

[91] S. Okamoto, D. Senechal, M. Civelli, and A. M. S. Tremblay, Phys. Rev. B **82**, 180511(R) (2010).

[92] H. Yamase and W. Metzner, Phys. Rev. B **75**, 155117 (2007).

[93] A. N. Rubtsov, V. V. Savkin, and A. I. Lichtenstein, Phys. Rev. B **72**, 035122 (2005).

[94] E. Gull, A. J. Millis, A. I. Lichtenstein, A. N. Rubtsov, M. Troyer, and P. Werner, Rev. Mod. Phys. **83**, 349 (2011).

[95] B. Bauer, L. D. Carr, H. G. Evertz, A. Feiguin, J. Freire, S. Fuchs, L. Gamper, J. Gukelberger, E. Gull, S. Guertler, A. Hehn, R. Igarashi, S. V. Isakov, D. Koop, P. N. Ma, P. Mates, H. Matsuo, O. Parcollet, G. Pawłowski, J. D. Picon, L. Pollet, E. Santos, V. W. Scarola, U. Schollwöck, C. Silva, B. Surer, S. Todo, S. Trebst, M Troyer, M. L. Wall, P. Werner, and S. Wessel, J. Stat. Mech. P05001 (2011).

[96] A. F. Albuquerque, F. Alet, P. Corboz, P. Dayal, A. Feiguin, S. Fuchs, L. Gamper, E. Gull, S. Guertler, A. Honecker, R. Igarashi, M. Koerner, A. Kozhevnikov, A. Laeuchli, S. R. Manmana, M. Matsumoto, I. P. McCulloch, F. Michel, R. M. Noack, G. Pawlowski, L. Pollet, T. Pruschke, U. Schollwock, S. Todo, S. Trebst, M. Troyer, P. Werner, and S. Wessel, J. Magn. Magn. Mater. **310**, 1187 (2007).

[97] A. T. Rømer, A. Kreisel, I. Eremin, M. A. Malakhov, T. A. Maier, P. J. Hirschfeld, and B. M. Andersen, Phys. Rev. B **92**, 104505 (2015).

[98] U. Opik and M. H. L. Pryce, Proc. Roy. Soc. London Ser. A **238**, 425 (1957).

[99] M. B. Walker and P. Contreras, Phys. Rev. B **66**, 214508 (2002).

[100] V. Mishra, U. Chatterjee, J. C. Campuzano, and M. R. Norman, Nat. Phys., **10**, 357 (2014).

[101] T. A. Maier, P. Staar, D. J. Scalapino, arXiv:1507.06206.

[102] S. Sakai, M. Civelli, and M. Imada, Phys. Rev. Lett. **116**, 057003 (2016).

[103] A. Valli, T. Schäfer, P. Thunström, G. Rohringer, S. Andergassen, G. Sangiovanni, K. Held, and A. Toschi, Phys. Rev. B **91**, 115115 (2015).

[104] T. Schäfer, A. A. Katanin, K. Held, and A. Toschi, arXiv:1605.06355.

[105] H. Park, K. Haule, and G. Kotliar, Phys. Rev. Lett. **101**, 186403 (2008).

[106] M. Potthoff, M. Aichhorn, and C. Dahnken, Phys. Rev. Lett. **91**, 206402 (2003).

[107] R. Blankenbecler, D. J. Scalapino, and R. L. Sugar, Phys. Rev. D **24**, 2278 (1981).

[108] P. Werner, M. Casula, T. Miyake, F. Aryasetiawan, A. J. Millis, and S. Biermann, Nat. Phys., **8**, 331 (2012).

[109] See, for example, J. V. José, *40 years of Berezinskii-Kosterlitz-Thouless theory* (World Scientific, Singapore, 2013).

[110] See, for example, A. T. Bollinger, G. Dubuis, J. Yoon, D. Pavuna, J. Misewich, and I. Božović, Nature **472**, 458 (2011); Y. Saito, Y. Kasahara, J. Ye, Y. Iwasa, and T. Nojima, Science **350**, 409 (2015).

[111] T. A. Maier, M. Jarrell, T. C. Schulthess, P. R. C. Kent, and J. B. White, Phys. Rev. Lett. **95**, 237001 (2005).

[112] See, for example, H. J. Vidberg and J. W. Serene, J. Low. Temp. Phys. **29**, 179 (1977).

Acknowledgements

First of all, the author would like to express my gratitude to Professor Hideo Aoki, who provided helpful comments and suggestions throughout my Ph.D. course. His advise and encouragement are necessary to complete the present thesis. The author would also like to thank Dr. Naoto Tsuji, who gave me the starting point of the present thesis, and whose opinions have helped very much throughout this study. The author would also like to appreciate Prof. Karsten Held and Dr. Thomas Schäfer in Vienna University of Technology for fruitful discussions. The author would like to thank Prof. Shinji Tsuneyuki and Dr. Ryosuke Akashi for helpful discussions. The author would like to acknowledge Prof. Naoki Kawashima, Prof. Atsushi Fujimori, Prof. Yusuke Kato, Prof. Osamu Sugino, and Prof. Naomichi Hatano for careful reading and constructive comments of the thesis.

The author also thank all the members of the Aoki, Tsuneyuki and Karsten groups for their various helps.

The author would also like to express his gratitude to his family for their encouragements.